

ERC41015.4FR

LEVEL

121

ERC41015.4FR

Copy No. 55

MULTI-PROCESSOR BUS . ARCHITECTURE

FINAL TECHNICAL REPORT FOR THE PERIOD
September 15, 1978 through September 14, 1979

This research was sponsored by the Defense Advanced Research Projects Agency under ARPA Order No. 3671, Contract No. MDA903-78-C-0463, Monitored by the Defense Supply Service.

Effective date of contract: 15 September 1978
Contract expiration date: 14 September 1979

Prepared for
Defense Advanced Research Projects Agency
1400 Wilson Boulevard
Arlington, VA 22209

by
Henry F. Taylor
Principal Investigator
(805) 498-4545, Ext. 280

DTIC
ELECTE
JUL 1 1980

The views and conclusions contained in this document are those of the author and should not be interpreted as necessarily representing the official policies, either expressed or implied, of the Defense Advanced Research Projects Agency or the United States Government.

JUNE 1980

Approved for public release; distribution unlimited



Rockwell International

80 6 30 183

ADA 0861 46

DDC FILE COPY.

UNCLASSIFIED

SECURITY CLASSIFICATION OF THIS PAGE (When Data Entered)

REPORT DOCUMENTATION PAGE		READ INSTRUCTIONS BEFORE COMPLETING FORM
1. REPORT NUMBER	2. GOVT ACCESSION NO.	3. RECIPIENT'S CATALOG NUMBER
	AD-A086 146	
4. TITLE (and Subtitle)	5. TYPE OF REPORT & PERIOD COVERED	
Multi-Processor Bus Architecture.	Final Technical Report 09/15/78 through 09/14/79	
	6. PERFORMING ORG. REPORT NUMBER	
	ERC41015.4FR	
7. AUTHOR(s)	8. CONTRACT OR GRANT NUMBER(s)	
H. Taylor	MDA903-78-C-0463	
10 Henry F. Taylor	ARPA Order No 3671	
9. PERFORMING ORGANIZATION NAME AND ADDRESS		10. PROGRAM ELEMENT, PROJECT, TASK AREA & WORK UNIT NUMBERS
Rockwell International Electronics Research Center 1049 Camino Dos Rios Thousand Oaks, CA 91360		
11. CONTROLLING OFFICE NAME AND ADDRESS		12. REPORT DATE
Defense Advanced Research Projects Agency 1400 Wilson Boulevard Arlington, VA 22209		June 1980
14. MONITORING AGENCY NAME & ADDRESS (if different from Controlling Office)		13. NUMBER OF PAGES
Defense Supply Service		149
9 Final technical rept. 15 Sep 78 - 14 Sep 79		15. SECURITY CLASS. (of this report)
		Unclassified
16. DISTRIBUTION STATEMENT (of this Report)		15a. DECLASSIFICATION/DOWNGRADING SCHEDULE
Approved for public release; distribution unlimited.		12 152
17. DISTRIBUTION STATEMENT (of the abstract entered in Block 20, if different from Report)		
18. SUPPLEMENTARY NOTES		
19. KEY WORDS (Continue on reverse side if necessary and identify by block number)		
Multi-Processor Bus Architecture, Fibers, Splicers, Fiber Optic Transmission Lines, Modulated Semiconductor Lasers, Electrooptic Modulators, Electronic Drivers, Photodiode, Signal-to-Noise Ratio, Frequency-Selective Couplers, Perturbation and Mode Coupling, Coupling Parameters, Parallel Channel Waveguides, High-Data-Rate, GaAs Substrate, Gbit/s, Microprocessor Bus, Mbit/s		
20. ABSTRACT (Continue on reverse side if necessary and identify by block number)		
<p>This report summarizes the results of a one-year study of very high data rate fiber optic buses for computer networks. The primary objectives were to:</p> <p>(1) assess the data rate limitations of components and systems for optical fiber communications, (2) develop a preliminary design for a very high-data-rate optical bus with microprocessor interfaces, and (3) recommend a program of technology development directed towards implementation of such a bus.</p> <p>Mathematical models developed during the course of this program were used extensively for investigating the data rate limitations. The performance of (over)</p>		

DD FORM 1 JAN 73 1473 EDITION OF 1 NOV 65 IS OBSOLETE

UNCLASSIFIED

SECURITY CLASSIFICATION OF THIS PAGE (When Data Entered)

411391

LB

UNCLASSIFIED

SECURITY CLASSIFICATION OF THIS PAGE (When Data Entered)

each component was optimized by varying the key parameters, within limits consistent with the properties of known materials and fabrication techniques. For transmitters and receivers integrated on a GaAs substrate, it is concluded that the maximum data rate for a single channel is limited to about 5 Gbit/s. The key to achieving very high data rates, in excess of 100 Gbit/s, is the use of carrier frequency (wavelength) multiplexing. It is estimated that 20 or more channels could be accommodated in a system of this sort, for an overall data rate per fiber in excess of 100 Gb/s. Higher data rates could be realized by the use of more than one fiber to interconnect bus terminals.

Design of the microprocessor bus considered the problem of interfacing processors with relatively low input-output data rates (~ 10 Mbit/s) with the high-data-rate bus. It is concluded that this problem can be solved by the use of recirculating-loop optical fiber buffers in conjunction with high-speed optical switches. A configuration for a bus terminal based on this concept is proposed.

The analysis indicates that best performance, as well as lowest cost and highest reliability, can be achieved by integrating all of the components for a bus terminal (except for the optical fiber) on a single semi-insulating gallium arsenide substrate. A technology development plan directed towards the realization of the optoelectronic integrated circuits needed for a very high-data-rate optical bus incorporating the features indicated above is outlined.

Accession For	
NTIS GRA&I	<input checked="checked" type="checkbox"/>
DDC TAB	<input type="checkbox"/>
Unannounced	<input type="checkbox"/>
Justification	
By	
Distribution/	
Availability Codes	
Dist.	Avail and/or special
A	

UNCLASSIFIED

SECURITY CLASSIFICATION OF THIS PAGE (When Data Entered)



TABLE OF CONTENTS

	Page
SUMMARY.....	111
1.0 INTRODUCTION.....	1
2.0 SURVEY OF PRESENT COMPONENTS AND SYSTEMS.....	5
2.1 Transmitters.....	5
2.2 Receivers.....	6
2.3 Fibers, Connectors, and Splicers.....	7
2.4 Systems Experiments.....	9
2.5 Summary.....	10
3.0 COMPONENTS LIMITATIONS.....	11
3.1 Fiber Optic Transmission Lines.....	11
3.2 Transmitters.....	16
3.2.1 Directly Modulated Semiconductor Lasers.....	17
3.2.2 External Electrooptic Modulators.....	31
3.2.2.1 Phase Matching of Microwave and Optical Signals.....	35
3.2.2.2 Attenuation and Distortion of Microwave Signal.....	39
3.2.2.3 Materials Considerations.....	42
3.2.3 Electronic Drivers.....	59
3.3 Receivers.....	64
3.3.1 Photodiode design.....	64
3.3.2 Signal-to-Noise Ratio.....	70
3.3.3 Amplifier Design Considerations.....	75
3.4 Electrooptic Switch.....	77
3.5 Frequency-Selective Couplers.....	82
3.5.1 Periodic Perturbation and Mode Coupling.....	86
3.5.2 Coupling Parameters for Parallel Channel Waveguides.....	97
3.5.3 Device Design Example.....	112
3.5.4 Design and Fabrication Criteria.....	113
3.6 Summary.....	117
4.0 TECHNOLOGY TRADEOFFS.....	120
5.0 BUS DESIGN	126
6.0 CONCLUSIONS	137
REFERENCES	140



SUMMARY

ERC41015.4FR

This report summarizes the results of a one-year study of very high data rate fiber optic buses for computer networks. The primary objectives were to: (1) assess the data rate limitations of components and systems for optical fiber communications, (2) develop a preliminary design for a very high-data-rate optical bus with microprocessor interfaces, and (3) recommend a program of technology development directed towards implementation of such a bus.

Mathematical models developed during the course of this program were used extensively for investigating the data rate limitations. The performance of each component was optimized by varying key parameters, within limits consistent with the properties of known materials and fabrication techniques. For transmitters and receivers integrated on a GaAs substrate, it is concluded that the maximum data rate for a single channel is limited to about 5 Gbit/s. The key to achieving very high data rates, in excess of 100 Gbit/s, is the use of carrier frequency (wavelength) multiplexing. It is estimated that 20 or more channels could be accommodated in a system of this sort, for an overall data rate per fiber in excess of 100 Gb/s. Higher data rates could be realized by the use of more than one fiber to interconnect bus terminals.

Design of the microprocessor bus considered the problem of interfacing processors with relatively low input-output data rates (~ 10 Mbit/s) with the high-data-rate bus. It is concluded that this problem can be solved by the use of recirculating-loop optical fiber buffers in conjunction with high-speed optical switches. A configuration for a bus terminal based on this concept has been proposed.

The analysis indicates that best performance, as well as lowest cost and highest reliability, can be achieved by integrating all of the components for a bus terminal (except for the optical fiber) on a single semi-insulating gallium arsenide substrate. A technology development plan directed towards the realization of the optoelectronic integrated circuits needed for a very high-data-rate optical bus incorporating the features indicated above has been outlined.



1.0 INTRODUCTION

As the technology of electronic data processing continues to advance at a phenomenal rate, the limitations of present data communications systems becomes more and more apparent. The evolution of LSI and VLSI chips with higher switching speeds, lower power consumption, and greater circuit densities will lead to new generations of computers which, though physically smaller than their predecessors, have faster central processing units and larger memories. As a result, input-output data rates for state-of-the-art computers are steadily increasing. This trend could even accelerate over the next few years with the advent of the new gallium arsenide integrated circuit technology, which can provide much higher speed and lower power dissipation than the traditional silicon circuits. Furthermore, with continuing advances in analog-to-digital conversion technology, the quantity of digital data which is available from the analog output of sensors continues to increase rapidly. All of these factors lead to requirements for higher and higher communication data rates in information processing systems.

Coaxial cables and twisted wire pairs are still the primary media for data communications, just as they were decades ago. Data rates for these electrical transmission lines are limited to a few megabits per second for lengths of one kilometer. These relatively low data rates are not adequate to meet the requirements of many of our modern military information processing systems.

The new technology which is capable of overcoming these limitations is fiber optics communications. Since the first low-loss (20 dB/km) fibers were produced ten years ago,¹ an optical communication industry based on the use of semiconductor light sources and photodetectors and silica fibers has evolved. Fibers with losses as low as 0.2 dB/km have been produced in the laboratory,² with losses of 2 dB/km routinely achieved in production. Experimental links have been operated at data rates as high as 1.6 Gbits/s over transmission line lengths in excess of 10 km.³ Although fiber optics has not yet made a large impact in data processing due to the relatively high cost of components, it is

anticipated that lower costs and requirements for larger transmission capacity will combine to make the technology cost-effective for an increasing number of civilian and military computer systems in the years ahead.

Data rates of state-of-the-art optical transmitters and receivers are limited to less than 2 Gb/s, yet much higher rates could be effectively utilized in future military systems. One example of such a system is the distributed computer network illustrated in Fig. 1.1, in which the terminals communicate with one another in a burst transmission mode. Best performance in such a system is obtained if data is transmitted on the interconnecting bus at very high rates, much higher than the input-output data rates for the individual processors. Performance improvements are realized because the use of a very high data rate bus makes it possible to minimize the interterminal delays for the data packets. Potential applications for such a bus include multisensor correlation, image processing, artificial intelligence, weather prediction, and display terminal networks.

This report summarizes the results of a detailed study of the capabilities and limitations of optical technology as it applies to the high data rate multiterminal bus. The study has been performed by Rockwell during FY 1979 under the program "Multi-Processor Bus Architecture," sponsored by the Information Processing Techniques Office of the Defense Advanced Research Project Agency.

The study has been guided by the following set of assumptions, or "ground rules:"

- (1) Only solid state components are used at the bus terminals.
- (2) Single-mode fibers are the transmission media.
- (3) The optical sources emit at near-infrared wavelengths.
- (4) No material breakthroughs are anticipated; i.e., the calculations make use of the parameters and characteristics of presently known optical and electronic materials.
- (5) The system is designed for local distribution, with a maximum interterminal separation of 100 m and a maximum total bus length of 1 km.

FIBER OPTIC DATA BUS CONCEPT

SC78-2052

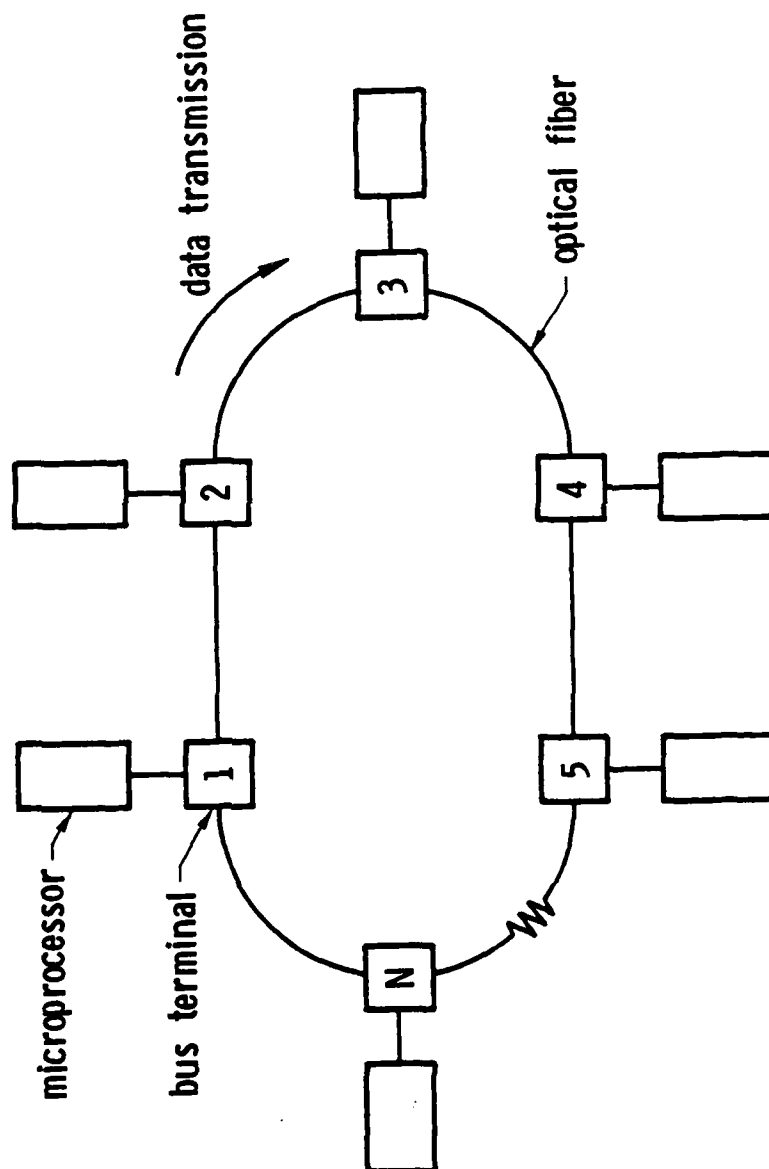


Fig. 1.1 Schematic of fiber optic data bus for interconnecting microprocessor terminals.



Rockwell International

ERC41015.4FR

This report is organized such that one section is allocated to each of the contractual tasks, which are:

- (1) A survey of the state-of-the-art of optical and electronic components which could be used in a very-high-speed ring bus.
- (2) An assessment of physical limitations on component performance for the bus application.
- (3) An analysis of the relative merits of possible approaches to achieving the highest level of system performance.
- (4) The design of a baseline system which is judged to have the potential for very-high-speed operation.
- (5) The delineation of technology development tasks required to achieve the desired level of performance.

The author expresses appreciation to P.D. Dapkus, A.I. Higgins, C.S. Hong, W.W. Ng, and L.R. Tomasetta of the Electronics Research Center and P. Yeh of the Science Center for numerous technical discussions and for preparing some of the material used in this report. He would also like to thank Dr. Vinton Cerf, Information Processing Techniques Office, Defense Advanced Research Projects Agency, for his encouragement and support during the course of this effort.



ERC41015.4FR

2.0 SURVEY OF PRESENT COMPONENTS AND SYSTEMS

A great deal of effort has been expended during the past decade in research and development on components and systems for optical fiber communications. Since the great majority of commercial and military applications require bandwidths less than 100 MHz, only a small percentage of the overall effort has been concerned with reaching higher bandwidths. However, during the past two or three years there has been an increasing interest in wideband fiber optic technology, particularly for digital transmission. This section summarizes the state-of-the-art in components and systems for high-data-rate fiber optical communications. Included in the survey are transmitters, receivers, and fibers, as well as systems demonstrated to date.

2.1 Transmitters

A number of digital optical transmitters have been developed for operation at data rates in the 1.0 - 2.3 Gbits/s range. Most of these experiments have utilized injection laser diodes as the optical source, directly modulated by varying the current to the device. The first demonstration of 1 Gbit/s modulation was reported in 1973.⁴ The laser was a stripe-geometry $\text{Ga}_x\text{Al}_{1-x}\text{As}$ double-heterostructure diode, and the driver was a silicon emitter-coupled logic circuit. A similar experiment was performed shortly thereafter using a Trapatt diode as the laser driver.⁵ Digital modulation of injection lasers at rates as high as 2.3 Gbit/s using a Gunn diode as the driver was also reported in 1973.⁶

These early experiments demonstrated the feasibility of direct modulation of semiconductor lasers at high speeds. However, practical transmitters and repeaters for optical communications require more sophisticated electronics for shaping input electrical pulses and providing sufficient amplitude from a low-level input signal to drive the laser. More recent work has concentrated on development of the circuitry needed to demonstrate these capabilities by the transmission of pseudorandom bit sequences. One such experiment utilized a GaAs FET as the driver for a GaAlAs laser.⁷ In another experiment, a transferred electron logic device (TELD), a planar Gunn-effect device used as a current switch, was the pulse shaping and driving element in a 1.5 Gbit/s transmitter.⁸

Finally, a transmitter incorporating an InGaAsP double heterostructure laser was operated at a 1.6 Gbit/s data rate.⁹ The quaternary InGaAsP laser is of particular interest for long-distance, high data rate systems because it can be designed for an emission wavelength in the 1.2 - 1.5 μm range, where the dispersion and losses of doped silica fibers are lowest. Both loss and dispersion are substantially higher in the 0.8 - 0.9 μm region, where the GaAlAs lasers operate most efficiently.

An alternative to direct modulation of semiconductor lasers is the use of a cw laser with an external modulator. A bandwidth of 1 GHz was demonstrated several years ago in a LiTaO₃ optical waveguide modulator.¹⁰ More recently, a bandwidth of 10.5 GHz was reported in a LiNbO₃ waveguide modulator, using a traveling wave configuration in which the modulating signal is carried on a coplanar transmission line, impedance matched to the driving circuit.¹¹ However, the modulators used for these feasibility demonstrations did not incorporate driving circuitry suitable for interfacing with a communication system. In particular, the 10.5 GHz modulator was driven from an oscillator and the pulse response was not investigated. Also, the depth of modulation was not reported for that device.

It should also be mentioned that a 1 Gbit/s transmitter using a mode-locked Nd:YAG laser and a LiTaO₃ bulk modulator has been developed for space communications.¹² However, that transmitter is not viewed as practical for fiber optic applications, inasmuch as the electrical power required for the modulator alone was about 50 W.

2.2 Receivers

A number of solid-state optical receivers have been demonstrated to operate at rates in excess of 1 Gbit/s. Most of these were developed to be compatible with optical transmitters for use in link transmission experiments. The receivers have all incorporated semiconductor avalanche photodiodes (APDs) as the optical sensor. The APD is desirable because its inherent internal gain improves the signal-to-noise ratio for a given optical power input and also reduces the gain required from the electronic amplifier.



ERC41015.4FR

APDs fabricated in the elemental semiconductor materials Si¹³ and Ge¹⁴ have shown response equivalent to digital data rates greater than 2 Gbit/s. The decreasing optical absorption of Si at longer wavelengths limits its spectral region for efficient operation to wavelengths less than about 1.1 μm . On the other hand, although the quantum efficiency of Ge is high at longer wavelengths, noise due to the high dark current limits its sensitivity. APDs fabricated from compound semiconductors such as GaAlAs for wavelengths less than 0.9 μm and GaAlAsSb and InGaAsP at wavelengths in the 1.0 - 1.6 μm range have much lower dark current than Ge and extremely fast response, equivalent to at least 5 Gbit/s.¹⁵

A high-speed digital receiver contains not only the photodetector but also an amplifier and a threshold circuit to restore a clean digital waveform. The fastest digital receiver reported to date used a Si APD and bipolar Si amplifiers and threshold circuitry and operated at 1.6 Gbit/s.³ Another Si APD receiver used a GaAs FET preamplifier to obtain operation at 1.12 Gbit/s.¹⁶ A receiver using a GaAs photodiode and GaAs FET circuit has also been demonstrated at 1 Gbit/s.¹⁷

2.3 Fibers, Connectors, and Splicers

The attenuation in optical fibers has dropped dramatically over the past decade. Prior to 1970, the lowest fiber losses were in the neighborhood of 1000 dB/km. In 1970 the first "low-loss" fiber, with an attenuation of 20 dB/km, was reported.¹ Recently, a loss figure of only 0.2 dB/km was achieved in a doped silica single-mode fiber at a wavelength of 1.5 μm ,² as illustrated in the spectral loss plot of Fig. 2.1. This is close to the "Rayleigh limit" of loss resulting from the scattering of light from frozen-in refractive index inhomogeneities. At the wavelength of 0.85 μm where GaAlAs lasers have best performance and 1.3 μm , at which InGaAsP lasers emit efficiently, the losses are 2 and 0.6 dB/km, respectively.

The data-rate capacity of single-mode fiber has been determined in experiments on pulse broadening in the fibers. At a wavelength of 0.85 μm , the dispersion is about 8 ps per km of fiber length per \AA of source spectral

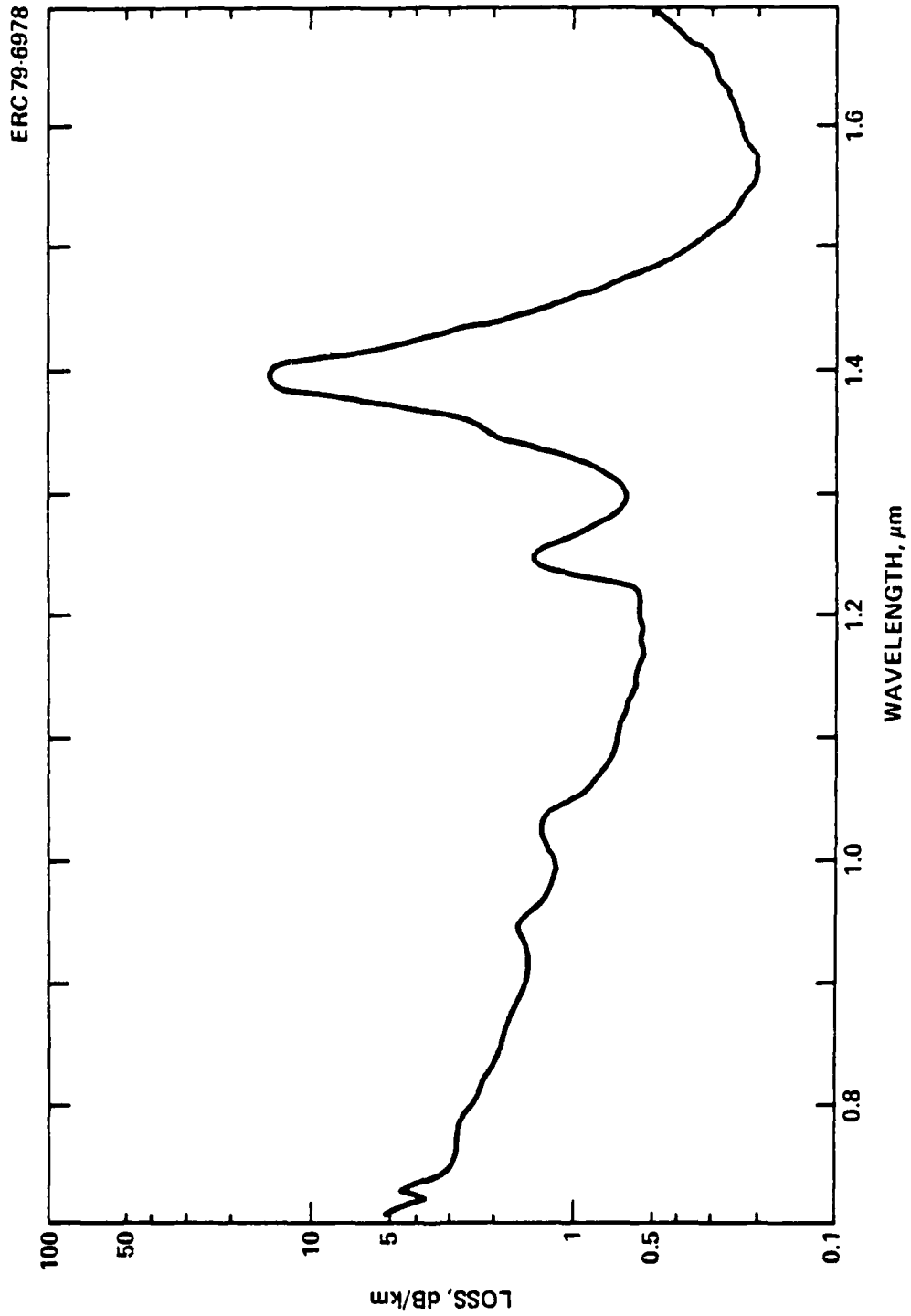


Fig. 2.1 Spectral attenuation curve for single mode silica fiber.



ERC41015.4FR

width,¹⁸ corresponding to a maximum data rate of about 10 Gbit-km/s for a source with 1Å spectral width. Near the dispersion minimum at 1.3 μm , the dispersion^{18,19} is less than 0.5 ps/km-Å, corresponding to a maximum data rate in excess of 50 Gbit-km/s for a 1Å source spectral width. The limitation in the latter case stems not from the inherent spectral width of the source but from the spectral broadening introduced by the modulating pulses.

Splicing of single mode fibers is important for producing long continuous lengths of fiber, since the initial draw is usually only one or two kilometers long. Splicing is also needed for field installation and repair of the fiber cables. Fusion splicing with an electric arc has been demonstrated to produce losses consistently less than 0.5 dB in the laboratory,²⁰ although careful alignment of the fibers is needed due to the small ($\sim 5 \mu\text{m}$) diameters of the fiber cores. It is also important that good uniformity of fiber diameter as well as core concentricity be maintained for consistently good results with this type of splice.

Demountable connectors for single-mode fibers has long been a critical problem, due to the mechanical tolerances ($\sim 1 \mu\text{m}$) required to achieve low optical loss. Recently, a connector using mating plugs and a sleeve with ballbearing arrays to force alignment, has demonstrated insertion losses consistently less than 0.7 dB.²¹ As with the low-loss splice, it is important to maintain diameter uniformity and core concentricity for the mating fiber ends.

2.4 Systems Experiments

Extensive development of single mode components at Nippon Telegraph and Telephone has recently culminated in some impressive demonstrations of point-to-point data transmission over single-mode fibers. One of these made use of a CW $\text{LiNdP}_4\text{O}_{12}$ laser emitting at a wavelength of 1.05 μm and a LiNbO_3 waveguide modulation to transmit data over a 4 km length of fiber at an 800 Mbit/s rate.²² The results of two other experiments which utilized directly modulated semiconductor lasers at data rates of 800 Mbit/s²³ and 1.6 Gbit/s³ are summarized in Table 2.1.

Table 2.1
Results of Single Mode Transmission Experiments

	Ref. 23	Ref. 3
Data Rate	800 Mbit/s	1600 Mbit/s
Length	7.3 km	13.1 km
Laser Material	GaAlAs	InGaAsP
Emission Wavelength, λ_0	.85 μm	1.29 μm
Spectral Width	$\sim 1 \text{ \AA}$	$\sim 1 \text{ \AA}$
Dispersion at λ_0	9 ps/ \AA -km	$\sim .4 \text{ ps}/\text{\AA}$ -km
Total Dispersion	65 ps	5 ps
Power Coupled Into Fiber	-0.5 dBm	-7.6 dBm
Photodetector Type	Si APD	Ge APD
Received Power, 10^{-9} error rate	-26 dBm	-23.0 dBm
Allowable Loss, 10^{-9} error rate	25.5 dB	15.4 dB
Total Fiber Loss	24.3 dB	10.4 dB

2.5 Summary

The results of the 1.6 Gbit/s data transmission experiments described in the preceding section provide a good indication of the state-of-the-art in high-data-rate fiber optic telemetry. The maximum data rates were limited by the transmitter and receiver response rather than by fiber propagation in those experiments. Discrete lasers were used in the transmitters and discrete photodiodes in the receivers, and silicon circuitry was used in both the laser drivers and receiver amplifiers and decision circuits. Maximum data rates using that approach are estimated to lie in the 2 - 2.5 Gbit/s range, limited primarily by the response speed of the silicon circuits. Higher speeds can be anticipated using gallium arsenide electronics, particularly if the optoelectronic components (i.e., lasers and photodetectors) are integrated on the same substrate with the electronic devices.



3.0 COMPONENT LIMITATIONS

Sound estimates of the performance limitations for the critical components are essential to a reliable assessment of the potential data rate of the fiber optic ring bus. Limitations for each of the key elements of the system -- fibers, transmitters, receivers, switches, and frequency-selective couplers -- are analyzed in the following sections. These analyses make use of mathematical models developed during the course of this study as an aid in predicting the performance of the key components.

3.1 Fiber Optic Transmission Lines

Optical fibers are used not only for transmitting data between the terminals of the hypothetical bus system described in Section 5, but also as data buffers in interfacing the main bus with microprocessors. It is assumed that single-mode fibers are used because of their superior bandwidth and because they are compatible with guided wave switches and frequency-selective couplers. The most important parameters of the fibers are the dispersion, which limits the fiber bandwidth, and the attenuation, including connecting and splicing losses. Polarization effects are also of some concern.

As indicated in Section 2, an attenuation of 2.5 dB/km at a wavelength of $.8 \mu\text{m}$ and only .2 dB/km at $1.6 \mu\text{m}$ have been achieved in single-mode fibers. The maximum interterminal separation is assumed to be 100 meters for the ring bus, so the fiber attenuation is less than 0.3 dB and can be neglected. Recent progress has also reduced connector and splicing losses to less than 1 dB.

Preservation of polarization in the fiber is important because response of electrooptic switches and modulators to an applied voltage is generally different for the two polarization states. The output polarization of a conventional circular core fiber is in general a mixture of the two linear polarization states and is sensitive to environmental and mechanical perturbations. However, it has been shown that birefringent single-mode fibers which maintain polarization can be produced by introducing a nonsymmetric stress in the

manufacturing process.²⁴ It is assumed that polarization preserving fibers are used for the distributed processor system, and only one polarization state of the fibers, modulators, and switches is excited. This should not be difficult in practice, since the output of injection lasers is generally linearly polarized, with the polarization vector in the plane of the junction.

The final factor of importance -- and the one of most concern to us -- is dispersion in the fiber. For single mode fibers in which only one polarization mode is excited, the only sources of dispersion are material dispersion and waveguide dispersion. For wavelengths less than 1 μm , material dispersion is dominant and the total dispersion is determined primarily by the properties of the doped silica from which the fiber is fabricated. The dispersion of fused silica is plotted as a function of wavelength in Fig. 3.1.²⁵ Note that at a wavelength of 0.8 μm , the dispersion coefficient per unit length and per unit spectral width, is about 10 ps/km-Å. Thus, for a 100 meter terminal separation, the dispersion is only 1 ps per angstrom of spectral width of the injected optical signal.

In investigating the ultimate bandwidth of single-mode fibers, it is important to note that the spectral width of the optical signal depends on both the spectral width of the unmodulated optical source and on the bandwidth of the modulating signal. If the signal injected into the transmission line is a Gaussian pulse of the form

$$f(t) = Ae^{-\left(\frac{t^2}{\tau}\right)},$$

then the spectrum, defined by

$$F(\omega) = \frac{1}{2\pi} \int_{-\infty}^{\infty} \cos \omega t f(t) dt$$



Rockwell International

ERC41015.4FR

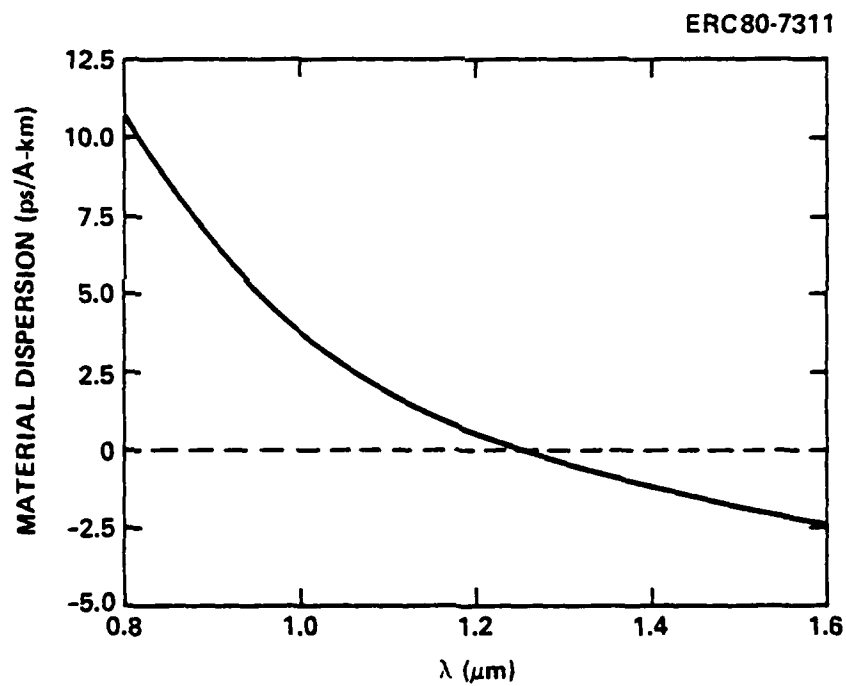


Fig. 3.1 Dependence of material dispersion coefficients on wavelength for fused silica.

is given by

$$F(\omega) = \frac{\tau}{2\sqrt{\pi}} e^{-\frac{\omega^2 \tau^2}{4}}$$

The spectral width to 10% amplitude points $\Delta\omega_0$ is given by

$$\frac{\Delta\omega_0^2}{2} = -\frac{4}{\tau^2} \ln .1 ,$$

or

$$\Delta\omega_0 = \frac{6.06}{\tau} .$$

On the other hand, the temporal width of the incident pulse to 10% amplitude points, Δt_0 , is given by

$$\frac{\Delta t_0^2}{2} = -\tau^2 \ln .1$$

or

$$\Delta t_0 = 3.03 \tau ,$$

so

$$\Delta\omega_0 \Delta t_0 = 18.4 .$$

The pulse width after propagation over a distance L is given by

$$\Delta t = \left(\Delta t_0^2 + d^2 L^2 \Delta\lambda^2 \right)^{1/2} ,$$

where d is the fiber dispersion coefficient,

$$\Delta\lambda^2 = \Delta\lambda_0^2 + \Delta\lambda_s^2 ,$$



ERC41015.4FR

with $\Delta\lambda_0$ the spectral width due to the modulation of the source, and $\Delta\lambda_s$ the spectral width of the unmodulated source. It is necessary to express $\Delta\omega_0$ in terms of $\Delta\lambda_0$ to evaluate the pulse dispersion. Since

$$\lambda v = c,$$

with c the free-space velocity of light and v the optical frequency, then,
with $\omega_0 = 2\pi v_0$,

$$\lambda_0 \omega_0 = 2\pi c. \quad (3.1)$$

But

$$\lambda_0 \Delta\omega_0 + \omega_0 \Delta\lambda_0 = 0,$$

or

$$\frac{\Delta\omega_0}{\omega_0} = - \frac{\Delta\lambda_0}{\lambda_0}.$$

Eliminating ω_0 from this expression yields

$$\Delta\omega_0 = - \frac{2\pi c \Delta\lambda_0}{\lambda_0^2}. \quad (3.2)$$

Finally, from (3.1) and (3.2),

$$\Delta\lambda_0 = - \frac{18.4 \lambda_0^2}{2\pi c \Delta t_0} = - 2.92 \frac{\lambda_0^2}{c \Delta t_0}.$$

For $\lambda_0 = .85 \mu\text{m}$, with $c = 3 \times 10^{10} \text{ cm/sec}$,

$$\Delta\lambda_0 = \frac{K_d}{\Delta t_0} ,$$

with $K_d = 7.05 \times 10^{-11}$ A-s. Thus the expression for pulse dispersion becomes

$$\Delta t = [\Delta t_0^2 + d^2 L^2 (\Delta\lambda_s^2 + K_d^2 / \Delta t_0^2)]^{1/2} . \quad (3.3)$$

Differentiating this expression with respect to Δt_0 yields the result that the minimum pulse width is

$$\Delta t_{\min} = (2K_d d L + \Delta\lambda_s^2 d^2 L^2)^{1/2}$$

which is obtained for $\Delta t_0 = (K_d d L)^{1/2}$. As a numerical example, if $d = 10$ ps/A-km, $L = 100$ m, $\Delta\lambda_s = 1$ Å, then $\Delta t_{\min} = 12$ ps. The inverse of Δt_{\min} yields an equivalent data rate of 83 Gbit/s, which can be taken as a measure of the data capacity of the fiber for a single optical carrier frequency channel. Clearly, this example demonstrates that the fiber is not the component which limits the data rate of the overall system.

3.2 Transmitters

In virtually all present-day fiber optic communication systems, modulation of the optical carrier is accomplished by varying the driving current for a semiconductor light source, a technique known as direct modulation. The alternative to direct modulation which has found rather extensive application in optical communication through the atmosphere makes use of a cw light source and an external modulator. Both direct modulation and external modulation are considered viable alternatives for the high-data-rate bus, and both have been investigated during the course of this program.



3.2.1 Directly Modulated Semiconductor Laser

The commonly used light sources for fiber optic communications are the light emitting diode (LED) and the injection laser diode (ILD). The properties of these two types of light source can be contrasted with regard to their suitability for use in the wideband bus application. The modulation fall time of the LED is limited by the spontaneous lifetime of the current carriers (electrons and holes), which is about 5 ns in high-purity, single crystal GaAs. This limits the useful modulation bandwidth of LEDs to a few hundred MHz. Furthermore, the incoherent output of an LED cannot be coupled efficiently into a single-mode fiber or waveguide. The LED is therefore not a practical light source for multigigahertz fiber optic systems. The ILD, on the other hand, is characterized by a stimulated carrier lifetime, which can be much shorter than the spontaneous lifetime. Further, the coherent output of an ILD which emits predominantly in a single spatial mode can be coupled efficiently into single-mode waveguides and fibers. Thus, the ILD is considered to be the only suitable candidate for use in the wideband bus application.

The response of an ILD to a time-varying current waveform is described in terms of two coupled first-order differential equations which relate the carrier and photon densities to the independent variable time. These rate equations can be written in the form²⁶⁻²⁸

$$\frac{dZ}{dt} = \frac{1}{\tau} [n - Z - XZ^2] \quad (3.4)$$

$$\frac{dX}{dt} = r [X(Z^2 - 1) + \alpha Z] \quad (3.5)$$

where

Z is the electron-hole density in the active (lasing)/region,
normalized to unity at the threshold for lasing,

X is the normalized photon density in the laser cavity,

η is the driving current, normalized to unity at the threshold for lasing,

α is the fraction of the photons emitted spontaneously which couple into the lasing mode,

$$T = t/(\tau_{sp}\tau_{ph})^{1/2},$$

t is the time (in seconds),

λ is a constant which determines the dependence of laser gain on carrier density,

$$r = (\tau_{sp}/\tau_{ph})^{1/2}, \text{ where}$$

τ_{sp} is the spontaneous-emission lifetime for electron-hole pairs, and

τ_{ph} is the photon lifetime in the cavity.

If the laser is initially unbiased, with $X = Z = \eta = 0$, and is excited by a step increase in current η_0 , such that $\eta_0 > 1$, then the onset of lasing is delayed by the time t_d , required for the carrier density Z to increase from 0 to 1. The value of t_d , obtained by solving (3.4) with $X \equiv 0$ is given by

$$t_d = \tau_{sp} \ln [\eta_0/(\eta_0 - 1)] \quad . \quad (3.6)$$

This delay is typically of the order of several nanoseconds and is obviously too great to allow for gigabit transmission. It is, therefore, necessary to supply a dc current to prebias the laser near, or even above, the lasing threshold. This makes subnanosecond response possible.

In order to obtain a reliable prediction of the laser response, it is important to determine values for the quantities τ_{sp} , τ_{ph} , λ and α which appear



ERC41015.4FR

in the rate equations as accurately as possible. Unfortunately, this is not a simple matter, as there is some disagreement in the literature with regard to how these parameters should be determined. For example, values for the constant α from 1 to 3 are commonly used in laser response calculations.

A set of simple formulas was used to determine values for τ_{sp} , τ_{ph} , and α for calculating the laser response. These formulas are based on empirical data on double-heterostructure $\text{Ga}_x\text{Al}_{1-x}\text{As}$ lasers.²⁹ First, the gain g is assumed to vary as

$$g = \alpha n^2 - \beta, \quad (3.7)$$

where α and β are constants and n is the carrier density. From empirical information it is determined that, for $\beta = 100 \text{ cm}^{-1}$, the threshold condition $g = 0$ is obtained for $n = 10^{18} \text{ cm}^{-3}$. From this information and (3.7), it is determined that

$$\alpha = 10^{-34} \text{ cm}^5.$$

Thus, the threshold current density n_{th} can be written

$$n_{th} = \left(\frac{\beta}{\alpha} \right)^{1/2}.$$

The spontaneous lifetime is given by

$$\tau_{sp} = \frac{n_{th} \Gamma d}{J_{th}},$$

where Γ is the photon confinement factor, $e = 1.6 \times 10^{-19} \text{ C}$ is the electronic charge, d is the thickness of the junction, and J_{th} is the threshold current density for the laser. Using the values $J_{th} = 1.5 \times 10^3 \text{ A/cm}^2$, $d = 0.3 \text{ }\mu\text{m}$, $\Gamma = .8$, and $n_{th} = 1 \times 10^{18}$, it is found that

$$\tau_{sp} = 2.6 \text{ ns.}$$

In general, it will be assumed that τ_{sp} is inversely proportional to n_{th} , as described by the relation

$$\tau_{sp} = K_1/n_{th} \quad ,$$

with

$$K_1 = 2.6 \times 10^9 \text{ s/cm}^3 \quad .$$

This also implies that

$$J_{th} = \frac{n_{th}^2 \text{red}}{K_1} \quad ,$$

or, for $d = 0.3 \text{ } \mu\text{m}$ and $\Gamma = 0.8$,

$$J_{th} = K_2 n_{th}^2 \quad ,$$

with

$$K_2 = 1.5 \times 10^{-33} \text{ A-cm}^4 \quad .$$

The photon lifetime in the cavity is given simply by

$$\tau_{ph} = \frac{\bar{n}}{c\beta} \quad ,$$

where \bar{n} is the group refractive index (~ 5 for GaAs)²⁵ and $c = 3.0 \times 10^{10} \text{ cm/s}$ is the velocity of light in free space.

The constant β , which represents the loss coefficient for light propagating in the laser cavity, is an important parameter in our model, as its value affects τ_{ph} , τ_{sp} , and the threshold current density J_{th} . It is possible to change the value of β by changing the mirror reflectance, for example. The effect of changes in β on the laser parameters is described by the relations,



ERC41015.4FR

$$\tau_{sp} = K_3 / B^{1/2} \quad (3.8)$$

$$\tau_{ph} = K_4 / B \quad (3.9)$$

$$J_{th} = K_5 B \quad (3.10)$$

derived from results of preceding paragraphs, with

$$K_3 = 2.6 \times 10^{-8} \text{ s/cm}^{1/2}$$

$$K_4 = 1.7 \times 10^{-10} \text{ s/cm}$$

$$K_5 = 15 \text{ A/cm} \quad .$$

Thus, increasing B decreases both the spontaneous lifetime and photon lifetime, but causes the threshold current density to increase.

The preceding three equations will be used in investigating the response of the laser to modulating current pulses. The final parameter is the fraction of spontaneous emission coupled into lasing modes, α . An empirical formula²⁸ which agrees reasonably well with theoretical calculations is

$$\alpha = K_6 / V \quad ,$$

where V is the volume of the laser cavity, and

$$K_6 = .02 (\mu\text{m})^3 = 2 \times 10^{-14} \text{ cm}^3 \quad .$$

Thus, for example, for a laser cavity with the dimensions $1 \mu\text{m} \times 1 \mu\text{m} \times 500 \mu\text{m}$, a value of α of 4×10^{-5} is calculated from the preceding formula.

The preceding results will now be used to calculate the response of a laser diode to particular current waveforms. First the response of an initially unbiased laser to a step increase in current to a value above lasing threshold will be considered. The initial conditions are

$$X = Z = \eta = 0 \quad T < 0$$

$$\eta = \eta_0 > 1 \quad T > 0$$

The normalized photon density Z (which is proportional to the optical output power), carrier density X , and current η , are plotted as a function of time for this laser in Fig. 3.2, for a step increase in current to twice the threshold value, i.e., to $\eta = 2$. Note that the carrier density builds up to the threshold value $Z = 1$ over a time t_d , and the photon density then begins to increase rapidly. This is followed by rapid oscillations in both X and Z . These oscillations, known as relaxation oscillations, are important to the modulation of lasers at high speeds. The inverse of the temporal period is an indication of the maximum rate at which the lasers can be modulated. Also, as mentioned earlier, the delay time for the carrier density to build up from zero to lasing threshold must be eliminated for high data rate modulation. This is accomplished by applying a dc bias current at or slightly above threshold.

The temporal response of a dc-biased laser to a series current pulses is given in Figs. 3.3 - 3.5. In each case, the normalized current increases from 1.05 to a maximum of 2.0, with rise and fall times of 35 ps and an interval of 25 ps between pulses. The difference between the three plots is the pulse duration - 380 ps in Fig. 3.3, 350 ps in Fig. 3.4, and 410 ps in Fig. 3.5. Note that there is a particular pulse width at which the carrier density at the end of the pulse return to the value at the onset of the pulse. This is the desired pulse width for high-data-rate modulation, as illustrated in the plots of Fig. 3.3. If the initial carrier density is different for consecutive pulses, the pulse amplitude will also change on a pulse-to-pulse basis, as in Figs. 3.4 and 3.5. On the other hand, if the carrier density returns to its



Fig. 3.2 Response of injection laser to a step increase in driving current to twice the threshold current, with $\tau_{sp} = 2.6$ ns, $\tau_{ph} = 1.7$ ps, $\alpha = 4 \times 10^{-5}$, $\chi = 2$. Stimulated emission begins when the normalized carrier density reaches unity, approximately 2 ns after the current step is applied.

ERC41015.4F2

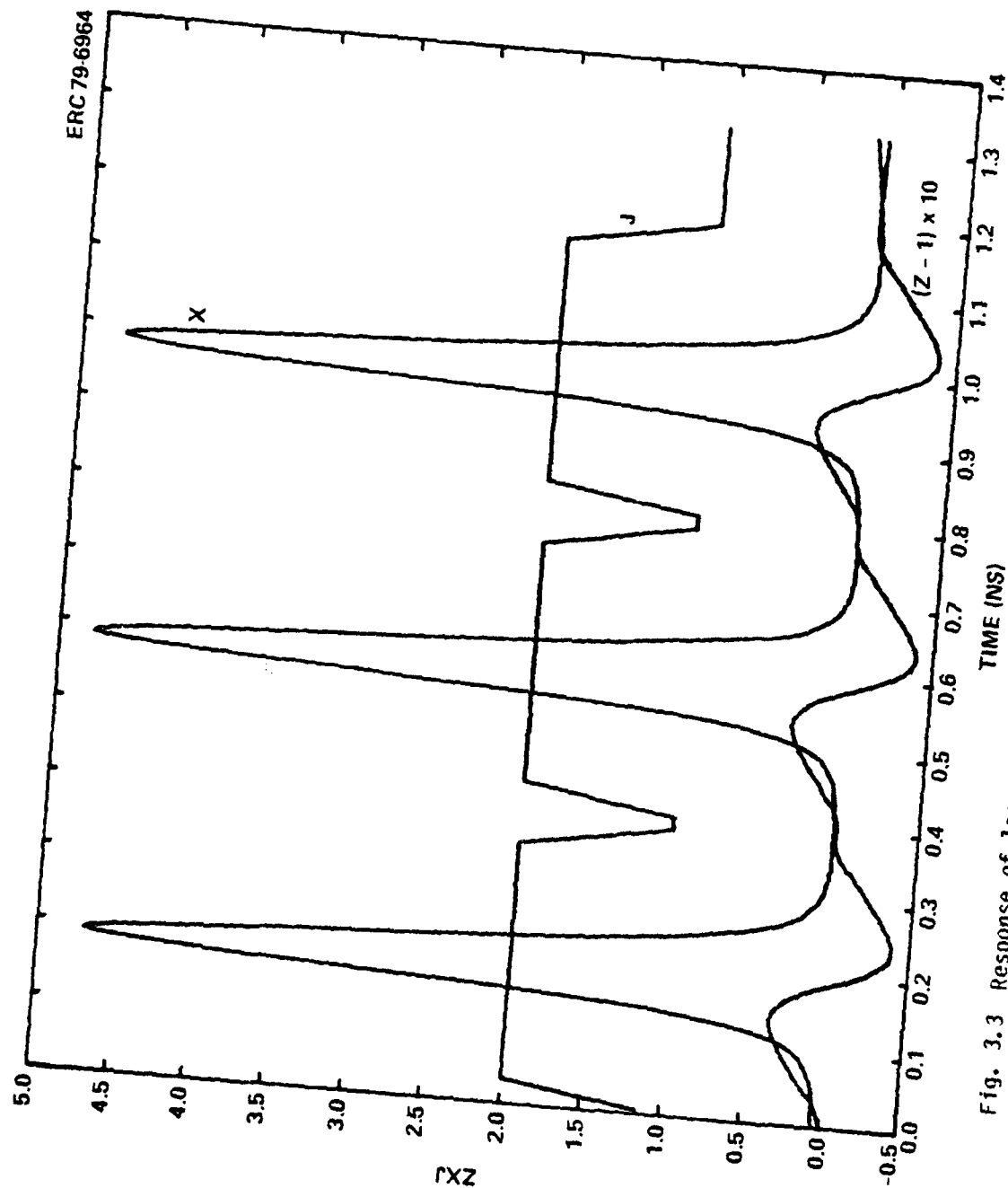


Fig. 3.3 Response of laser to three successive current pulses. A dc bias current of 1.05 the threshold value is applied, and the carrier and photon densities are in equilibrium at initiation of the first pulse. Other parameters are the same as in Fig. 3.2.



Rockwell International

ERC41015.4FR

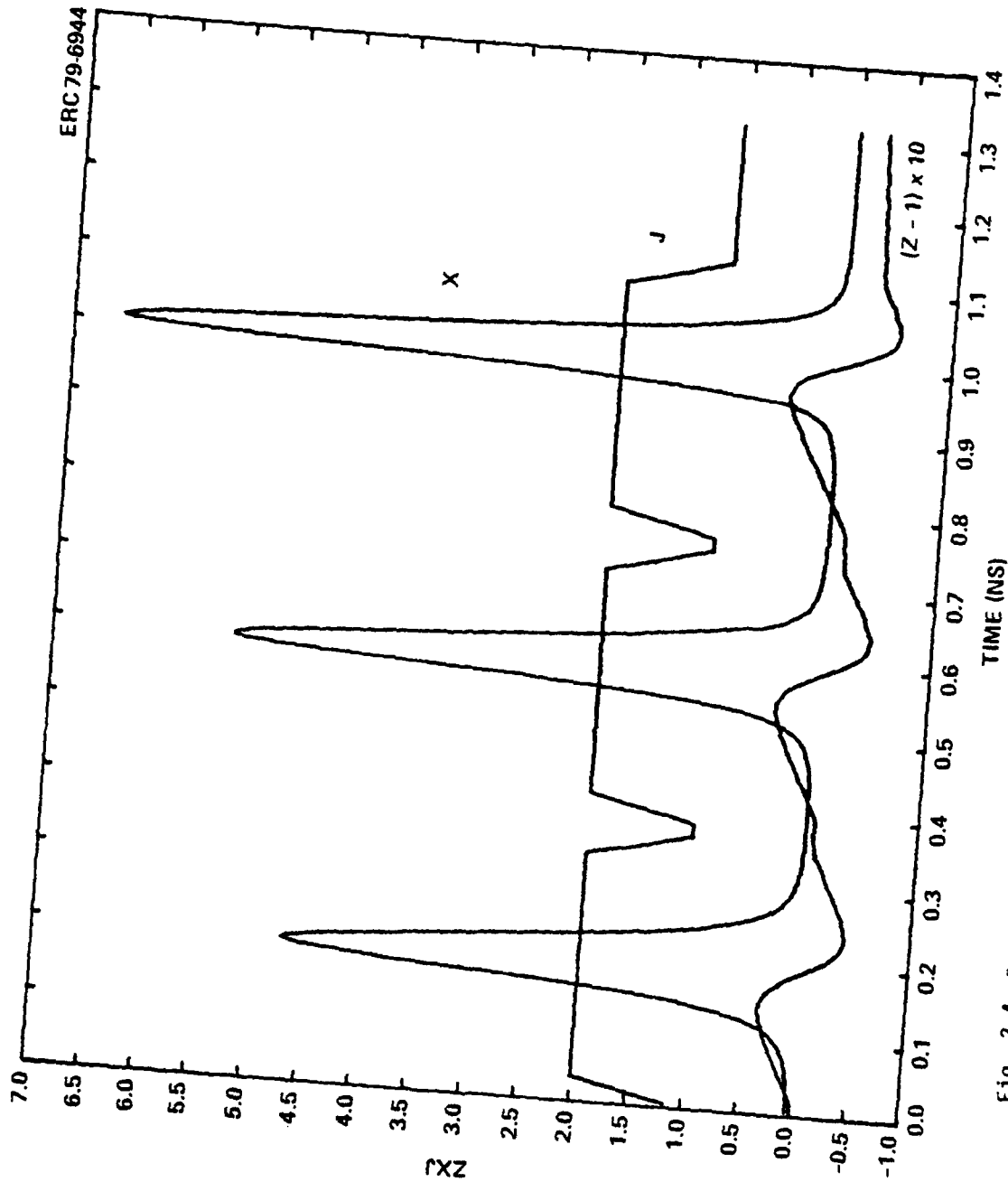


Fig. 3.4 Response of laser to three successive current pulses of slightly shorter duration than in Fig. 3.3, illustrating the sensitivity of laser response to pulse width.

ERC41015.4FR

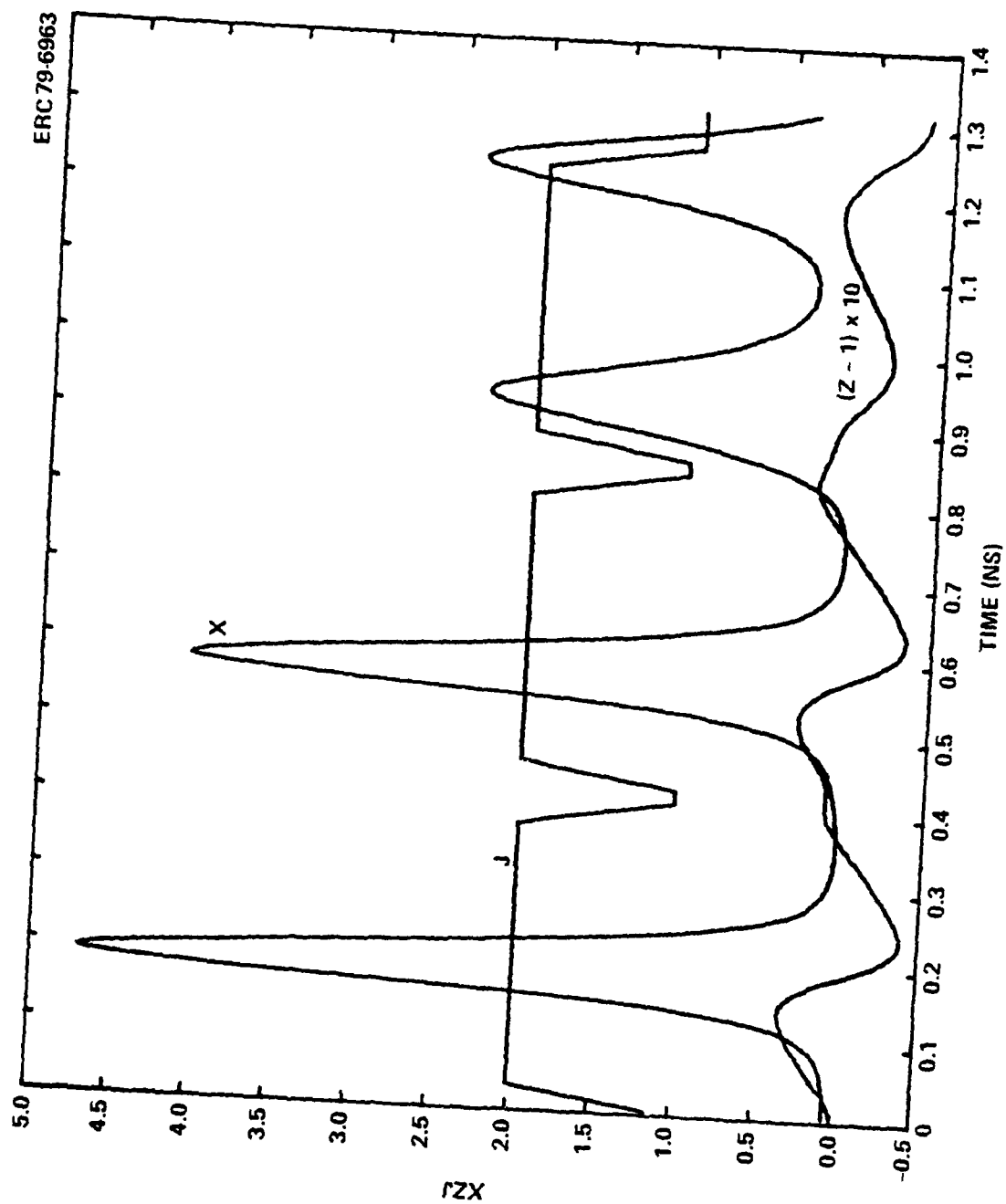


Fig. 3.5 Response of laser to successive current pulses of slightly greater duration than those in Fig. 3.3.



Rockwell International

Science Center

ERC41015.4FR

equilibrium value at the end of each pulse, the amplitudes of successive pulses will be equal.

The high sensitivity of laser performance to pulse width illustrated in Figs. 3.3 - 3.5 is undesirable for a practical system, as it implies very tight tolerances on the performance of the driving electronics. Fortunately, it is possible to greatly reduce the sensitivity of the laser output to the characteristics of the current pulses by injecting cw light from another laser into the cavity of the modulated laser, as in the illustration of Fig. 3.6. Furthermore, this optical injection also gives a substantial improvement in the maximum digital data rate at which the laser can be modulated.

Mathematically, the current injection is described by modifying one of the two coupled laser rate equations, (3.5), to read

$$\frac{dX}{dt} = r[X(Z^2 - 1) + \alpha Z + Q], \quad (3.11)$$

where Q is a constant which reflects the rate of photon injection from the cw laser.²⁷ Note that if the carrier density $Z = 0$ for the modulated laser, the normalized photon density at equilibrium is given by $X = Q$.

Examples of the modulated output of the injection laser with current injection are illustrated in Figs. 3.7 and 3.8. The level of current injection $Q = 0.005$ corresponds to a photon injection of roughly 1% of the average number of photons emitted by the modulated laser. Note that the optical output tends to lag behind the current pulses in this case. This contrasts with the preceding results without current injection, in which it was necessary to have the current pulse extend well beyond the end of the photon pulse to obtain reproducible output on a pulse-to-pulse basis. The reason for this difference is that the equilibrium value for the normalized carrier density at lasing threshold is significantly less than unity with current injection, and the increase in photon density during the pulse can drive the carrier density from a value greater than one at the peak of the pulse down to its equilibrium value at the end of the pulse. The higher data rate with current injection results

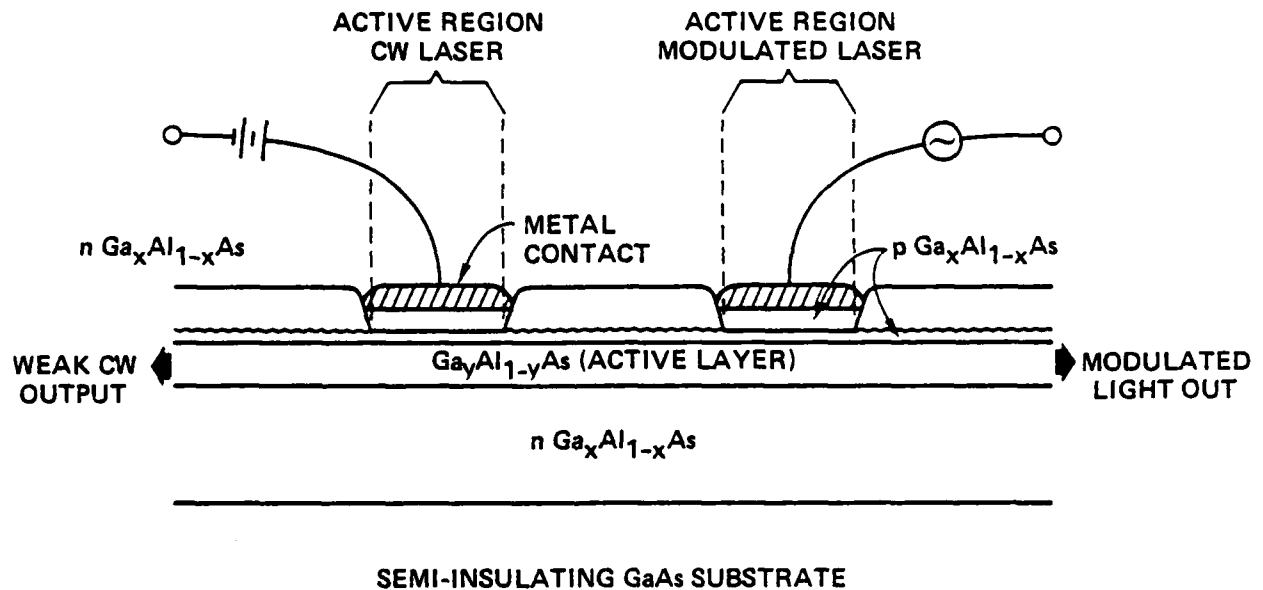


Fig. 3.6 Hypothetical configuration for two coupled distributed Bragg reflector (DBR) lasers, in which cw emission from one laser is coupled into a second, modulated laser. The purpose of the cw injection is to make the modulated laser less sensitive to small variations in the parameters of the driving pulse, and to increase the effective data rate of the transmitter.



Rockwell International

ERC41015.4FR

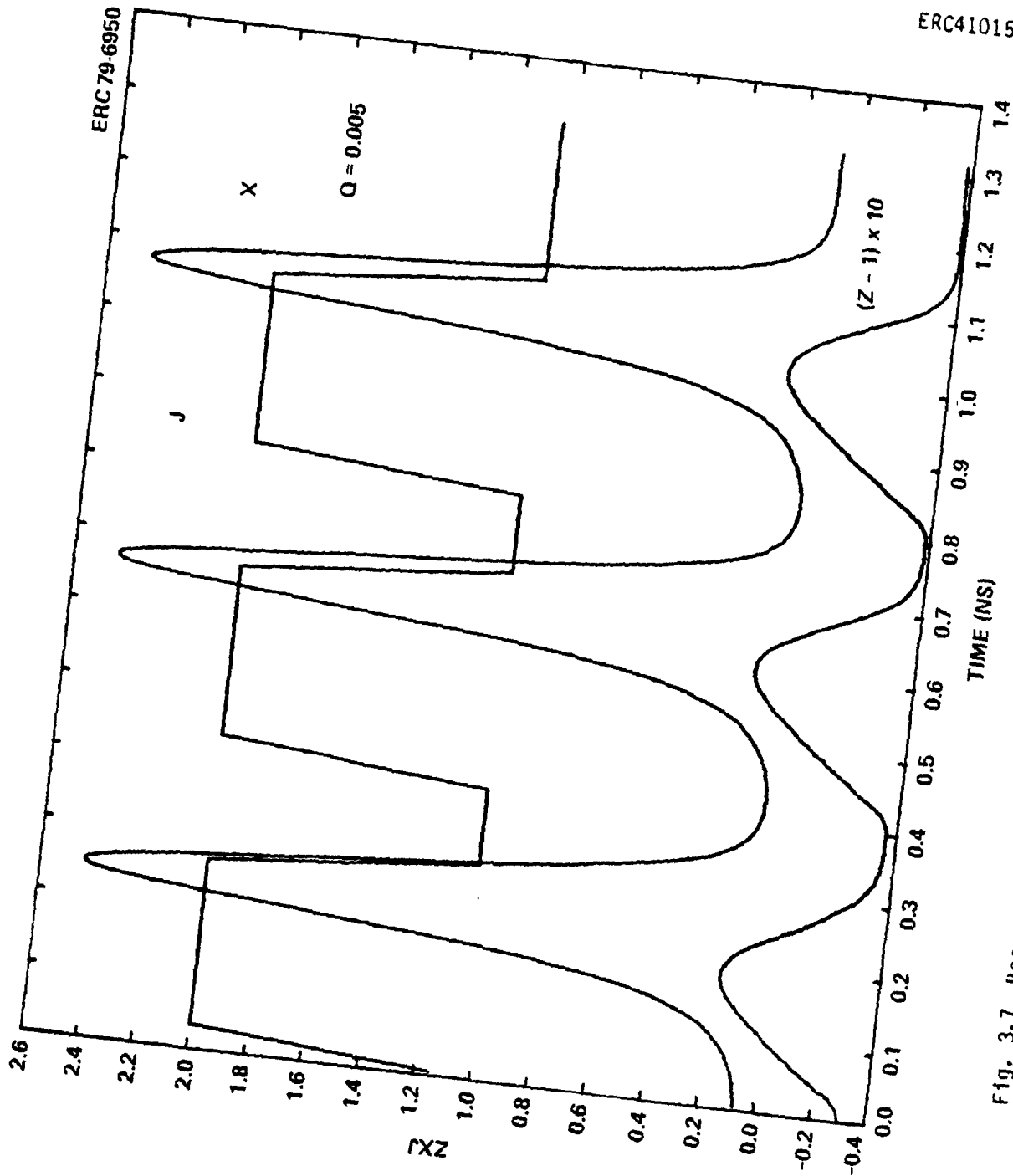
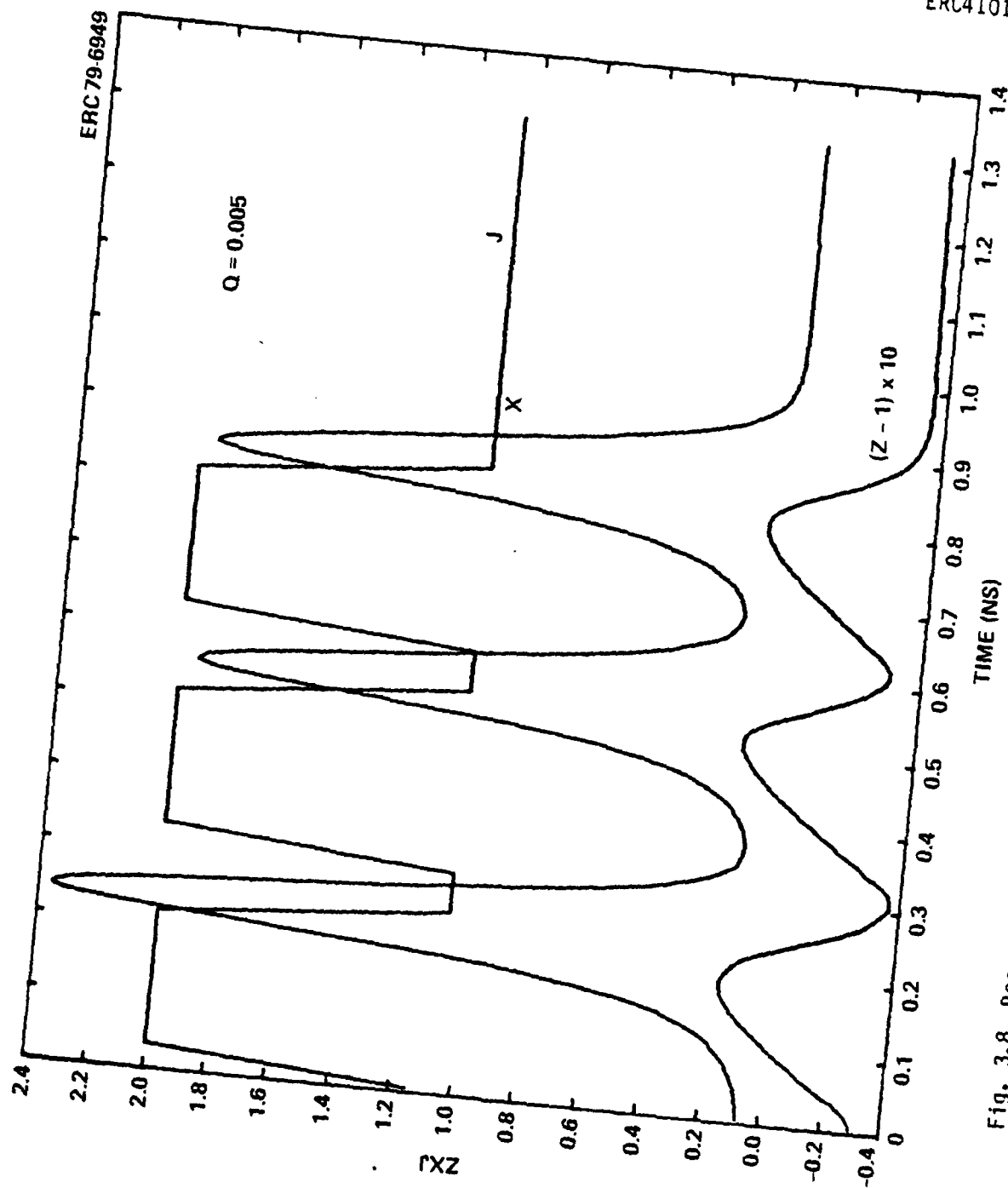


Fig. 3.7 Response of laser to successive current pulses, with cw photon injection ($Q = .005$). Other parameters are the same as in Fig. 3.2.



ERC41015.4FR

Fig. 3.8 Response of laser to successive current pulses. The pulses are about 25% shorter than in the preceding illustration, yet good stability is still maintained for the optical output on a pulse-to-pulse basis.



ERC41015.4FR

because it is not necessary to extend the driving current pulse beyond the end of the optical pulse to restore carrier equilibrium.

The pulse rate in the plots of Figs. 3.7 and 3.8 correspond to data rates of 2.5 Gbit/s and 3.3 Gbit/s, respectively. The data rate is further enhanced by increasing the attenuation in the cavity, β . It follows from (3.8) and (3.9) that increasing β causes a decrease in both τ_{sp} and τ_{ph} and both of these changes tend to increase the laser modulation bandwidth. The third effect is an increase in threshold current density. The final set of examples in Figs. 3.9 - 3.10 reflect an increase in β from 100 cm^{-1} , as in the previous examples, to 200 cm^{-1} . This results in a decrease in τ_{sp} from 2.6 ns to 1.8 ns, and in τ_{ph} from 1.7 ps to 0.85 ps, while J_{th} increases from 1500 A/cm^2 to 3000 A/cm^2 . The net effect is to increase the equivalent data rate from 3.3 Gbit/s, as in Fig. 3.8, to 5.3 Gbit/s, as in Fig. 3.9. Finally, in Fig. 3.10, the effect of increasing the modulation rate to above 6 Gbit/s is illustrated. Here the response of the carrier and photon densities to the modulating pulse is too slow to restore equilibrium at the end of the current pulse, so that there is a significant variation in amplitude on a pulse-to-pulse basis.

3.2.2 External Electrooptic Modulator

An alternative to the directly modulated semiconductor laser described in the preceding section is a cw laser with an external modulator. Of the various types of optical waveguide modulators which have been investigated, the channel waveguide electrooptic modulator offers the greatest potential for high-speed, low-power operation. To achieve bandwidths well in excess of 1 GHz, a traveling wave configuration in which the modulating electrical signal propagates in a microwave transmission line is needed. The transmission line is fabricated on the same electrooptic substrate which contains the optical waveguides, as illustrated in Fig. 3.11.

Some of the key factors in the design of the wideband modulator are phase matching of microwave and optical waves, attenuation and distortion of the modulating signal, and dielectric and optical parameters of the substrate

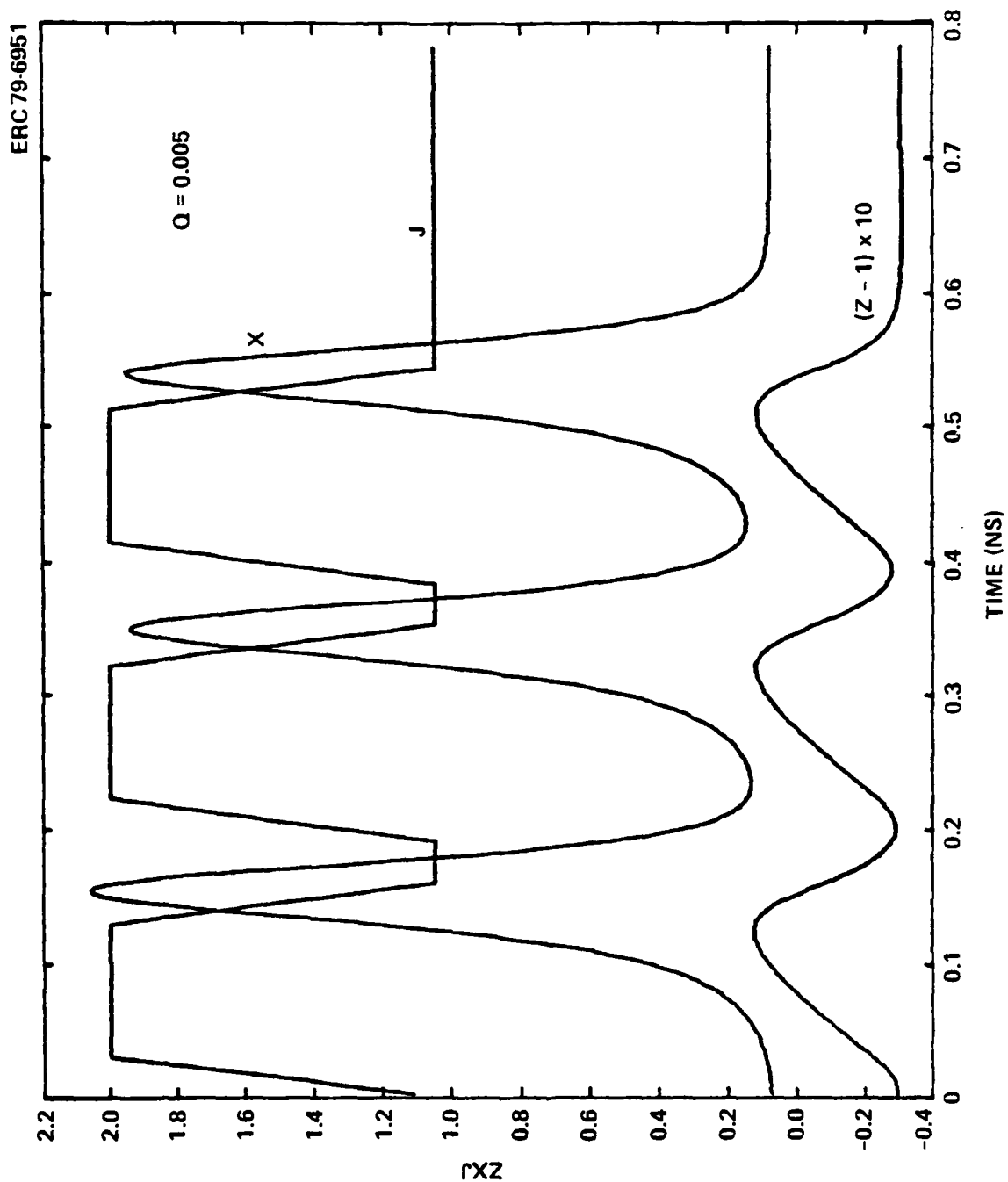


Fig. 3.9 Response of laser to successive current pulses, illustrating how increasing the cavity loss can increase the data rate. Values for the model parameters are $\tau_{ph} = 2.6\text{ns}$, $\tau_{sp} = 0.85\text{ns}$, $\alpha = 4 \times 10^{-5}$, $\ell = 2$, $Q = 0.005$, $\text{Eq. len} = 10$ in $5.3 \times 10^5 \text{t/s}$

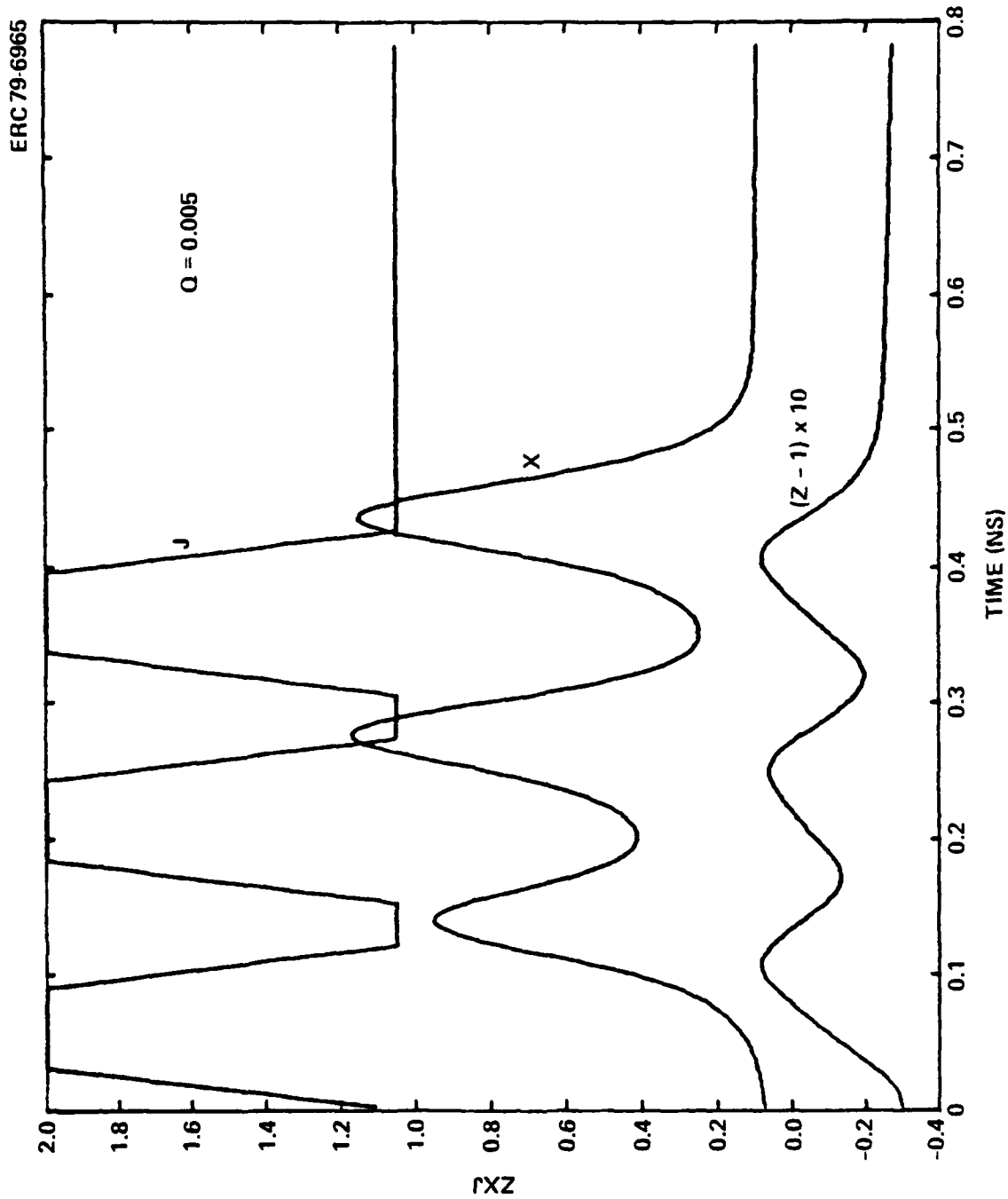


Fig. 3.10 Response of laser to series of pulses at an equivalent data rate of 6.5 Gbit/s, with other parameters the same as in Fig. 3.9. The pulse-to-pulse variations are an indication that the data rate capability of the laser has been exceeded.

TRAVELING WAVE ELECTROOPTIC MODULATOR

SC79-4143

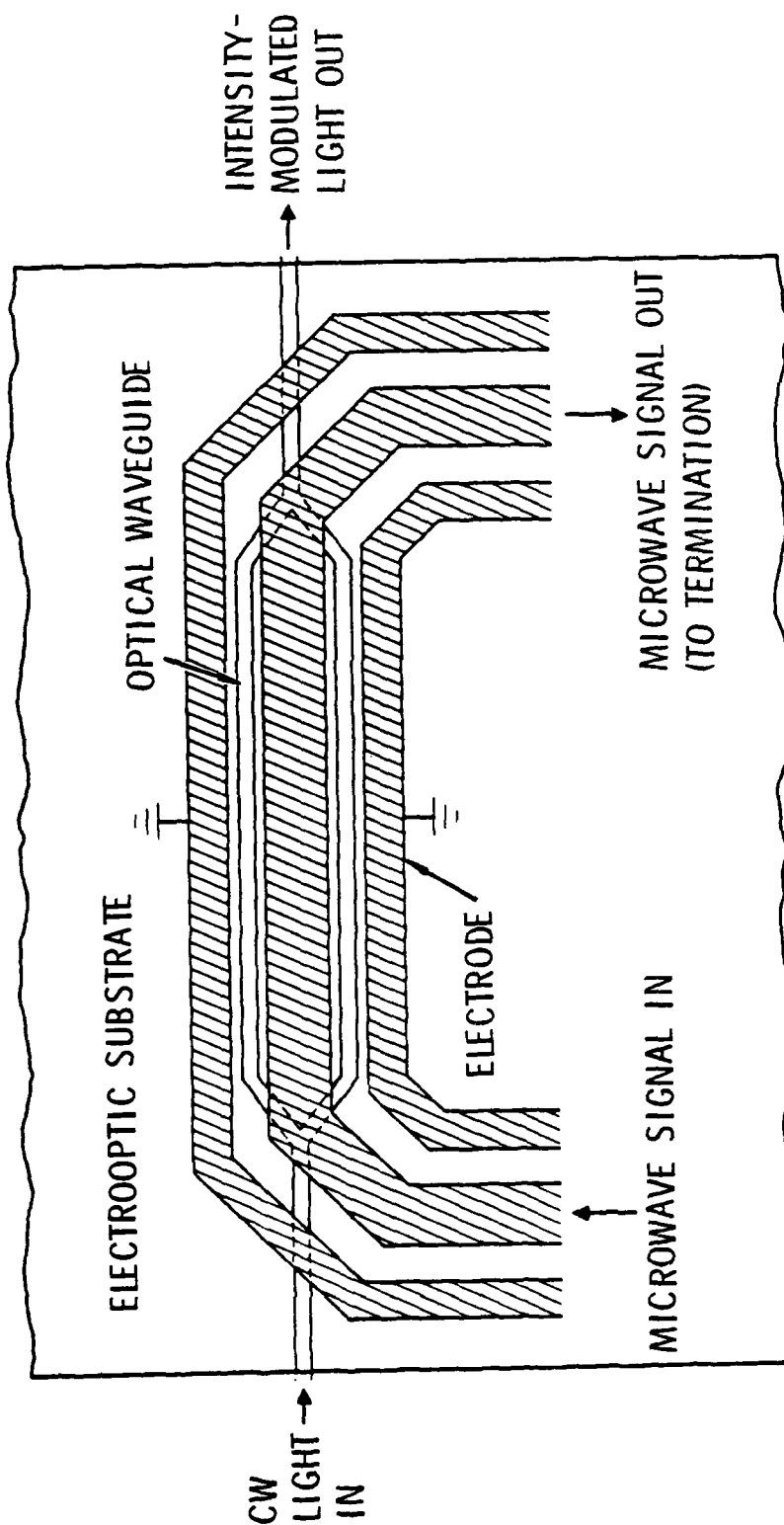


Fig. 3.11 Schematic diagram of a traveling wave electrooptic modulator.

ERC41015.4FR



ERC41015.4FR

material. Each of these aspects of modulator design and performance is discussed in some detail below.

3.2.2.1 Phase Matching of Microwave and Optical Signals

For operation of a wideband traveling wave optical modulator, it is desirable for the phase velocity of the optical wave v_o to be nearly equal to that of the modulating microwave signal v_m . If the phase velocities are not equal, then the phase mismatch for a given modulation frequency f_m increases as a function of distance along the length of the modulator. This phase mismatch limits the modulator bandwidth.

To explore the effect of phase mismatch on modulator performance, it will be assumed that the modulating wave produces a change in the effective refractive index ΔN of the electrooptic medium given by

$$\Delta N = \Delta N_o f(Z - v_m t) e^{-\alpha Z} \quad 0 < Z < L \quad (3.12)$$

where ΔN_o is the modulation amplitude for $Z = 0$, the shape of the modulating waveform is described by the function f , and the attenuation of the modulating signal amplitude as a function of distance is determined by the constant α . Then, the position Z of an optical phasefront which crosses the plane $Z = L$ at $t = t_o$ is given by

$$Z = v_o (t - t_o) + L$$

Substituting this result into (3.12) yields

$$\Delta N = \Delta N_o f\left[\left(1 - \frac{v_m}{v_o}\right) Z - v_m t_o + \frac{v_m}{v_o} L\right]$$

so that the total phase change as a function of time for the modulated wave $\Delta\phi(t_o)$ is

$$\Delta\phi(t_0) = \frac{2\pi}{\lambda} \int_0^L \Delta N dZ$$

or

$$\Delta\phi(t_0) = \frac{2\pi\Delta N_0}{\lambda} \int_0^L f \left[\left(1 - \frac{v_m}{v_0}\right) Z - v_m t_0 + \frac{v_m L}{v_0} \right] e^{-\alpha Z} dZ \quad (3.13)$$

The preceding derivation holds for an arbitrary temporal dependence $f(t)$ for the modulating waveform. If the modulating signal is sinusoidal, such that

$$f(Z, t) = \cos(k_m Z - \omega_m t)$$

with

$$k_m = \frac{\omega_m}{v_m},$$

and

$$v_m = 2\pi f_m,$$

where f_m is the frequency of the modulating signal, then f can be written

$$f(Z, t) = \cos \frac{\omega_m}{v_m} (Z - v_m t).$$

It then follows from (3.13) that

$$\Delta\phi(t) = \frac{2\pi\Delta N_0}{\lambda} \int_0^L \cos \left(qZ + \frac{\omega_m}{v_m} L - \omega_m t \right) e^{-\alpha Z} dZ \quad (3.14)$$

where q , defined by



ERC41015.4FR

$$q = \omega_m \left(\frac{1}{v_m} - \frac{1}{v_o} \right) \quad (3.15)$$

is a measure of the phase mismatch between the optical and modulating waves. Integrating (3.14) yields the result

$$\begin{aligned} \Delta\phi = \frac{\exp(-\alpha L)}{\alpha^2 + q^2} & [\sin \omega_m t' (-\alpha \sin qL - q \cos qL)] \\ & + \cos \omega_m t' (-\alpha \cos qL + q \sin qL) + q \sin \omega_m t' - \alpha \cos \omega_m t' \end{aligned}$$

with

$$t' = t_o - L/v_m$$

The amplitude $\Delta\phi$ of the modulated output at the frequency f_m is given by the square root of the sum of the squares of the sine and cosine terms; that is

$$\Delta\phi = \frac{2\pi\Delta N_o}{\lambda} [\exp(-2\alpha L) + 1 - 2 \cos qL \exp(-\alpha L)] (\alpha^2 + q^2)^{-1/2} \quad (3.16)$$

In the limit that the attenuation constant $\alpha \rightarrow 0$, this reduces to

$$\frac{\Delta\phi}{\Delta\phi_0} = \frac{2\pi\Delta N_o L}{\lambda} \frac{\sin(qL/2)}{(qL/2)}$$

For the case that $\alpha = 0$, the modulation depth falls to half its zero-frequency value for $\sin(qL/2)/(qL/2) = 1/2$, or $qL = 3.8$.

The phase shift given by (3.16) is plotted as a function of qL in Fig. 3.12 for $\alpha = 0$, $\alpha = 1/4 q$, $\alpha = 1/2 q$, $\alpha = q$, and $\alpha = 2 q$.

It is evident from the preceding discussion that the falloff in modulation effectiveness with frequency is determined by the value of the quantity qL , given by

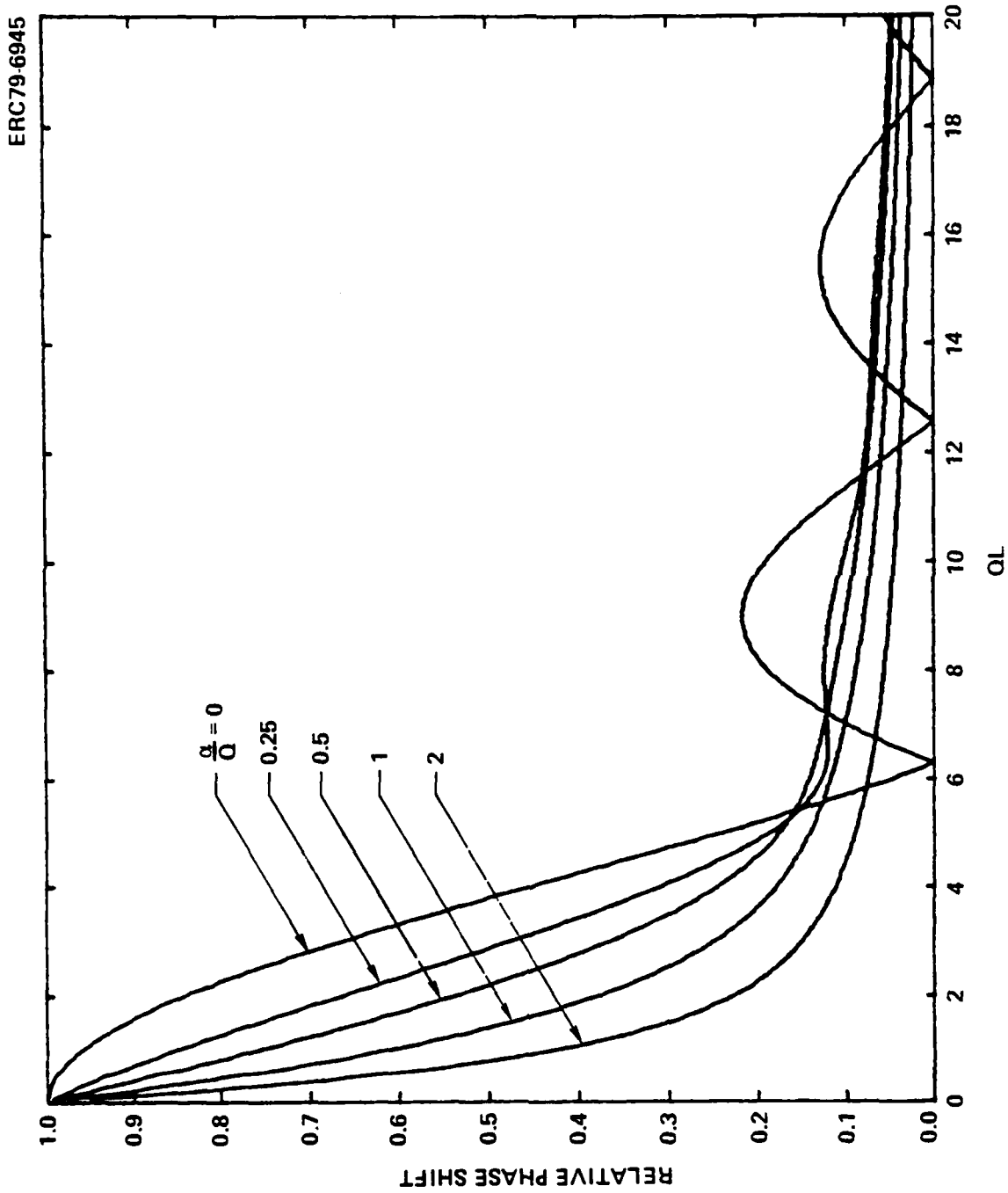


Fig. 3.12 Effect of the phase mismatch parameter QL on the relative phase shift of a traveling wave electrooptic modulator, for different values of the transmission line attenuation constant α .



$$qL = \omega_m \left(\frac{1}{v_m} - \frac{1}{v_0} \right) L$$

If the modulating region is short (i.e., $L \rightarrow 0$), then the modulation depth will not decrease appreciably with frequency. If the phase match is good ($v_m \approx v_0$) then $qL \rightarrow 0$ even for large values of L . In that case, the modulation depth will decrease with frequency as a result of an increase in the microwave attenuation α with frequency. If the phase mismatch is poor, on the other hand, the falloff in modulation depth with frequency will be determined by the increase in qL as ω increases.

3.2.2.2 Attenuation and Distortion of Microwave Signal

As indicated in the preceding discussion, if the phase match is good between the modulating signal and the optical wave, the increase in attenuation of the microwave signal with frequency is the factor which limits the bandwidth of a modulator of given length. This loss arises from ohmic dissipation in the modulator electrodes as well as from the dielectric loss in the electrooptic material. Usually, however, the electrode losses are dominant. At high frequencies, the current is confined to a region near the surface of the opposing electrodes in a thin layer of depth σ , known as the skin depth. The skin depth decreases as the inverse square root of the modulating frequency, leading to an increase in resistance with frequency, the "skin effect."

As a result of the skin effect, a voltage pulse injected into an electrical transmission line will not only be attenuated, but will also be broadened as it propagates.³² The starting point for analyzing the propagation of such a pulse is the transmission line equation

$$\frac{V(Z)}{V(0)} = e^{-\gamma Z}, \quad (3.17)$$

where $V(Z)$ is the voltage amplitude, and

$$\gamma = \sqrt{(R + j\omega L)(j\omega C)} \quad (3.18)$$

where R , L , and C are, respectively, the resistance, inductance, and capacitance per unit length for the transmission line. As a result of the skin effect, the resistance per unit length increases at high frequencies according to

$$R = R_{sk} \sqrt{S} \quad ,$$

where R_{sk} is a constant determined by the electrode conductivity and dimensions, and

$$S = j\omega \quad .$$

Substituting these expression into (3.18) yields

$$\gamma = \sqrt{-\omega^2 LC - \frac{1}{\sqrt{2}} \omega^{3/2} R_{sk} C + \frac{j}{\sqrt{2}} \omega^{3/2} R_{sk} C}$$

or

$$\gamma = i\omega \sqrt{LC} \sqrt{1 + (1 - j)(R_{sk}/\sqrt{2}\omega L)} \quad .$$

It is now possible to use Fourier analysis to determine the evolution of an incident pulse as it propagates along the transmission line. A Gaussian shape for the incident pulse $f(0,t)$ of the form

$$f(0,t) = \frac{1}{\sqrt{\pi\tau}} e^{-t^2/\tau^2}$$

will be assumed, where the pulse amplitude is normalized such that

$$\int_{-\infty}^{\infty} f(0,t) dt = 1 \quad .$$

The Fourier transform of this pulse shape is given by

$$F(0,\omega) = \frac{1}{\sqrt{2\pi}} \int_{-\infty}^{\infty} f(0,t) \cos \omega t dt \quad ,$$



which is evaluated for the Gaussian pulse to be

$$F(0, \omega) = \frac{1}{\sqrt{2\pi}} e^{-\omega^2 \tau^2 / 4} .$$

Then, a distance z down the transmission line,

$$F(z, \omega) = e^{-\gamma z} F(0, \omega) .$$

Finally, the temporal shape of the propagating pulse $f(z, t)$ is determined from

$$f(z, t) = \frac{1}{\sqrt{2\pi}} \int_{-\infty}^{\infty} F(t, \omega) e^{j\omega t} d\omega .$$

It is possible to rewrite this in the form

$$f(z, t) = \frac{1}{2\pi} \int_{-\infty}^{\infty} e^{-\omega^2 \tau^2 / 4 - |B|z + j\omega t - jAz} , \quad (3.19)$$

with

$$A = \omega \sqrt{LC} \operatorname{Re} \sqrt{1 + \frac{(1 - j) R_{Sk}}{\sqrt{2\omega} L}} \quad (3.20)$$

$$B = \omega \sqrt{LC} \operatorname{Im} \sqrt{1 + \frac{(1 - j) R_{Sk}}{\sqrt{2\omega} L}} \quad (3.21)$$

With these substitutions $f(z, t)$ simplifies to

$$f(z, t) = \frac{1}{\pi} \int_0^{\infty} \cos(\omega t - Az) e^{-\omega^2 \tau^2 / 4} e^{-Bz} d\omega . \quad (3.22)$$

This integral cannot be evaluated in closed form because of the dependence of A and B on ω , but numerical integration on a digital computer is straightforward. Some plots showing the temporal evolution of pulses on a transmission line using specific materials parameters are given in the next section.

3.2.2.3 Materials Considerations

The materials of primary interest for external modulators are the semi-conductors GaAs/Ga_xAl_{1-x}As and the ferroelectric insulators LiNbO₃ and LiTaO₃. Some of the key parameters of these materials are summarized in Table 3.1. The two figures of merit n^3r and n^6r^2/ϵ are inversely proportional to the modulating voltage and the modulating power, respectively, for a phase matched modulator of a given physical configuration. Thus, a phase matched modulator of given length in GaAs would require roughly six times more voltage and ten times as much power as a modulator of the same length, electrode spacing, and waveguide dimensions in the ferroelectrics.

Table 3.1

Properties of Electrooptic Materials

Material	r_{33}^a ($\times 10^{-12}$ m/V)	r_{41}^a ($\times 10^{-12}$ m/V)	n^a	ϵ	n^3r ($\times 10^{-12}$ m/V)	n^6r^2/ϵ ($\times 10^{-24}$ m ² /V ²)
GaAs		1.2	3.6	13.2	56	237
LiNbO ₃	30.8		2.19 ^b	34.5 ^c	315	2871
LiTaO ₃	30.3		2.19 ^b	42 ^c	316	2378

a. Data for GaAs at $\lambda = 0.9$ μ m; for other materials at $\lambda = 0.63$ μ m.

b. n_3

c. $\epsilon = (\epsilon_1\epsilon_3)^{1/2}$.

While the larger electrooptic coefficients tend to favor the use of the ferroelectrics as modulator materials, the phase-matching criterion tends to support the use of GaAs. The optical phase velocity is given by

$$v_o = \frac{c}{n},$$

while, for "embedded" electrodes completely surrounded by dielectric,

$$v_m = \frac{c}{\sqrt{\epsilon}}.$$



On the other hand, for a coplanar structure with electrodes on the surface of the dielectric and air above,

$$v_m = \sqrt{\frac{2}{\epsilon + 1}} c$$

The key parameters related to phase matching for GaAs, LiNbO₃, and LiTaO₃ are summarized in Table 3.2. Note in particular the values of $|v_m^{-1} - v_o^{-1}|$, which is a measure of the phase mismatch, are much smaller in GaAs, and this quantity almost vanishes in GaAs for "embedded" electrodes. This means that, for a given modulator length, the maximum bandwidth consistent with the phase matching requirement is much higher in GaAs.

Table 3.2

Phase Matching for Traveling Wave Modulators

Material	v_o (cm/s)	Embedded Electrodes		Coplanar Electrodes	
		v_m (cm/s)	$v_m^{-1} - v_o^{-1}$ (s/cm)	v_m (cm/s)	$v_m^{-1} - v_o^{-1}$ (s/cm)
GaAs	8.25×10^9	8.33×10^9	-1.1×10^{-12}	1.13×10^{10}	-3.27×10^{-11}
LiNbO ₃	1.37×10^{10}	5.11×10^9	1.23×10^{-10}	7.12×10^9	6.75×10^{-11}
LiTaO ₃	1.37×10^{10}	4.63×10^9	1.42×10^{-10}	6.55×10^9	7.98×10^{-11}

It is useful to calculate the amplitude of the electrooptic interaction for a specific electrode configuration and dimensions. A simple model for an interferometric modulator illustrated in Fig. 3.13 will be assumed, in which the electrodes and optical waveguides are embedded in the substrate material. Neglecting fringing fields and the nonuniform electrode current distribution in the y-direction, the constant R_{Sk} for the transmission line can be written

$$R_{Sk} = \frac{1}{W} \sqrt{\rho \mu_0}$$

ERC41015.4FR

ERC79-6977

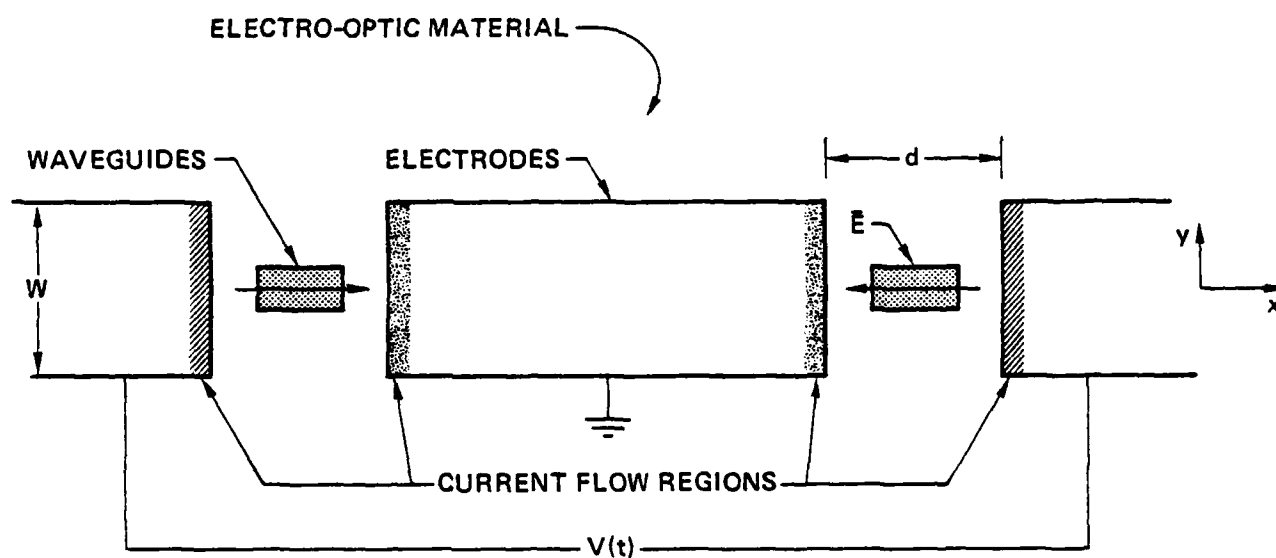


Fig. 3.13 Model for calculating response of traveling wave modulator, with electrodes embedded in the substrate.



where $\mu_0 = 4\pi \times 10^{-9}$ H/cm is the permeability of free space, W is the electrode height, and ρ is the electrode resistivity. On the other hand, the inductance per unit length is

$$L \approx \frac{\mu_0 d}{2W} ,$$

where d is the electrode separation. For gold electrodes, with $\rho = 2.2 \times 10^{-6}$ Ω -cm at room temperature, the quantity R_{Sk}/L which appears in equations (3.20) and (3.21) for the transmission line parameters A and B , is given by

$$R_{Sk}/L = 2.64 \times 10^5 \text{ (cm/H)}^{1/2}/d ,$$

where d is expressed in microns. The other parameter which appears in those equations is \sqrt{LC} , which is given by

$$\sqrt{LC} = \sqrt{\mu_0 \epsilon} = 1/v_m .$$

Values of v_m for GaAs, LiNbO₃ and LiTaO₃ appropriate to the embedded electrode structure of Fig. 3.13 are given in the third column of Table 3.2.

The temporal behavior of a Gaussian pulse injected into a transmission line of the type illustrated in Fig. 3.13 has been calculated for different lengths along the line by numerical integration of Eq. (3.22). Results are illustrated in Figs. 3.14 - 3.17 using values for the parameter τ of 25 and 50 ps, with materials parameters appropriate to LiNbO₃ and GaAs.

Modulation efficiency is determined by integrating the voltage amplitude experienced by a particular phase front along the entire length of the transmission line; that is,

$$\Delta\phi \propto \int_0^L f(\ell(t), t) d\ell ,$$

where

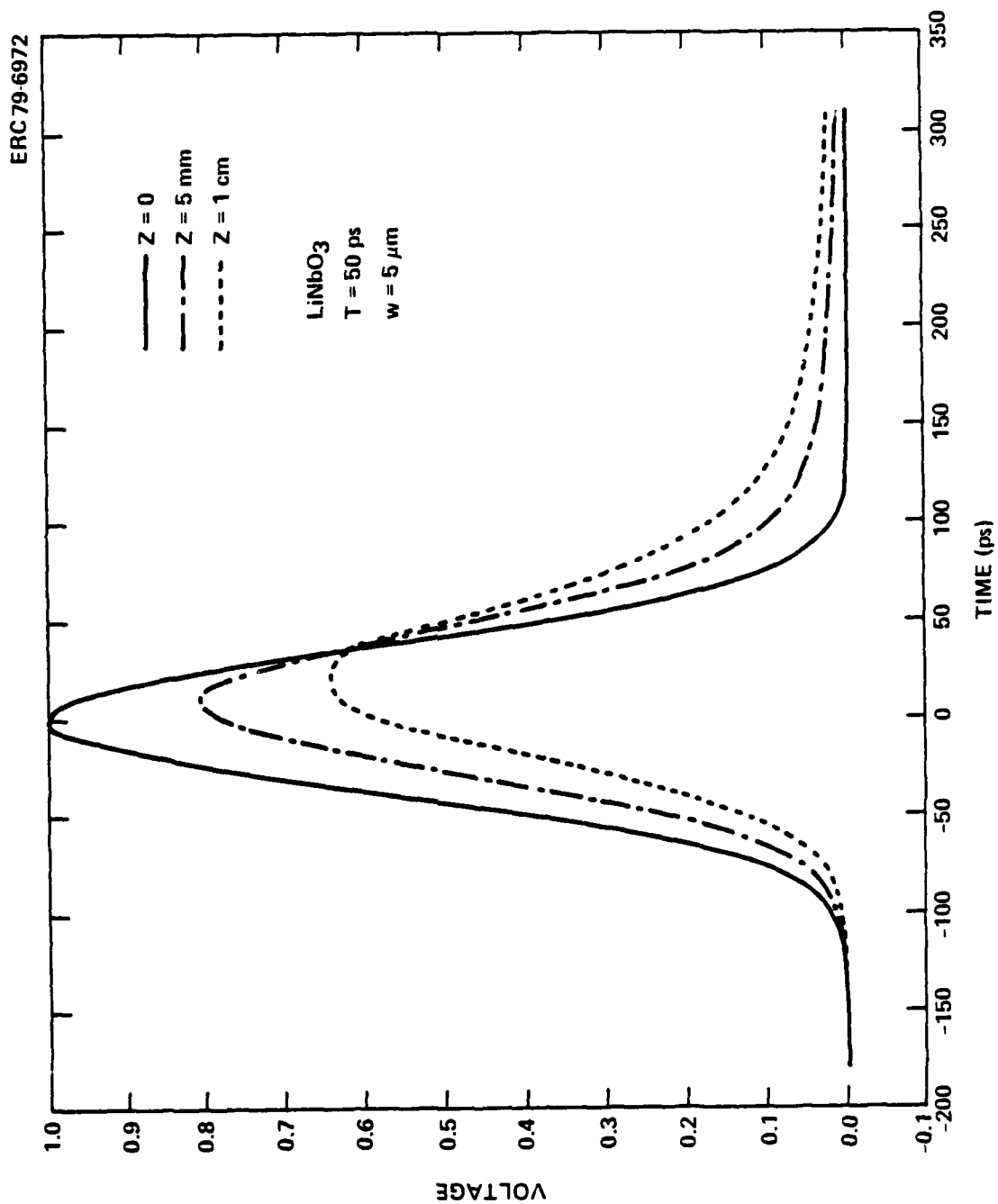


Fig. 3.14 Evolution of voltage pulse along a LiNbO_3 transmission line of the type illustrated in Fig. 3.13, with $\tau = 50 \text{ ps}$.



ERC41015.4FR

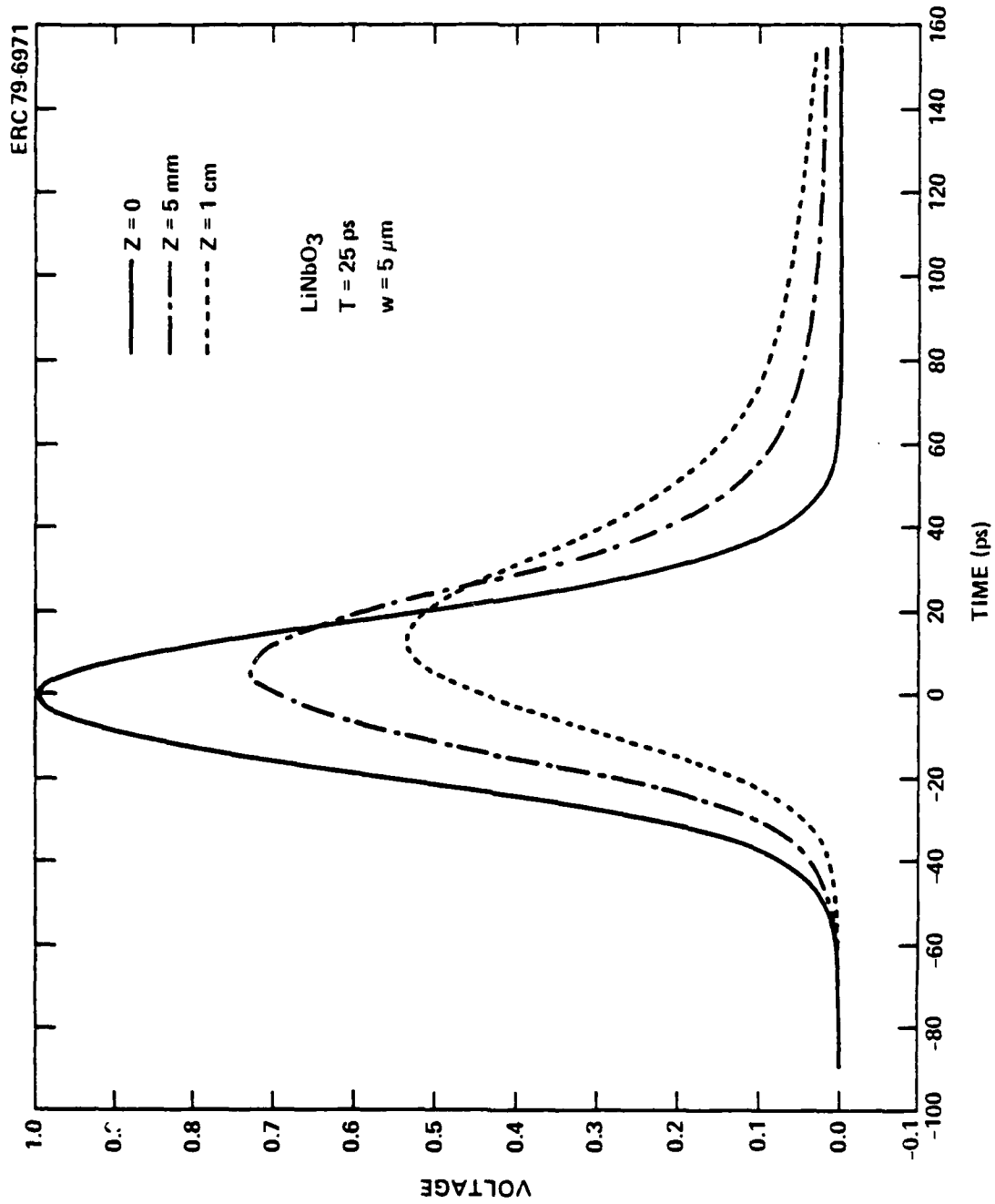
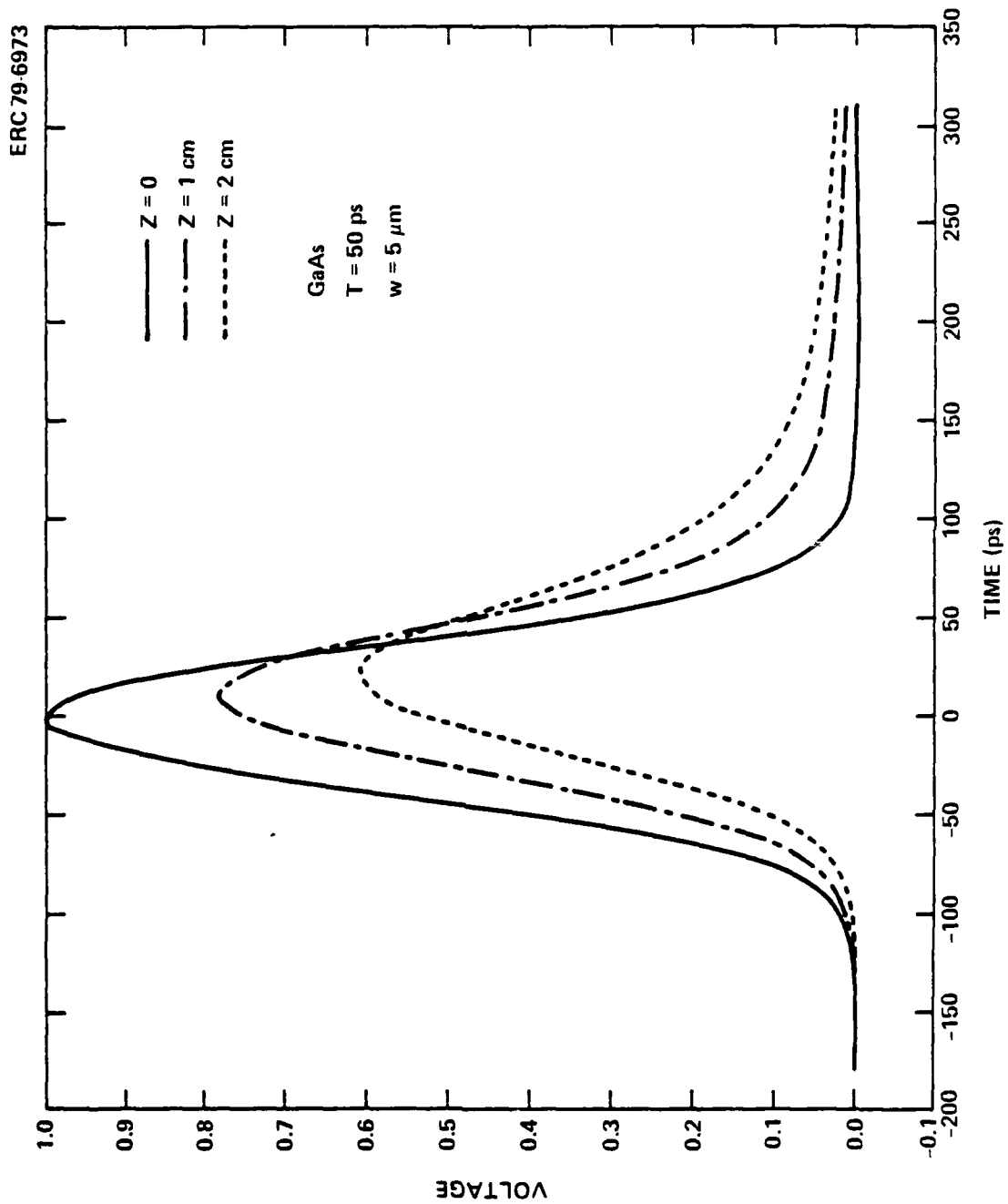


Fig. 3.15 Pulse evolution on a LiNbO_3 transmission line, with $\tau = 25 \text{ ps}$.

Fig. 3.16 Pulse evolution on a GaAs transmission line, with $\tau = 50 \text{ ps}$.



ERC41015.4FR

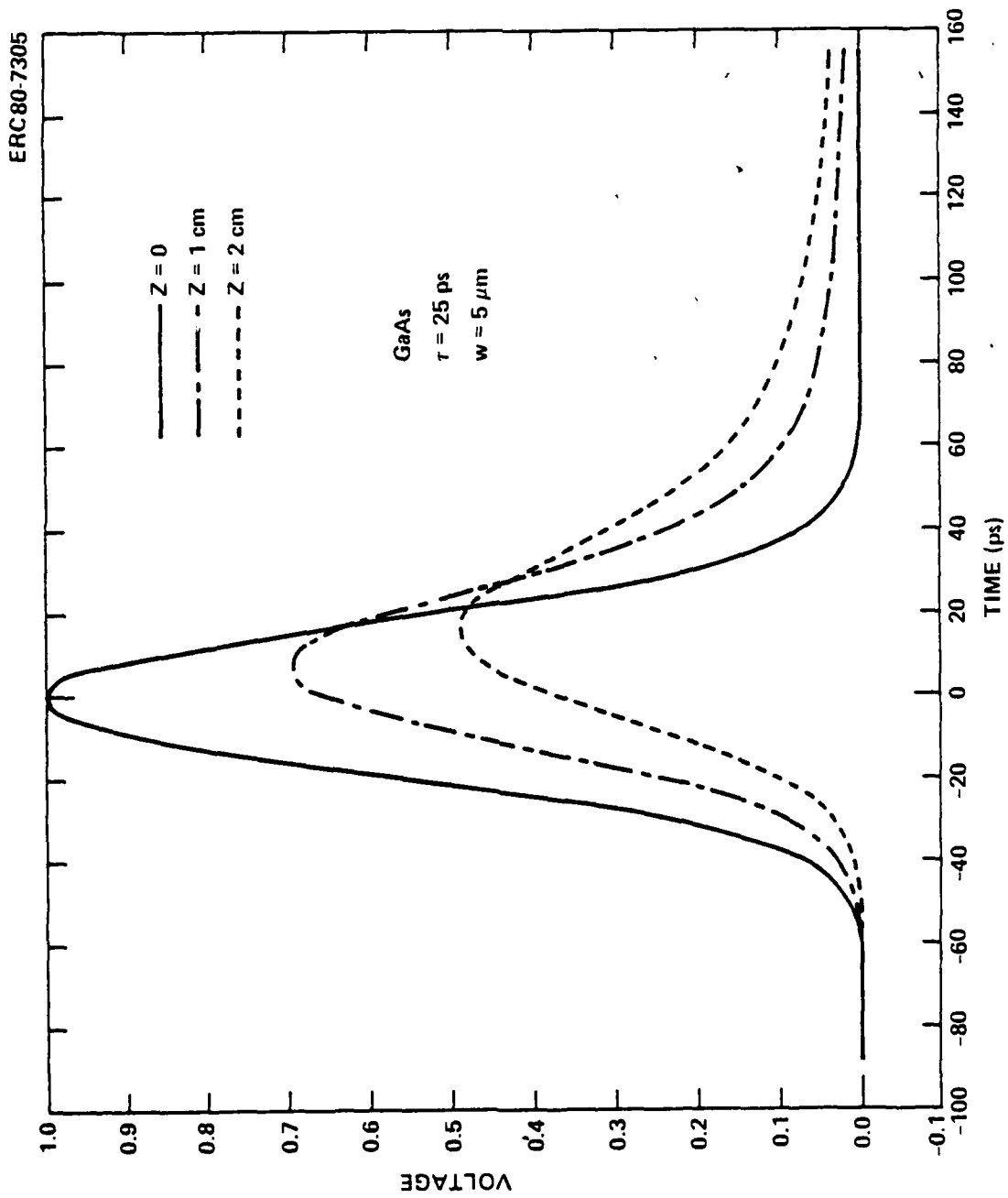


Fig. 3.17 Pulse evolution on a GaAs transmission line, with $\tau = 25 \text{ ps}$.

$$l(t) = t/v_{\text{opt}} \quad .$$

Plots of the temporal dependence of the induced phase change determined in this manner are given in Figs. 3.18 - 3.23, again using parameters appropriate to GaAs and LiNbO₃. These plots illustrate the effects of attenuation and distortion of the modulating pulse as well as the optical-microwave phase mismatch. The critical parameters phase shift amplitude and pulse width as determined from the plots of Figs. 3.18 - 3.22 and summarized in tabular form in Table 3.3. The amplitudes given in that table are those relative to those which would be obtained with perfect phase matching and no attenuation or distortion of the modulating pulse.

Another important parameter of the transmission line is its characteristic impedance, Z_0 , given by

$$Z_0 = (L/C)^{1/2} \quad ,$$

where L is the inductance per unit length and C is the capacitance per unit length. Again neglecting fringing effects, we can write

$$C \approx \frac{2\epsilon W}{d} \quad ,$$

for the structure of Fig. 3.12, so that

$$Z_0 \approx \sqrt{\frac{\mu_0}{\epsilon}} \frac{d}{2W} \quad .$$

If $d = W$, for example, then $Z_0 = 52\Omega$ in GaAs, 32Ω in LiNbO₃, and 29Ω in LiTaO₃.

It is possible to use the data in Table 3.3, together with the transmission line impedance values given above, to estimate the modulator power dissipation for the assumed materials parameters. The electrical power dissipation p_e is given by

$$p_e = \frac{B}{Z_0} \int_{-\infty}^{\infty} v^2(t) dt,$$



ERC41015.4FR

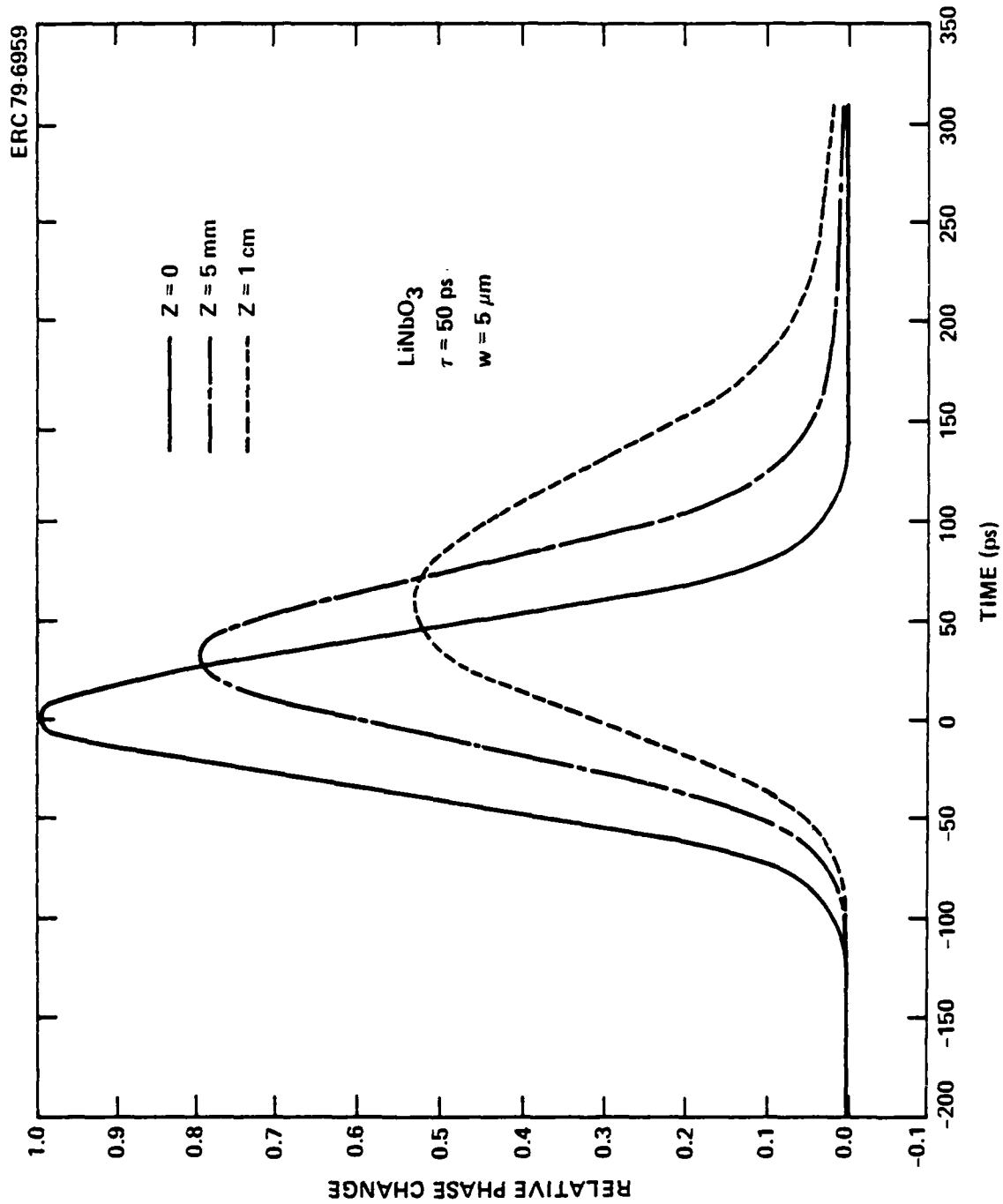


Fig. 3.18 Relative phase change for a LiNbO_3 traveling wave modulator, with $\tau = 50 \text{ ps}$.

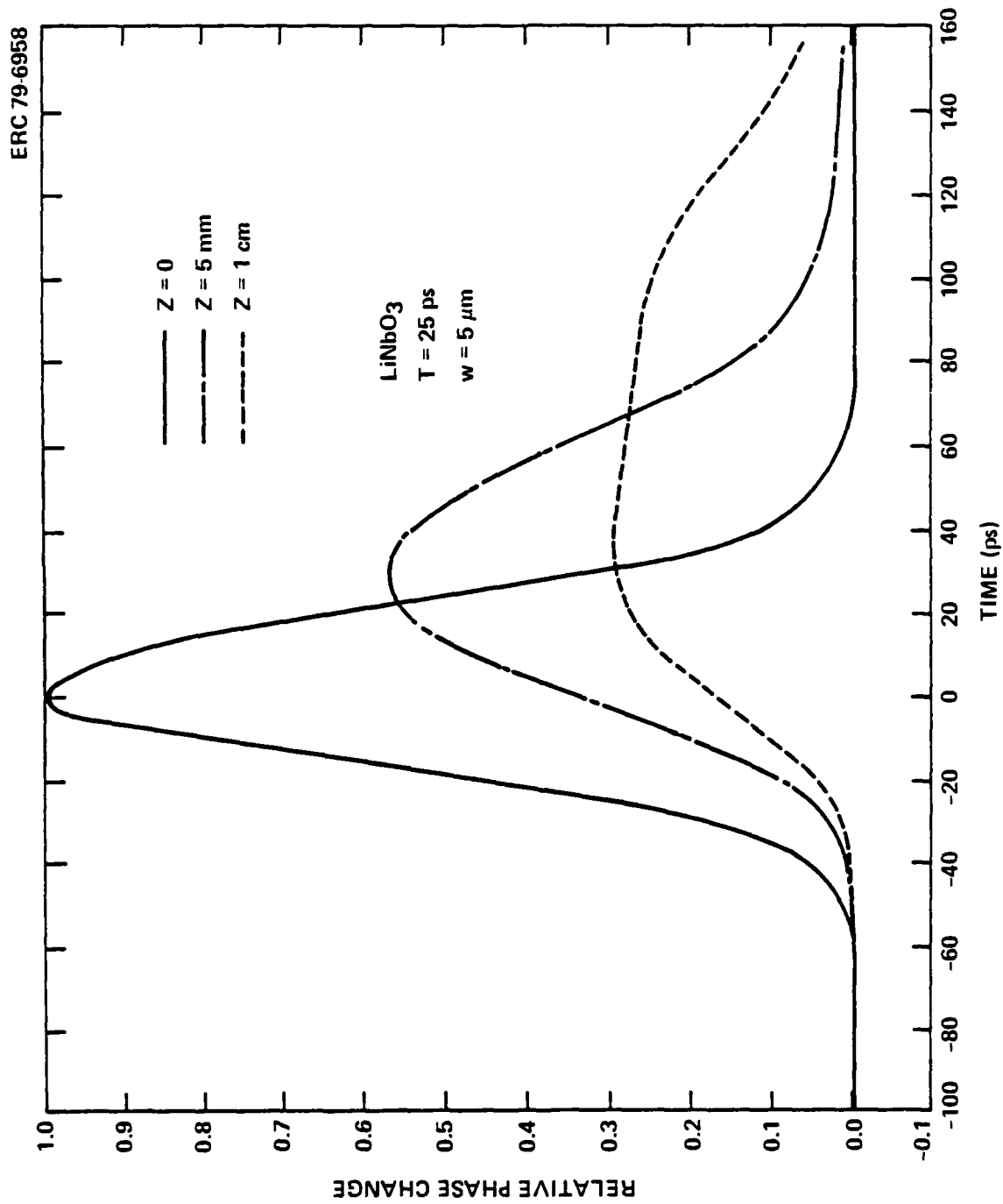


Fig. 3.19 Relative phase change for a LiNbO₃ traveling wave modulator, with $\tau = 25$ ps.



ERC41015.4FR

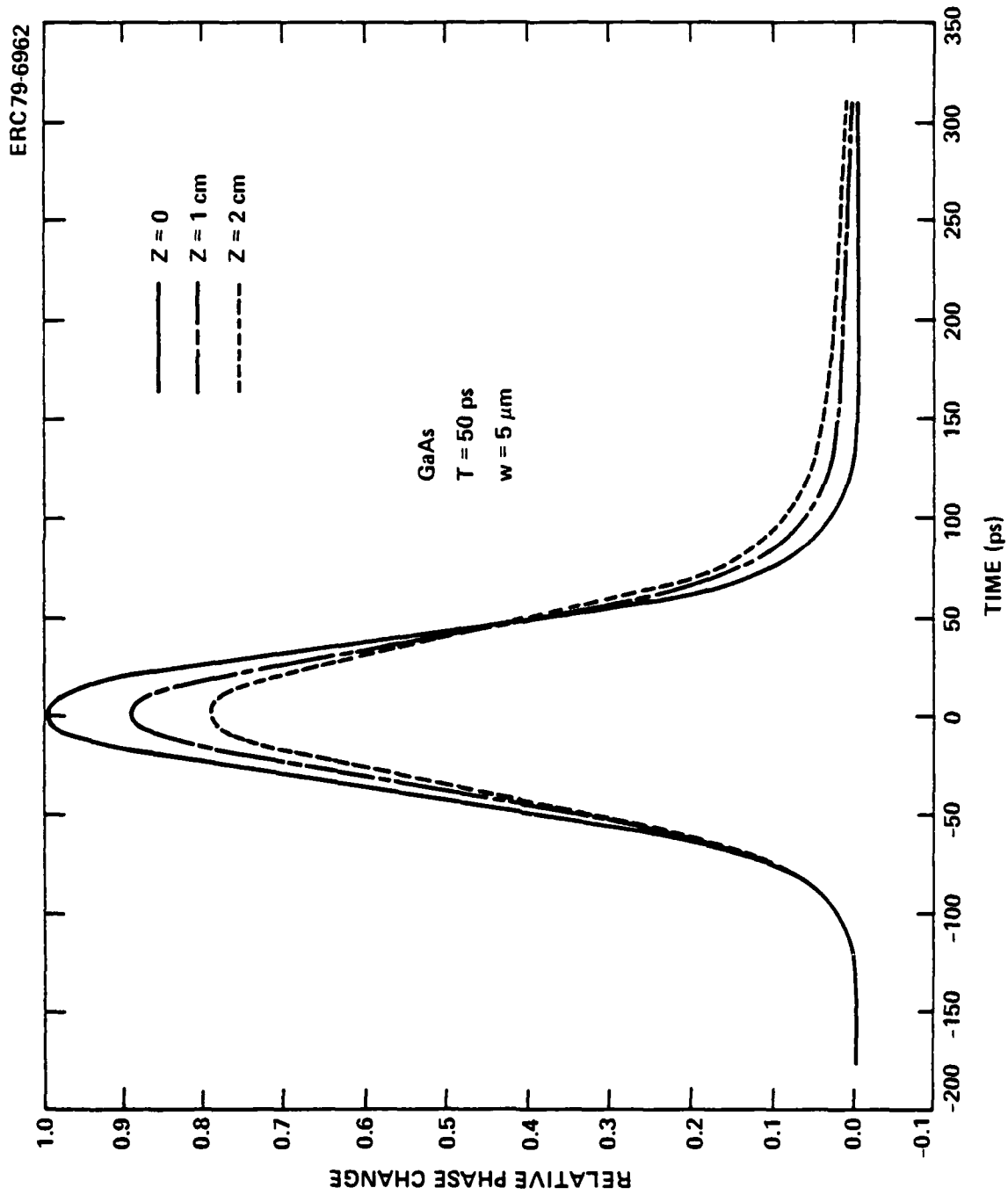


Fig. 3.20 Relative phase change for a GaAs traveling wave modulator, with $\tau = 50$ ps, $w = 5$ μ m.

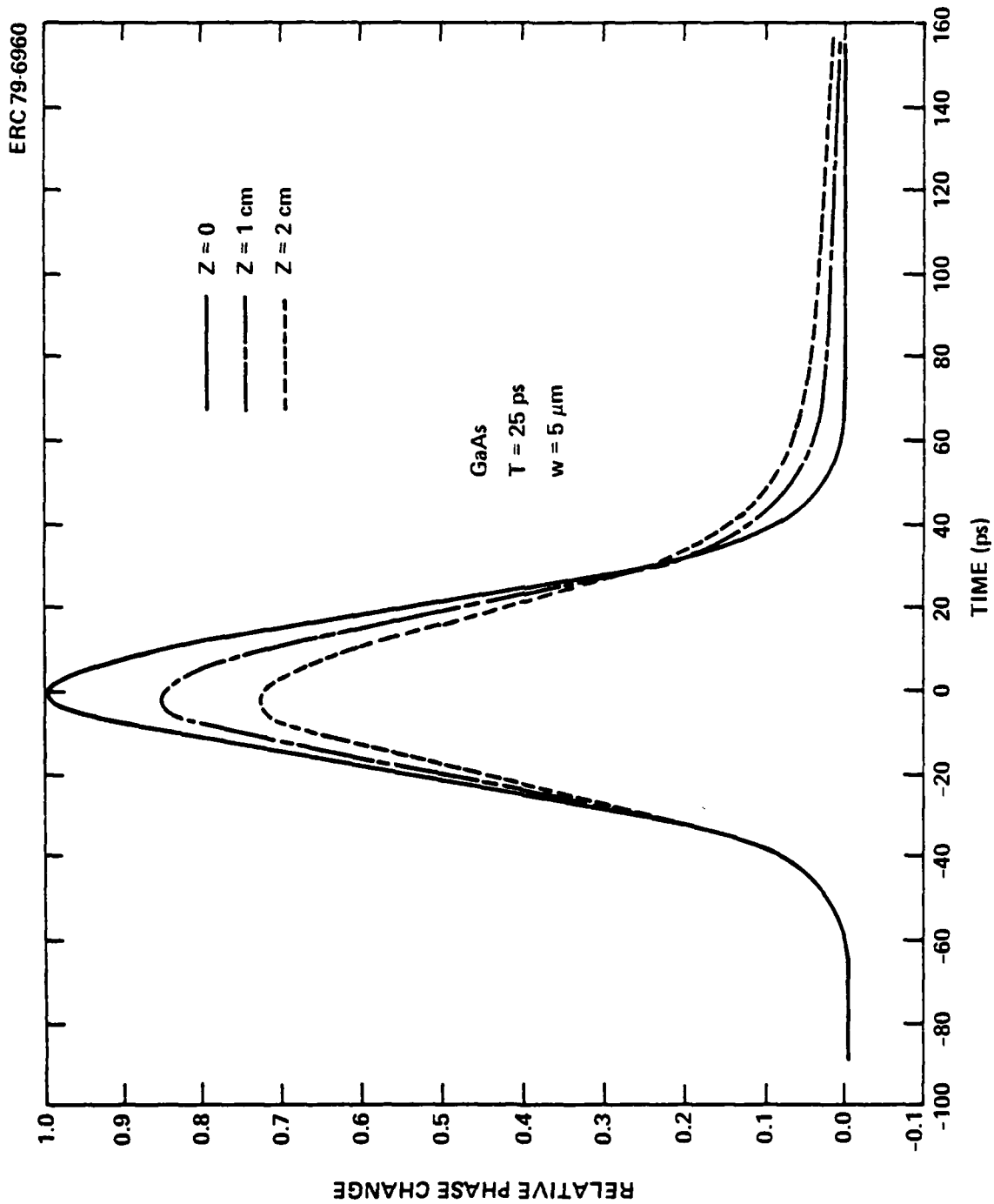


Fig. 3.21 Relative phase change for a GaAs traveling wave modulator, with $\tau = 25 \text{ ps}$, $w = 5 \text{ } \mu\text{m}$.



ERC41015.4FR

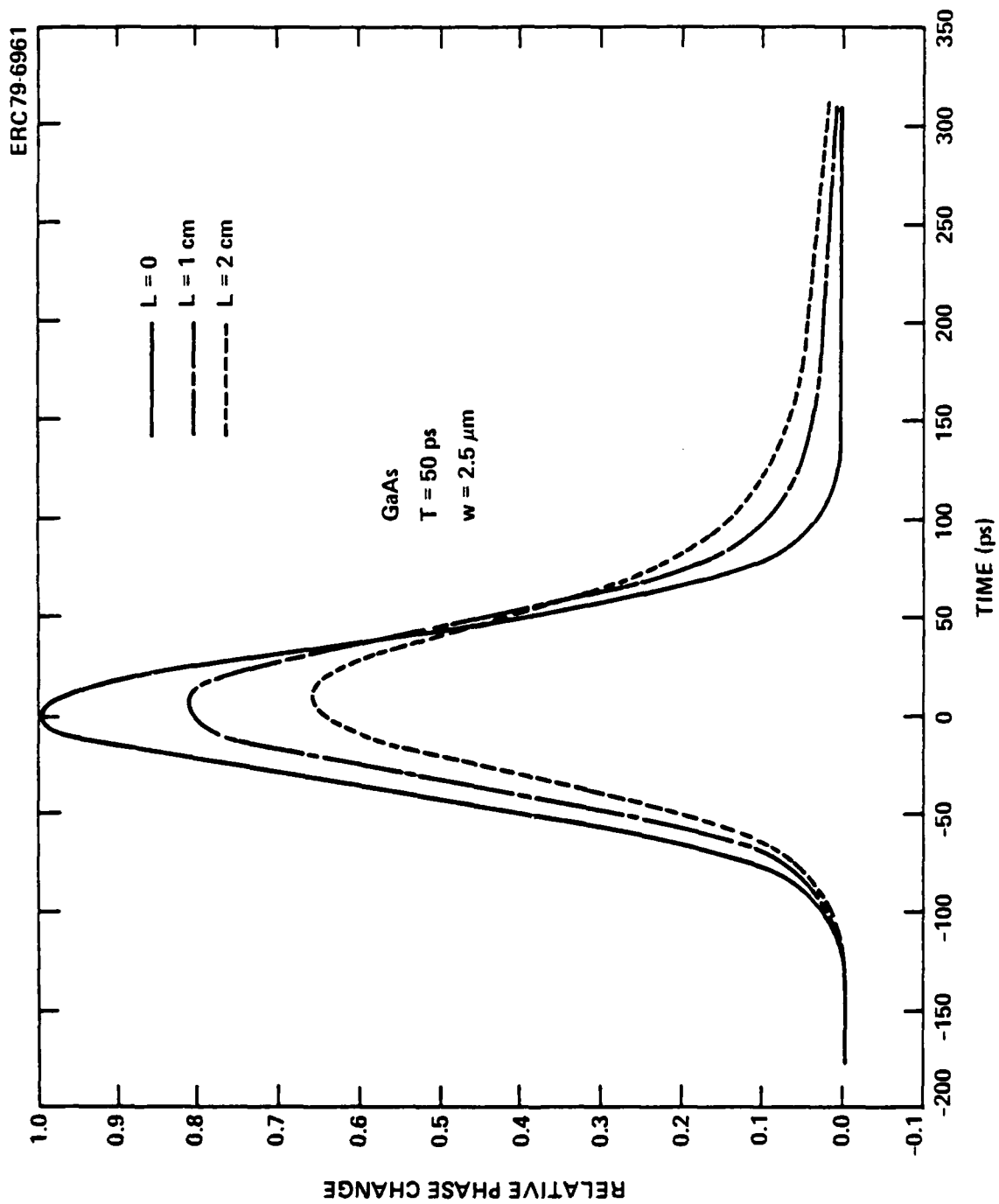


Fig. 3.22 Relative phase change for a GaAs traveling wave modulator, with $\tau = 50$ ps, $w = 2.5$ μ m.

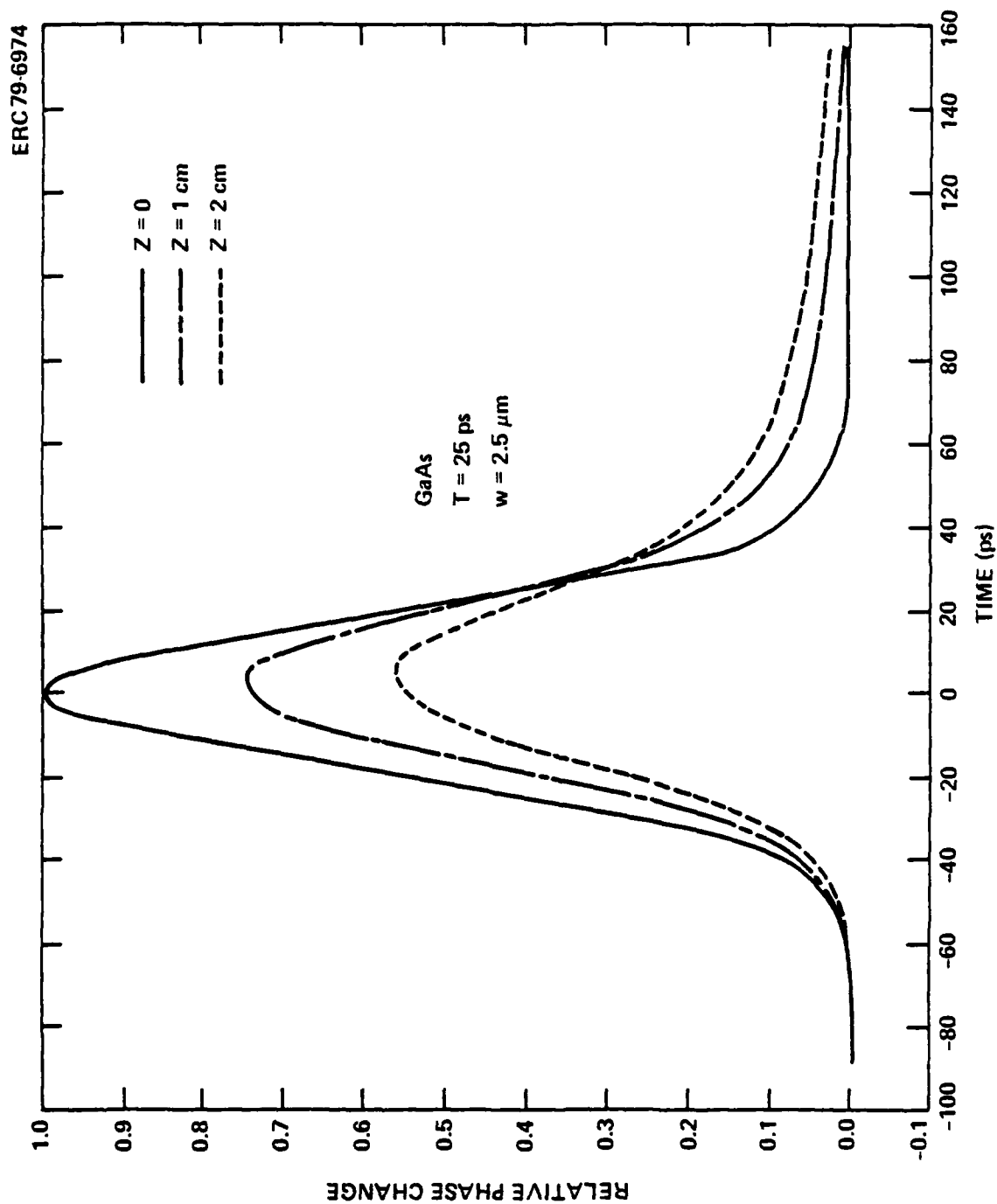


Fig. 3.23 Relative phase change for a GaAs traveling wave modulator, with $\tau = 25 \text{ ps}$, $w = 2.5 \text{ } \mu\text{m}$.



Table 3.3

Effect of Modulator Parameters on Amplitude and Width of
Relative-Phase-Shift Pulse

Material	T(ps)	W(μm)	Z(cm)	Relative Phase Shift Amplitude	Pulse Width (ps)*	
					10%	50%
LiNbO ₃	50	5	.5	.80	184	103
			1	.53	258	142
	25	5	.5	.56	178	73
			1	.28	>250	135
GaAs	50	5	1	.90	161	88
			2	.79	181	91
	25	5	1	.86	86	45
			2	.73	106	48
	50	2.5	1	.81	179	94
			2	.65	224	100
	25	2.5	1	.75	97	47
			2	.57	136	54

*The incident pulse width for T = 50 ps to 50% amplitude points is 88 ps, and to 10% amplitude is 155 ps. For T = 25 ps, the incident pulse width is 44 ps to 50% amplitude points, and 78 ps to 10% amplitude.

where B is the bit rate and

$$V(t) = V_p e^{-(t/T)^2},$$

with V_p the peak voltage. Evaluating the integral above yields the result

$$p_e = \sqrt{\frac{\pi}{2}} \frac{BTV_p^2}{Z_0} \quad (3.23)$$

It is assumed that V_p is the voltage required for complete extinction (π -radian phase shift) in the interferometric modulator. For LiNbO₃, the minimum value of V_p , given by

$$V_p = \frac{1}{2} \frac{d\lambda}{n_3^3 r_{33} L},$$

where r_{33} is the appropriate electrooptic coefficient, is obtained with both the applied field and the optical polarization vector parallel to the optic axis of the crystal. For GaAs, the minimum voltage is

$$V_p = \frac{\sqrt{3}}{4} \frac{d\lambda}{n^3 r_{41} L},$$

which occurs when the applied field and optical polarization vector are both parallel to a (111) crystal axis. Such a configuration in GaAs could not be achieved with the (100) substrate orientation commonly used for optical and electronic devices in GaAs, but could be obtained with a (110) substrate.

Values for the power dissipation calculated using (3.23) are tabulated in Table 3.4, assuming a bit rate B equal to the reciprocal of the 10% pulse width in Table 3.3. According to Table 3.4, a bit rate of 10.3 Gbit/s is expected in GaAs for $T = 25$ ps, $d = 2.5$ μm , and $Z = 1$ cm, with only 30 mW of electrical power dissipation. The apparently superior performance of GaAs vs LiNbO_3 in these examples results from the improved phase matching, higher impedance, and lower microwave attenuation of the former material, which more than compensates for the higher electrooptic coefficient in LiNbO_3 . It should be noted, however, that these calculations apply to the embedded electrode structure. The comparison would be more favorable to LiNbO_3 if coplanar electrodes were used.

Other factors which have a bearing on the choice of modulator materials are attenuation of the optical wave and compatibility with electronic driving circuitry. The optical attenuation is considerably higher in GaAs. The best optical attenuation figures reported in GaAs waveguides to date are about 6 dB/cm,³³ compared with less than 1 dB/cm in LiNbO_3 .³⁴ It is not clear, however, whether 6 dB/cm figure represents an intrinsic material limit or is due to impurity absorption. The answer to this question could have an important bearing on the ultimate performance of optoelectronic circuits and devices. The final factor is the potential for monolithic integration of the GaAs modulators and switches on the same substrate with the electronic components. In comparison with a hybrid approach based on the use of LiNbO_3 or LiTaO_3 for modulators and switches and GaAs for the other elements, monolithic integration apparently



ERC41015.4FR

Table 3.4

Electrical Power and Equivalent Data Rate for
Traveling Wave Modulator

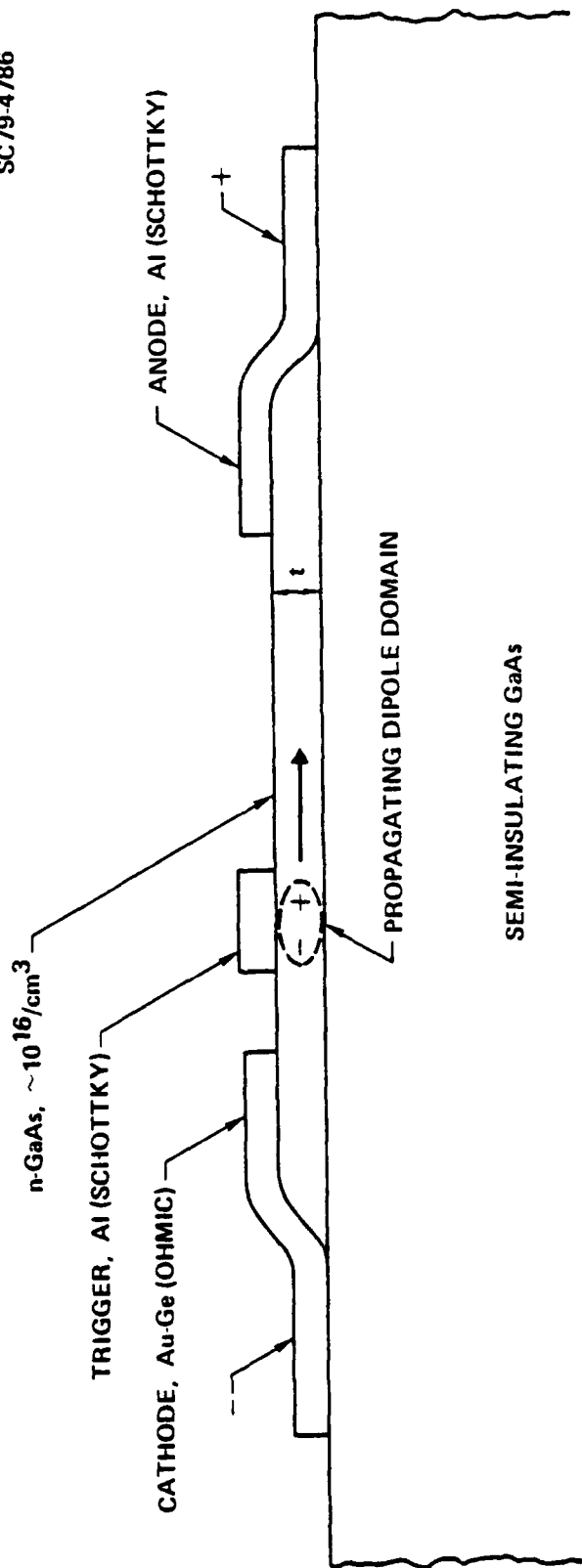
Material	T(ps)	d(μ m)	Z(cm)	Data Rate (Gbit/s)	Power (mW)
LiNbO ₃	50	5	.5	5.4	26
			1	3.9	11
	25	5	.5	5.6	27
			1	<4	-
GaAs	50	5	1	6.2	101
			2	5.3	28
	25	5	1	11.6	103
			2	9.4	29
	50	2.5	1	5.6	28
			2	4.5	11
	25	2.5	1	10.3	30
			2	7.4	9.3

offers the potential for lower cost and higher reliability, as well as higher performance resulting from the elimination of wire-bonded connections.

3.2.3 Electronic Drivers

The transferred electron logic device, or TELD, because of its high speed and essentially digital nature, is ideally suited for use in the electronic driver of the optical transmitter. A TELD is a three-terminal device, with an anode, a cathode, and a trigger electrode usually positioned near the cathode,³⁵ as illustrated in Fig. 3.24. The active region is an n-type epitaxial or ion-implanted layer fabricated on a semi-insulating GaAs substrate. Operation of the TELD is based on the negative differential mobility of gallium arsenide resulting from the transfer of conduction band electrons from states of low effective mass to states of higher effective mass under the influence of a high electric field. The low effective mass states which predominate at low fields are associated with the conduction band

SC79-4786



ERC41015.4FR

Fig. 3.24 Schematic diagram of a TELD.



ERC41015.4FR

energy minimum (Γ -point) at the center of the Brillouin zone, while the high effective mass states are associated with higher energy satellite minima (X -point) in the zone. Since the phenomenon depends upon the transfer of electrons from one conduction-band minimum to another, devices based on this effect are known as transferred electron devices (TEDs).

When a TED is biased above a certain threshold voltage V_t , dipole charge domains begin to form at the cathode and propagate to the anode, where current pulses appear. Only one propagating domain is present at any given time, and when one domain is extracted the next one forms at the cathode. The formation of a propagating domain results in a reduction in current through the device, while the current increases after a domain is extracted. As a result, the device acts as an oscillator, with fundamental frequency, f_0 , given by $f_0 = 1/\tau$, where τ is the transit time for a domain. In gallium arsenide, the propagation velocity for a domain is close to 1.0×10^7 cm/s, so $f_0 \approx 10^7/d$, where d is the anode-cathode separation.

A TELD is a TED with a Schottky barrier trigger electrode positioned between the anode and cathode. Under normal bias conditions, the electric field near the cathode is too small for domain formation. A negative voltage pulse applied to the trigger electrode causes an increase in depletion layer thickness in the region underneath the electrode, leading to an increase in the electric field near the cathode to a level above threshold for domain formation. The domain propagates from cathode to anode, and the current through the TELD is reduced for a period of time equal to the domain transit time. The response of the TELD to a negative trigger voltage pulse is therefore a negative current pulse of duration equal to the domain transit time.

The anode-to-cathode separation for the device is determined by the desired duration for the current pulses. For a transmitter designed for operation at a bit rate B , the current pulse duration τ_p should satisfy

$$\tau_p < 1/B \quad .$$

For example, if $B = 5$ Gbit/s, then $\tau_p < 250$ ps. To provide 25 ps margins for turn on and turn off of the TED, the maximum value of $\tau_p \sim 150$ ps. Since

$$d \sim 10^7 \tau_p \text{ (cm)} ,$$

with τ_p in seconds, then in this case $d = 15 \text{ } \mu\text{m}$. The threshold voltage can be calculated from

$$V_t = E_t d ,$$

where E_t is the threshold electric field. With $E_t = 3300 \text{ V/cm}$ in GaAs,³⁶ then $V_t = 5$ volts in the case considered.

The doping level and dimensions of the active region affect the formation and stability of dipole domains and determine amplitude of the current pulses as well as the average (dc) power dissipation. It has been determined from studies of planar TED oscillators that, to ensure full domain formation and propagation, the product of carrier concentration n and length d of the active region should satisfy the relation.³⁷

$$nd > 10^{13} \text{ cm}^{-2} \quad (3.24)$$

while the product of n and the thickness t of the active layer should satisfy³⁸

$$nt > 10^{12} \text{ cm}^{-2} \quad (3.25)$$

The influence of the dimension of the active layer on the series resistance R_S of the device is given by the relation

$$R_S = \frac{L}{e \mu n w t}$$

when e is the electronic charge ($= 1.6 \times 10^{-19} \text{ C}$), μ is the carrier mobility, t is the layer thickness, and w is the channel width. The dc current for bias



ERC41015.4FR

near the threshold is then given by

$$I_t = \frac{e \mu n t w V_t}{d} = e \mu n t w E_t \quad .$$

Substituting numerical values into this equation, $E_t \approx 3300$ V/cm for gallium arsenide and $\mu \sim 6700$ cm²/V-s (typical for high-quality epitaxial layers in gallium arsenide) gives

$$I_t = 3.5 \times 10^{-12} \text{ ntw} \quad .$$

Using the design values of

$$n = 2 \times 10^{16} / \text{cm}^3$$

$$t = 2 \times 10^{-4} \text{ cm}$$

$$w = 10^{-2} \text{ cm} \quad ,$$

it follows from the preceding equation that

$$I_t = 70 \text{ mA} \quad .$$

Assuming a 50% drop in current when a domain is produced, the change in current is

$$\Delta I_{\text{TELD}} = 0.5 I_t = 35 \text{ mA} \quad .$$

Note that in this example

$$n_d = 3 \times 10^{13} \text{ cm}^{-2}$$

$$n_t = 2 \times 10^{12} \text{ cm}^{-2} ,$$

so that the relations (3.24) and (3.25) are satisfied.

3.3 Receivers

The important characteristics of the optical receiver for the high-data-rate bus are speed of response and sensitivity. The speed of response determines whether the receiver limits the maximum data rate for the system, while the sensitivity determines the minimum required optical power at the receiver. The receiver contains a high-speed photodetector, amplifier stages, and a threshold circuit to regenerate the original train of pulses. Each of the receiver elements is discussed below.

3.3.1 Photodiode Design and Performance

Best performance in high-speed solid state optical receivers is obtained with the use of semiconductor photodiodes as the optical sensing elements. The diode is operated in the reverse-biased condition and is designed such that the optical absorption takes place primarily in the depletion region. The electron hole pairs generated as the light is absorbed are swept out of the depletion region by the dc bias field. In a simple pn or pin structure the maximum number of electronic charges collected is equal to the number of photons absorbed in the depletion region, while the internal speed of response is determined by the time required for electrons and holes to travel across the depletion region. In an avalanche photodiode (APD), on the other hand, a larger electric field in a portion of the depletion region makes it possible for the carriers to acquire enough kinetic energy to create additional carriers by collisions which promote electronic transitions from valence band to conduction band. The APD is then characterized by internal gain, in which the electronic charge collected exceeds the number of absorbed photons. This gain leads to improved signal-to-noise in a receiver, as it increases the signal level with respect to the thermal noise of the preamplifier or output circuit. However,

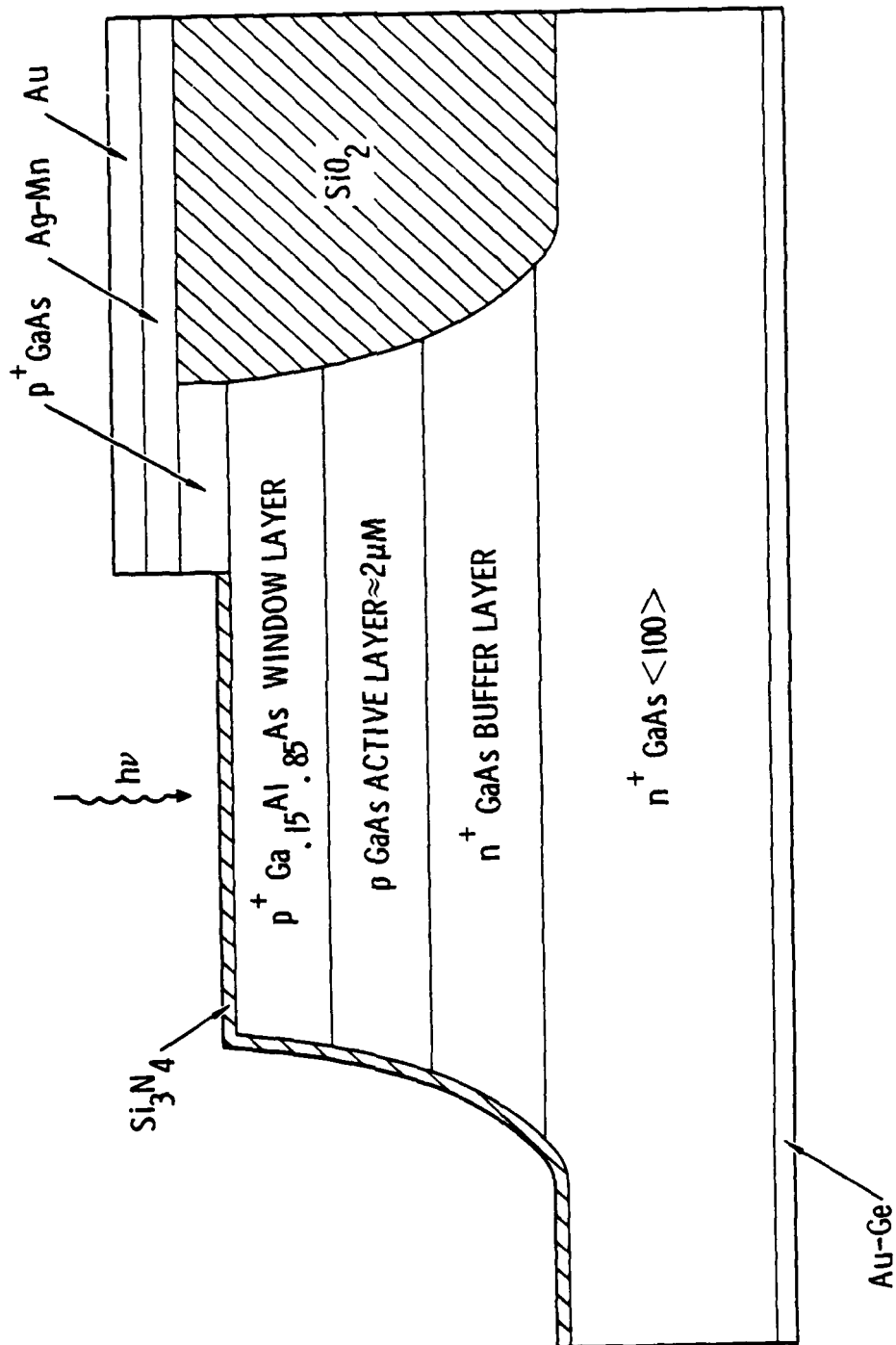


increasing the gain of an APD by increasing the bias voltage also has undesirable effects. The dark current and associated noise also increases sharply as the bias is increased. The speed of response is also reduced, as the multiple collisions lead to an increase in the effective transit time. There is thus an optimum APD gain which maximizes the receiver signal-to-noise ratio, consistent with the signal bandwidth or data rate.

In determining or predicting the response of a photodiode or avalanche photodiode, the kinetics of the carrier multiplication process must be taken into account. This is possible if the dependence of the ionization coefficient for both electrons and holes on the electric field is known. In order to predict the temporal response of an APD, a computer program has been written which calculates the evolution of carriers in response to an initiating light pulse, using the empirical data of Law and Lee³⁹ to determine the field dependence of electron and hole ionization coefficients. Using this model, calculations have been made of the temporal response of some APD structures to an optical pulse of infinitesimal duration, as a function of the gain of the device. For the conventional GaAs/GaAlAs structure of Fig. 3.25, with light incident through the surface of the semiconductor, the predicted temporal response is plotted in Fig. 3.26 for several values of the avalanche gain M . For guided wave applications, a different structure will be needed in which the light is incident in an optical wave guide. Such a structure is illustrated in Fig. 3.27, and the predicted response is plotted in Fig. 3.28. The pulse width at 10% amplitude points as determined from the plots of Fig. 3.28 is tabulated in Table 3.5. A corresponding bit rate B , defined as the inverse of the pulse width, is also given in that Table.

GaAs AVALANCHE PHOTODIODE WITH GaAlAs WINDOW

SC79-3466



ERC41015.4FR

Fig. 3.25 Schematic of a GaAs avalanche photodiode with a GaAlAs window.



ERC41015.4FR

IMPULSE RESPONSE OF GaAs AVALANCHE PHOTODIODE

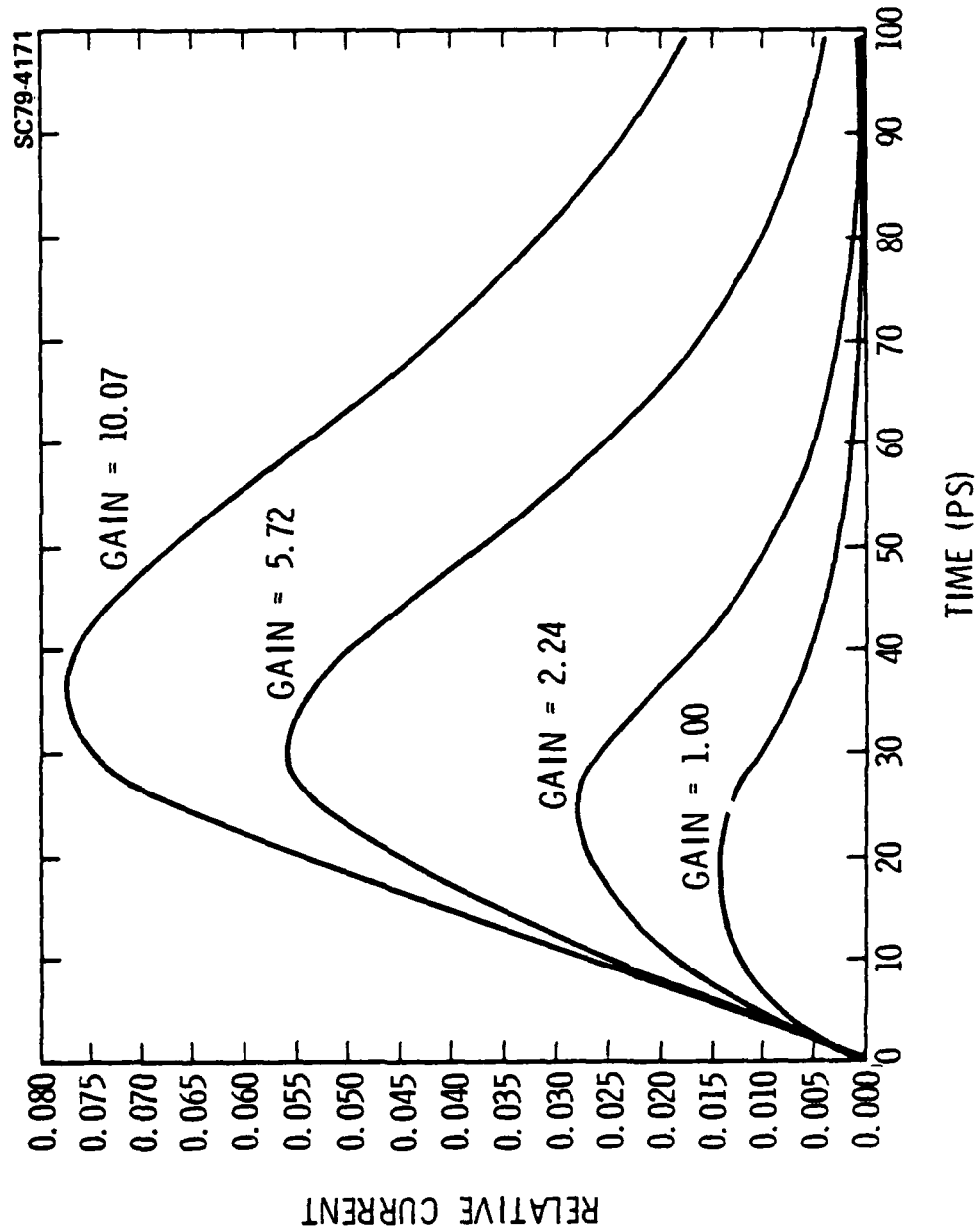


Fig. 3.26 Calculated temporal response of GaAs APD to an optical impulse for different values of gain.

ERC41015.4FR

ERC80-7303

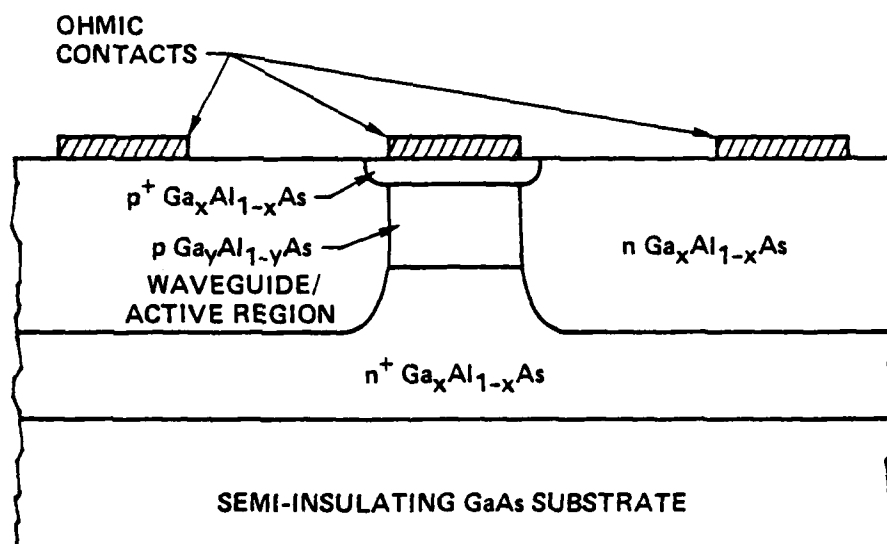


Fig. 3.27 Hypothetical structure for optical waveguide APD.



ERC41015.4FR

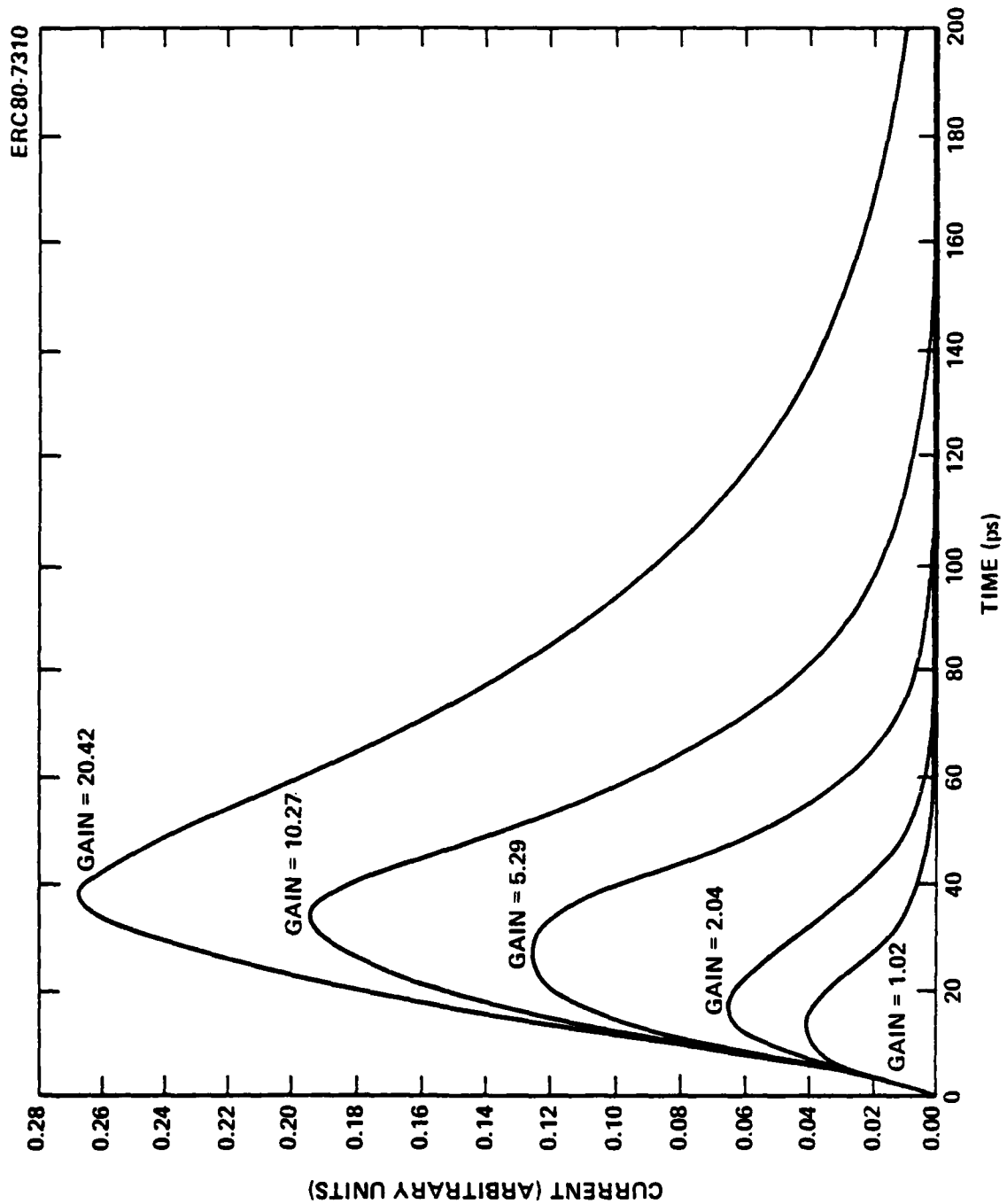


Fig. 3.28 Calculated temporal response of the APD structure of Fig. 3.27 to an optical impulse for several values of gain.

Table 3.5

APD Response Characteristics

Gain	Pulse Width, ps (10% Amplitude)	Data Rate (Gbit/s)
1.02	42	23.8
2.04	50	20
5.29	70	14.3
10.27	95	10.5
20.42	150	6.7

3.3.2 Receiver Signal-to-Noise Ratio

A practical receiver should be designed to maximize the signal-to-noise ratio, S/N. For a bit-rate B, the ratio of the signal power to noise power in the receiver circuit is⁴⁰

$$\frac{S}{N} = \frac{(nePM/h\nu)^2}{(ne^2P/h\nu + eI_D) M^{2+X_n} B + (4kT\alpha/R)B} \quad (3.26)$$

where

- η is the quantum efficiency
- e is the electronic charge
- M is the gain
- $h\nu$ is the photon energy in electron volts
- P is the average optical power
- I_D is the dark current (in amps)
- X_n is the avalanche noise factor
- k is Boltzmann's constant
- T is the absolute temperature, and
- R is the photodetector output impedance
- α is the amplifier noise figure.



The signal-to-noise ratio is an increasing function of the impedance R . However, increasing R decreases the response speed of the photodiode as determined by the RC time constant, where C is the capacitance of the photodetector and amplifier input. For a practical digital receiver,

$$RC \leq (2\pi B)^{-1},$$

which implies a charge decay by a factor of 535 during one bit interval. Assuming that $R = (2\pi BC)^{-1}$ makes it possible to rewrite (1) as

$$\frac{S}{N} = \frac{(nePM/h\nu)^2}{(ne^2P/h\nu + eI_D) M^{2+\alpha} B + 8\pi kT\alpha CB^2} \quad (3.27)$$

Thus, for high bit rates and constant optical power, the signal-to-noise ratio falls as B^{-2} .

The calculated dependence of error rate for digital transmission on signal-to-noise ratio, assuming white Gaussian noise, is given by Fig. 3.29. For an error rate of 10^{-10} , for example, the required signal-to-noise ratio is 22 dB. For a given allowable error rate and an assumed set of receiver parameters, it is possible to determine the required optical power level at the receiver. This is accomplished by expressing (3.26) as a quadratic equation in the optical power P , and solving for P . In these calculations, it is assumed that the receiver noise figure is given by $\alpha = 1 + 8 \times 10^{-11} B$; i.e., that it increases from 0.3 dB at 1 Gbit/s to 2.6 dB at 10 Gbit/s. Minimum optical power is plotted as a function of bit rate for several values of APD gain in Fig. 3.30. Note that best performance is obtained for a gain of about 10 over the entire range of bit rates considered, from 100 Mbit/s to 10 Gbit/s. In Fig. 3.31, the minimum optical power is plotted as a function of gain at a data rate of 5 Gbit/s. The minimum optical power at this data rate is found to be -28 dBm.

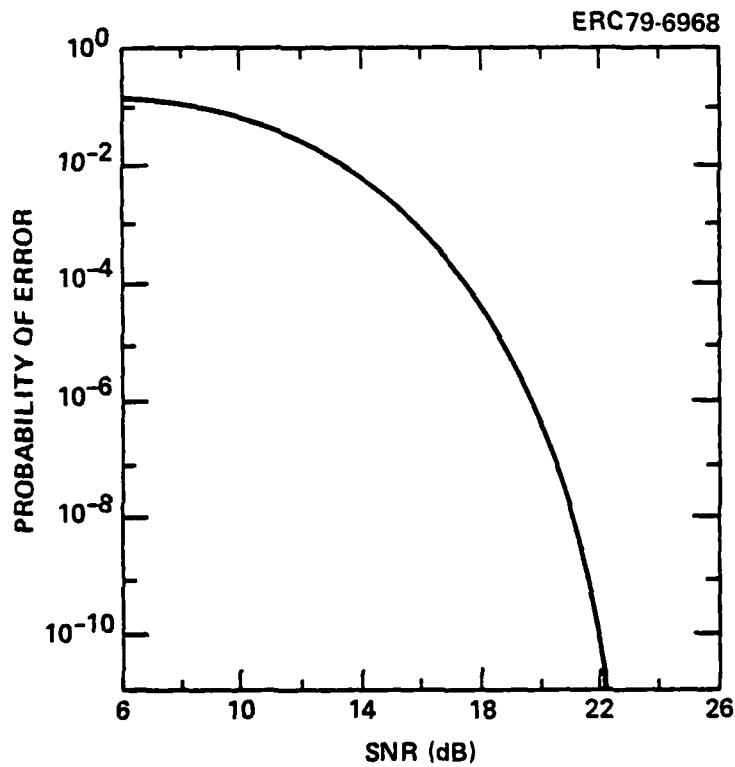


Fig. 3.29 Calculated dependence of probability of error on signal-to-noise ratio for pulse-code-modulated transmission, assuming white Gaussian noise.

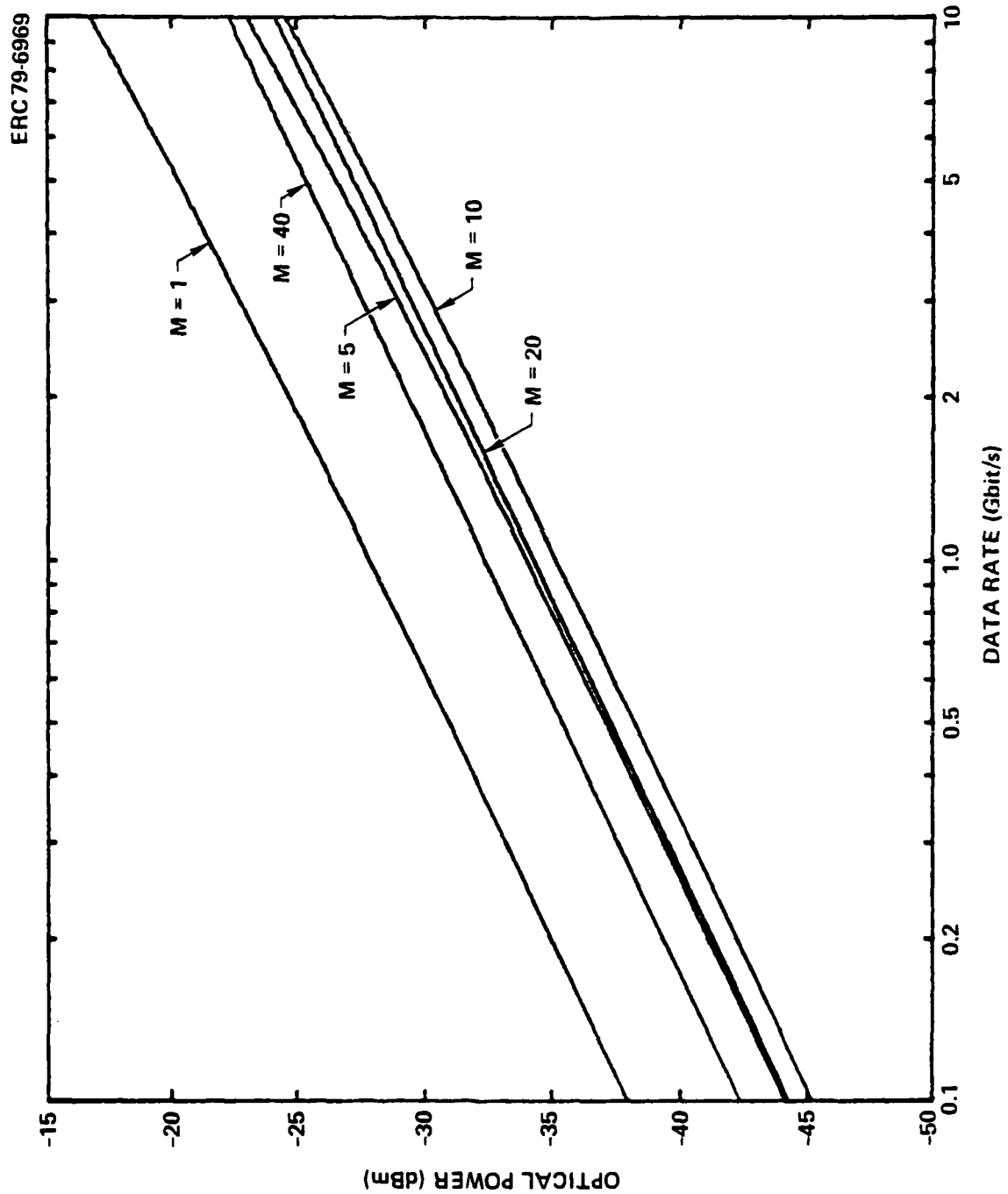


Fig. 3.30 Calculated dependence of minimum optical power required to achieve an error rate of 10^{-10} on data rate, for different values of APD gain.

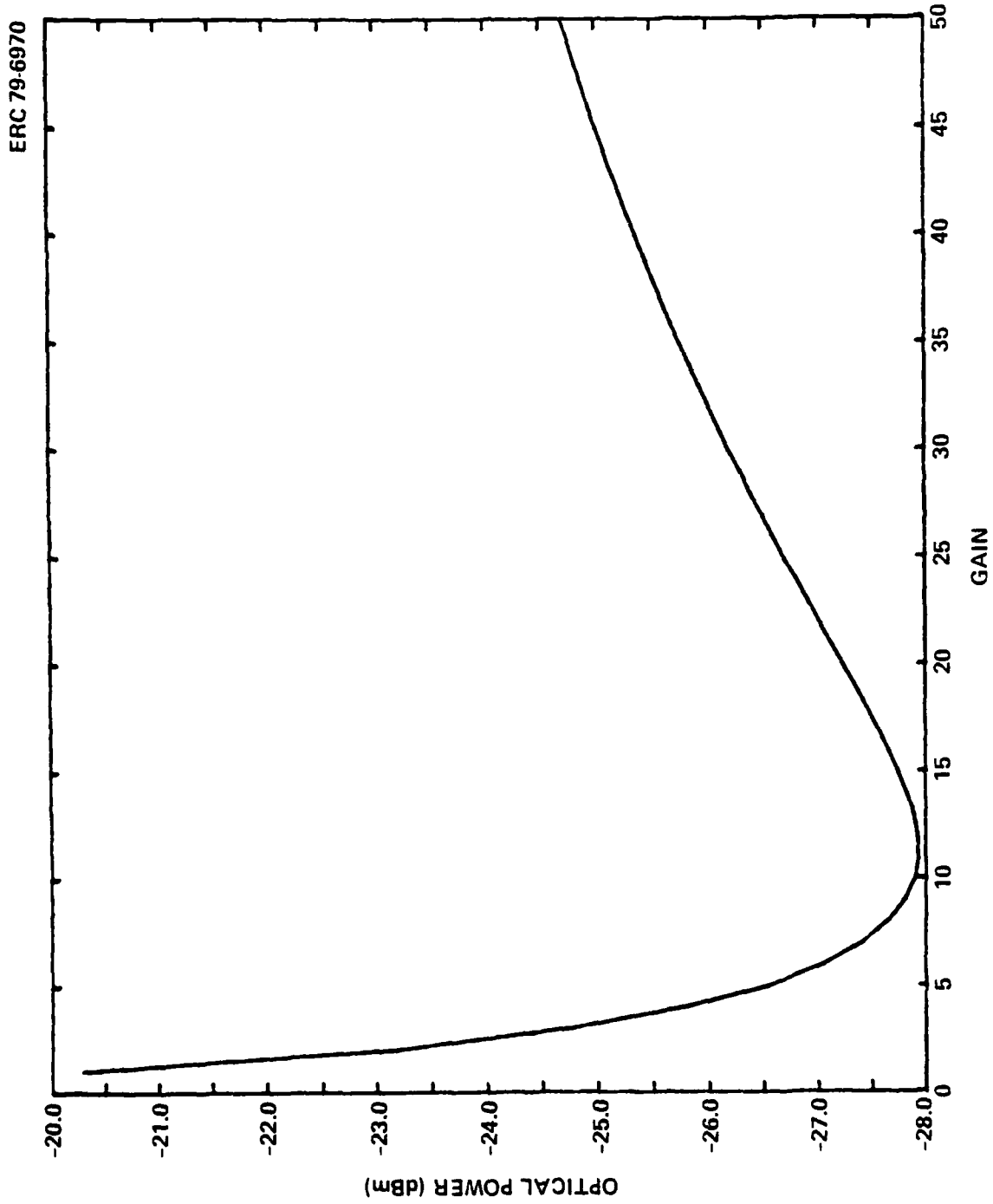


Fig. 3.31 Dependence of minimum optical power required to achieve an error rate of 10^{-10} at a data rate of 5 Gbit/s on APD gain.



3.3.3 Amplifier Design Considerations

In the high-speed repeater, it is necessary to amplify the electrical signal from the photodiode to a power level sufficient to activate the TELD driver for the laser. This is accomplished by means of a multistage FET amplifier integrated on the same substrate with the photodiodes. The FET is also a three-terminal device, but unlike the TED it has a dependence of output current on input voltage which is approximately linear over a fairly wide operating range.⁴¹ The three terminals are designated source, gate, and drain, as indicated in Fig. 3.32. In gallium arsenide, the electrodes are fabricated on a thin n-type layer, with ohmic contacts for source and drain and a Schottky barrier for the gate. When a bias voltage is applied between source and drain, a current flows through the n-type layer. The source-to-gate bias controls the source-to-drain current by regulating the thickness of the depletion layer under the Schottky gate electrode. No current flows in the depletion layer so that increasing the negative gate bias decreases the drain current. The current is completely shut off for a negative gate voltage large enough to completely deplete the layer under the gate. This voltage is known as the "pinch off" voltage, V_{po} . For zero applied gate voltage, the region under the gate is partially depleted due to the Schottky barrier potential. The "built in" potential responsible for the depletion, V_{bi} , equals -0.8 V in GaAs.

An important factor in the amplifier design is the gain which it is required to deliver. Assuming an optical signal level of -27 dBm and a gain of 23 (which gives an error rate of 10^{-10} , according to Fig. 3.31), the current from the photodetector at a wavelength of .8 μm and quantum efficiency of .9 is 27 μA . For a capacitance of .05 pf, an input impedance of 600 Ω gives an RC time constant of 30 ps for the preamplifier. Thus, the voltage input to the amplifier is 16 mV, and the power input is -34 dBm. Assuming that a power of 25 mW, or 14 dBm, is needed to drive the laser, and that the TELD provides 10 dB of gain, then the amplifier must provide an additional gain of 38 dB.

The amplifier response speed is a critical factor in determining the maximum receiver data rate. The cutoff frequency for current gain for an FET is approximated by the simple relation

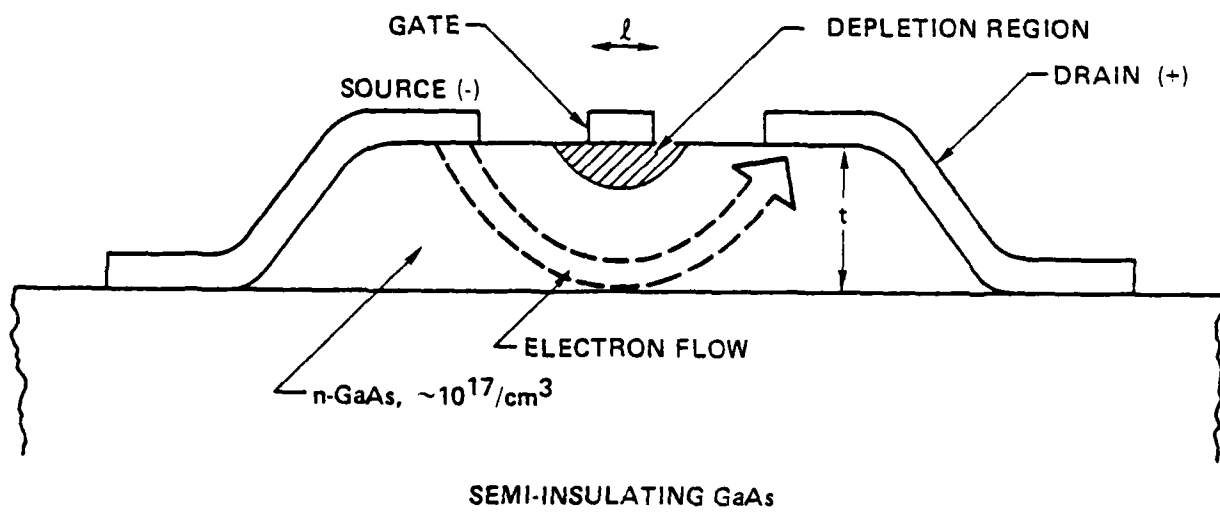


Fig. 3.32 Schematic diagram for GaAs FET.



$$f_T \approx \frac{1}{2\pi} \frac{v_{sat}}{L} ,$$

where v_{sat} is the saturation velocity for electrons in the material ($v_{sat} = 8 \times 10^6$ cm/s in GaAs) and L is the gate length. Thus, $f_T = 12$ GHz, 24 GHz, and 48 GHz for $L = 1 \mu\text{m}$, $0.5 \mu\text{m}$, and $0.25 \mu\text{m}$, respectively. For a 5 Gbit/s receiver designed such that the 3 dB cutoff frequency f_{co} is 10 GHz, the useful gain f_T/f_{co} is 1.2 (1.6 dB), 2.4 (7.6 dB), and 4.8 (13.6 dB) for $1 \mu\text{m}$, $0.5 \mu\text{m}$, and $0.25 \mu\text{m}$ gate widths. Thus, it appears that a practical amplifier designed to give 38 dB gain at 5 Gbit/s would require FET gate widths of the order of $0.25 \mu\text{m}$, in which case the required gain could be achieved in a 3-stage amplifier.

3.4 Electrooptic Switch

Optical switches are needed in the high-speed bus for controlling the flow of data between the input-output buffer loops and the main bus terminal and between the buffer loops and the processor terminals. Switches based on the electrooptic effect have the potential for the high-speed operation required for the buffer loop-to-processor interfaces. Two configurations for 2×2 electrooptic switches are illustrated schematically in Figs. 3.33 and 3.34. In both those types of switch, the electrooptic interaction affects the efficiency for power coupling between two parallel optical waveguides. The coupling region and electrooptic interaction region can be common, as in Fig. 3.33, or separate, as in Fig. 3.34. The power transfer characteristics for these two switch configurations are different, as illustrated in Figs. 3.35 and 3.36.

Of the two configurations, the one in which the electrooptic interaction region and the coupling region are separate (Fig. 3.34) is judged to be preferable for the high-speed bus. If surface electrodes are used, the center electrode must be only a few μm wide for the common coupling interaction region alternative of Fig. 3.33, leading to a substantial increase in attenuation of the modulating signal due to the relatively high resistance of the narrow electrode. Furthermore, separating the coupling and interaction regions makes it possible to use a buried electrode structure, as illustrated previously in

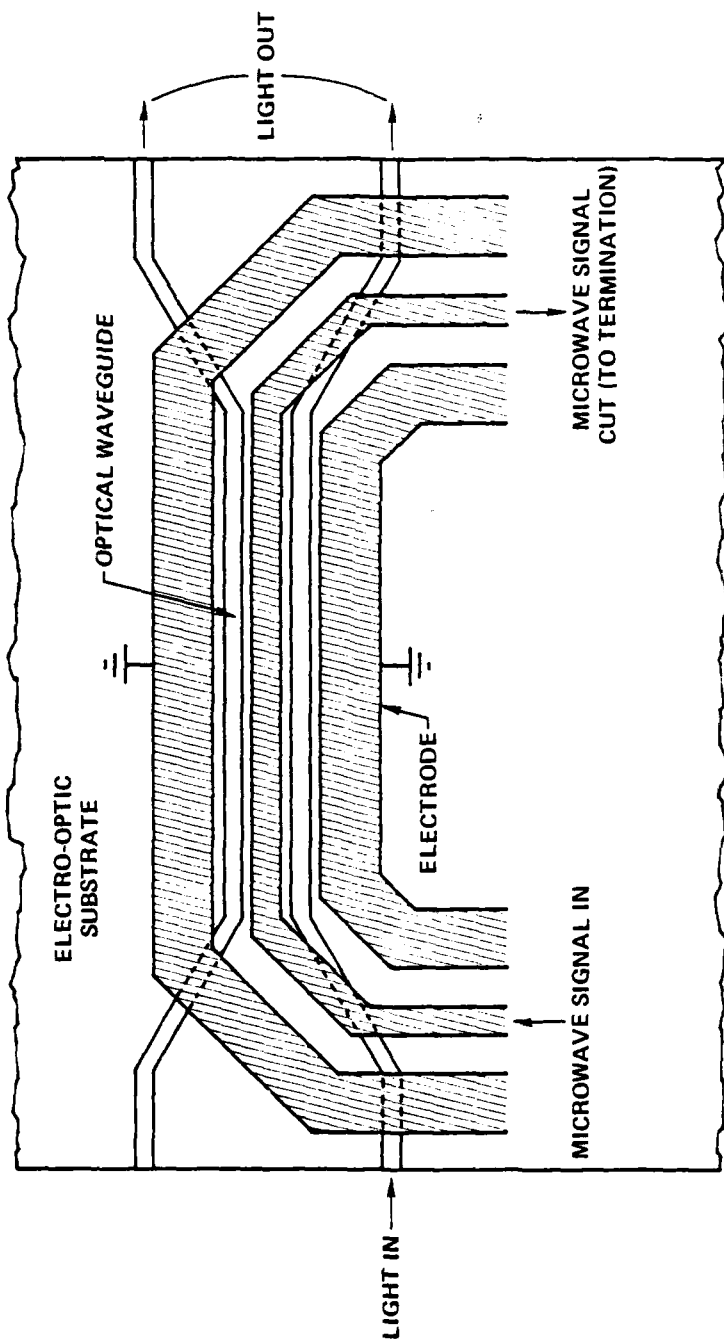


Fig. 3.33 Traveling wave configuration for a 2 x 2 optical switch, with common coupling and electrooptic interaction regions.



TRAVELING WAVE ELECTRO-OPTIC MODULATOR

ERC80-7309

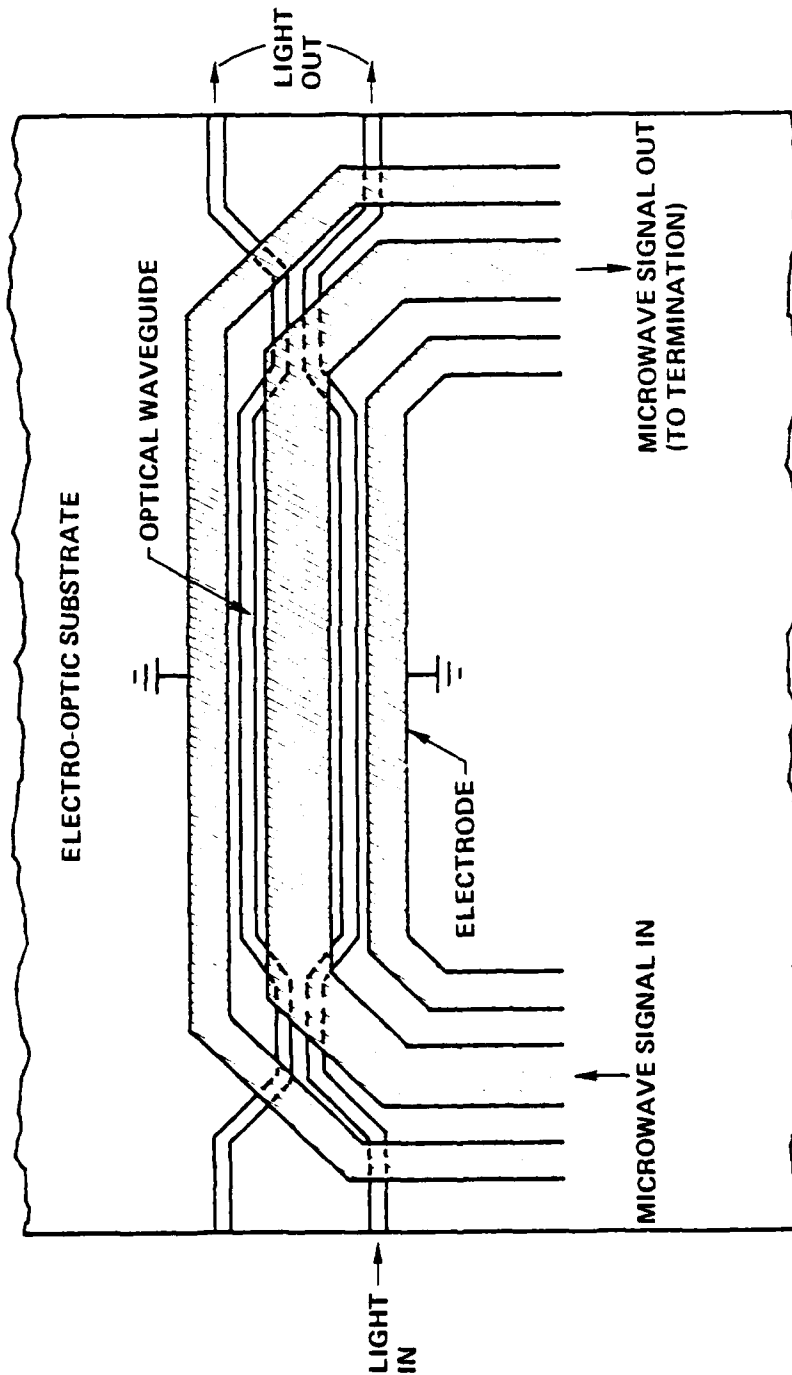


Fig. 3.34 Traveling wave 2 x 2 optical switch, with separate coupling and interaction regions.

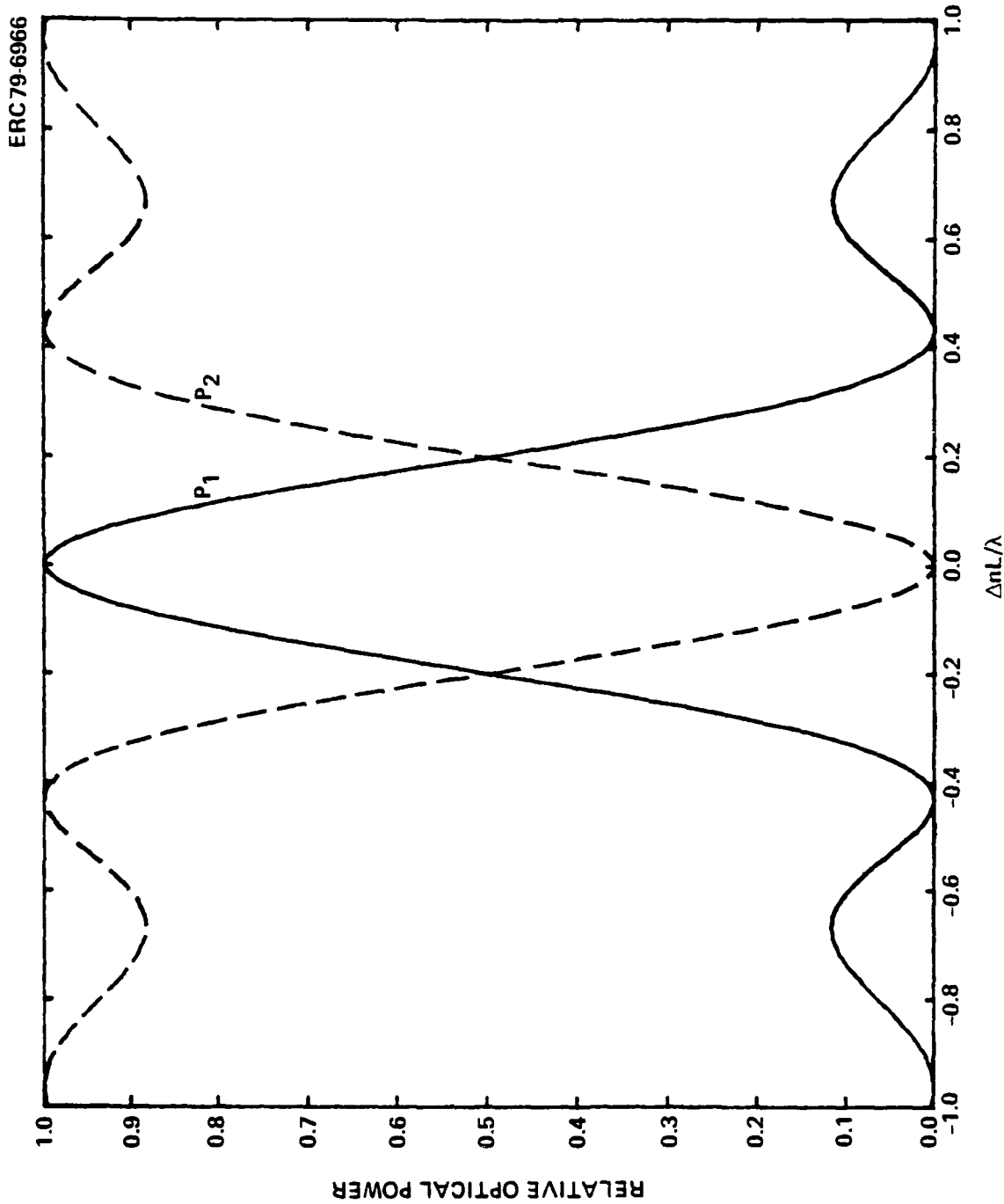


Fig. 3.35 Relative output power for the two output ports of the switch illustrated in Fig. 3.33, plotted as a function of the normalized induced refractive index change. It is assumed that only one input waveguide is excited. Perfect phase matching and no attenuation of the modulating signal are assumed in the calculations.



ERC41015.4FR

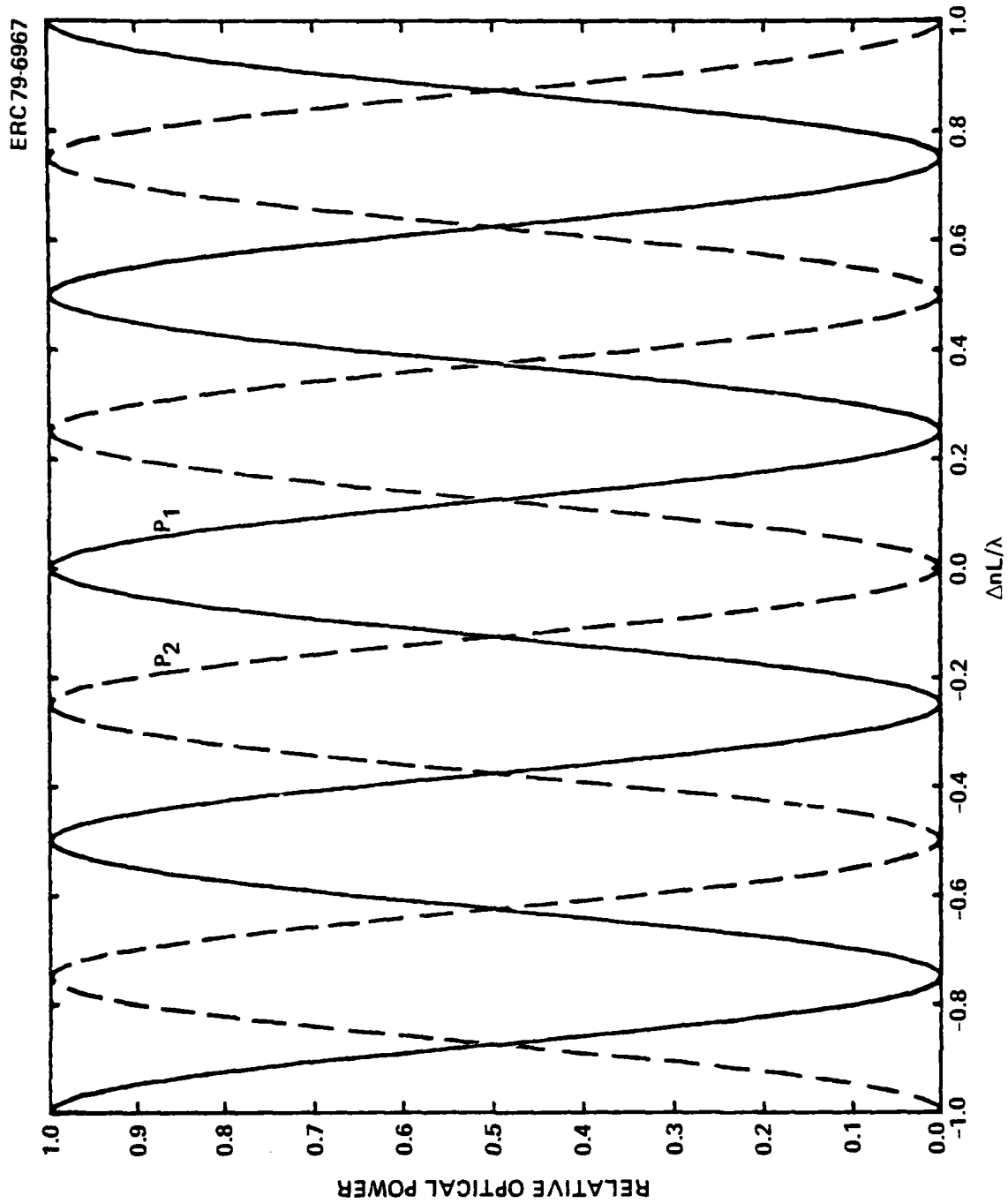


Fig. 3.36 Relative power output for the two output ports of the switch of Fig. 3.34, plotted as a function of the normalized induced refractive index change.

Fig. 3.13. A larger refractive index change is obtained for a given modulating power level with buried electrodes than with surface electrodes, which make use of fringing fields to produce the electrooptic modulation.

Analysis of the 2 x 2 switch is almost identical to that of the traveling wave modulator described in Section 3.3.2. However, the function of the switch in the system is different from that of the modulator -- the modulator is used to generate short pulses, while the switch performs the function of removing single pulses from the storage loop or inserting single pulses into the loop. As such, the switch must provide a "time window" with turn-on and turn-off of extremely short duration and total duration less than a bit interval. Assuming that the switch is initially in the "cross-over" state, the temporal dependence of the power transmitted in the straight-through state P_s in response to a Gaussian modulating pulse is given by

$$P_s = P_0 \sin^2[(\Delta\phi_0/2) \exp(-t/T)^2] ,$$

where P_0 is the total optical output power in both ports of the switch and $\Delta\phi_0$ is the phase shift in the modulator arms at the peak amplitude of the pulse. The preceding equation assumes perfect phase matching between the optical and microwave signals. The transmission characteristics of the optical switch can have much sharper rise and fall times than those of the modulating electrical pulse, as illustrated in Figs. 3.37 - 3.39.

3.5 Frequency-Selective Couplers

Frequency multiplexing (sometimes referred to as "color multiplexing" or "wavelength multiplexing") offers the possibility of greatly increasing the information capacity of an optical fiber transmission line. Even in systems where bandwidth is not a limiting factor, the use of frequency multiplexing can eliminate the need for expensive and complex electronic multiplexing equipment. In a frequency multiplexed system, each information channel is assigned a range of frequencies, or frequency band, for transmission. An important element of



ERC41015.4FR

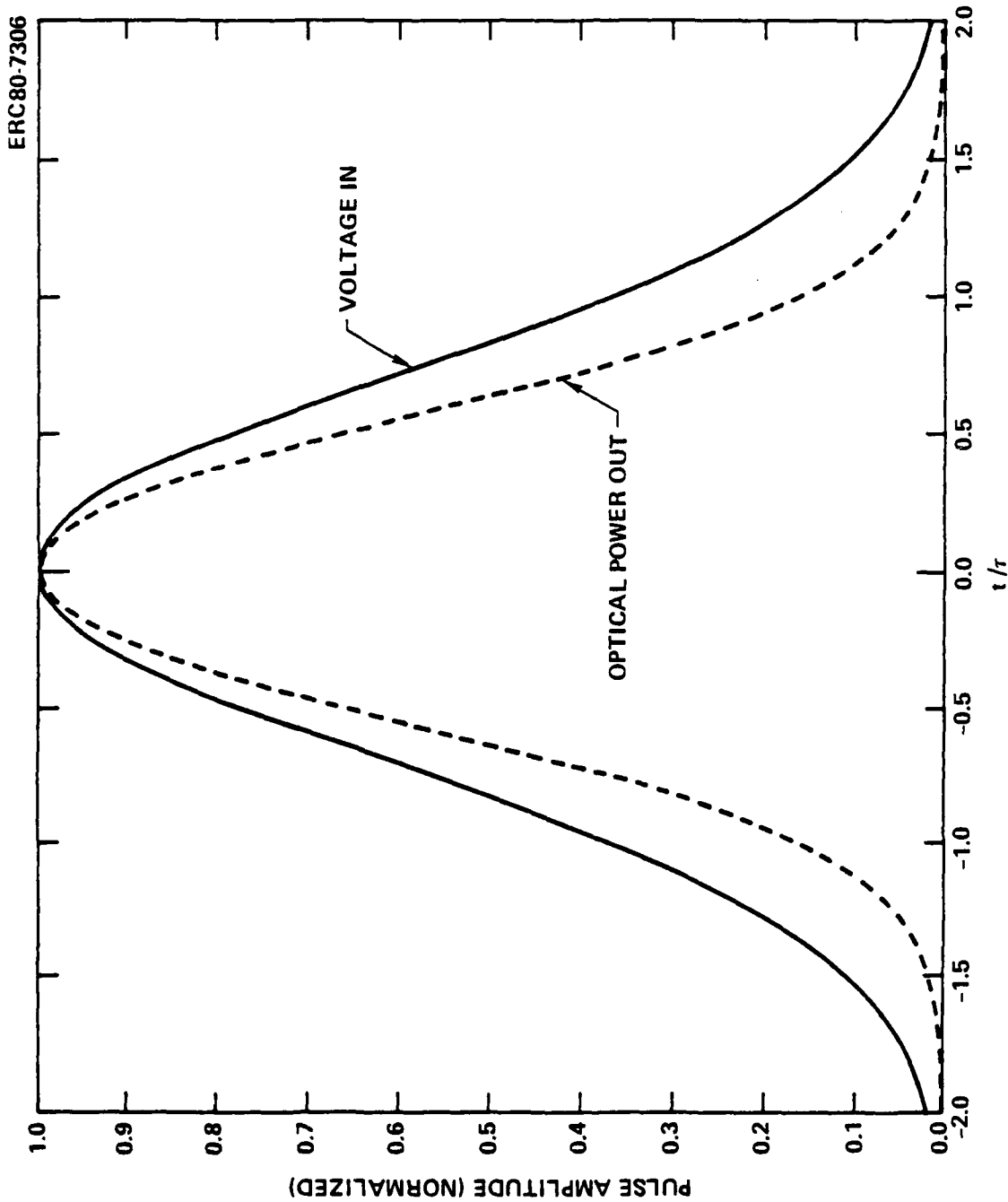


Fig. 3.37 Temporal response of switch transmission to a Gaussian voltage pulse, assuming perfect phase matching of microwave and optical signals and no attenuation of the modulating wave. It is assumed that the peak voltage produces a $\pi/2$ radian phase shift between the interferometer arms. The optical power is normalized to unity maximums.

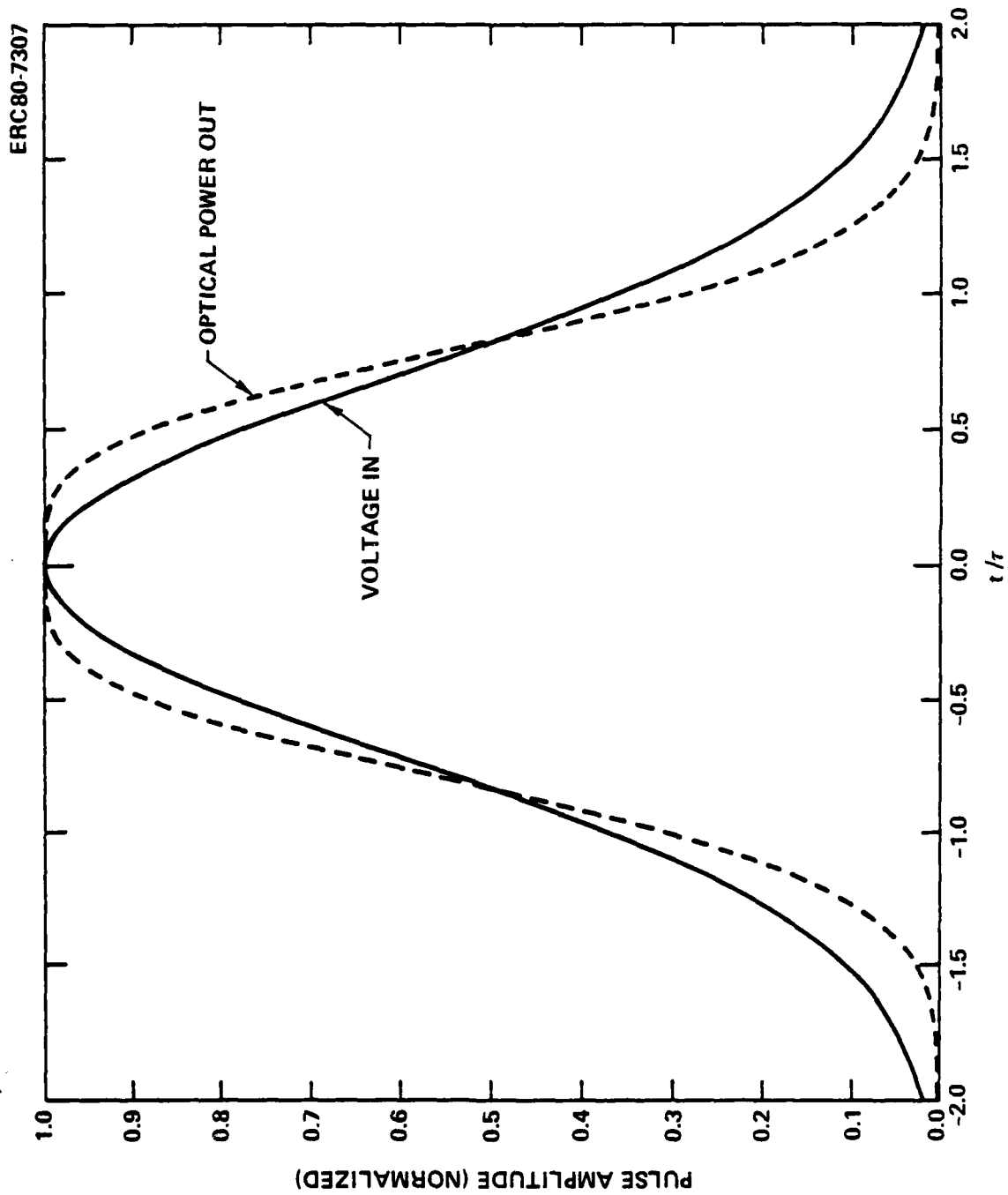


Fig. 3.38 Temporal response of switch transmission, with a peak phase shift between interferometer arms of π radians.



Rockwell International

ERC41015.4FR

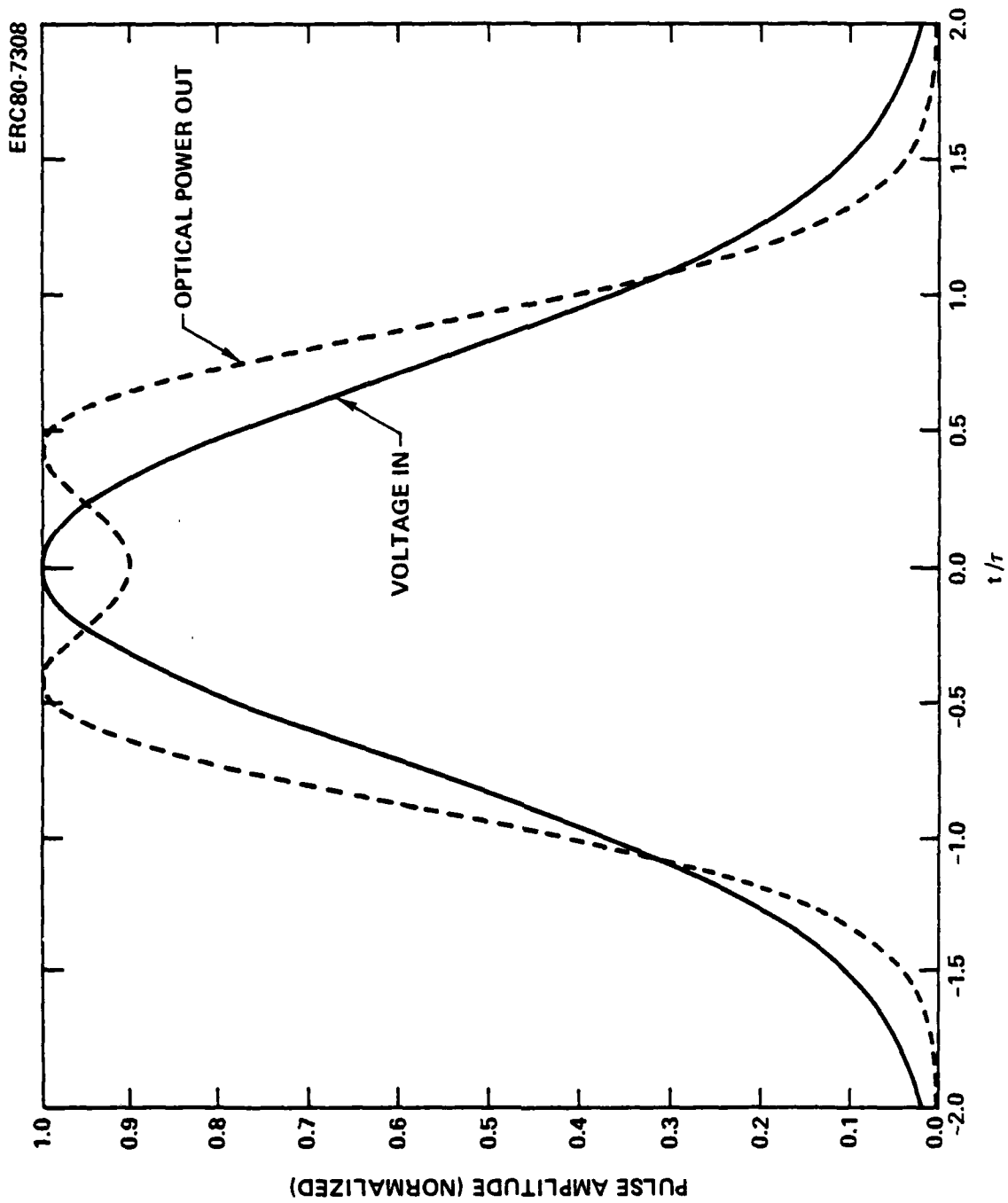


Fig. 3.39 Temporal response of switch transmission, with peak phase shift between interferometer arms of 1.2π radians.

such a system is the frequency selective coupler, for combining and separating the channels. The use of parallel single-mode optical waveguides as a codirectional frequency selective coupler has been proposed⁴² and demonstrated.⁴³⁻⁴⁵ Contradirectional frequency-selective couplers in which phase matching is achieved by a spatially periodic refractive index perturbation have also been suggested.⁴⁶ The contradirectional coupler has the advantage of strong frequency selectivity (i.e., narrow passband) for short interaction length, but is more difficult to fabricate because of the short-period gratings which are required.

This section treats the design and performance of contradirectional frequency-selective couplers for use in single-mode optical fiber communications, as illustrated in Fig. 3.40. It should be noted that this type of coupler is a reciprocal device, and as such can combine, as well as separate, optical frequency channels.

3.5.1 Periodic Perturbation and Mode Coupling

Periodic perturbations and specifically a corrugation over a thin film waveguide play an important role in a number of applications. These include grating light wave couplers,⁴⁷ Bragg reflectors,^{48,49} and distributed feedback lasers.⁵⁰ All of these applications involve the use of a periodic structure to furnish a Bragg momentum $2\pi/\Lambda$ (Λ = period) in order to satisfy the momentum conservation requirement for the desired coupling. In this section, we consider the coupling between two single-mode waveguides due to a periodic surface corrugation, as illustrated in Fig. 3.41. We assume that the uncorrugated parallel-waveguide structure can support at least two confined modes. A confined wave propagating in the composite waveguide structure can, in general, be represented as a linear combination of all the confined modes, i.e.,

$$\psi(x,y,z) = \sum A_\ell \psi_\ell(x,y) e^{i\beta_\ell z} \quad (3.5.1)$$



ERC41015.4FR

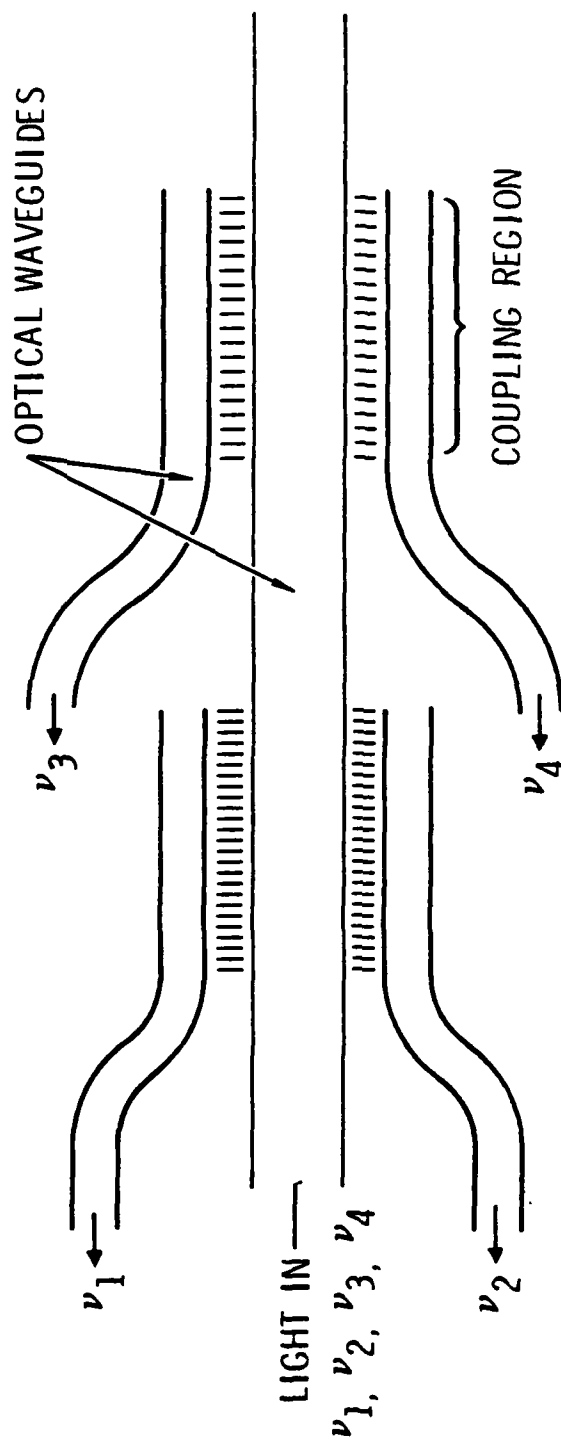


Fig. 3.40 Frequency-selective coupler for use in optical fiber communication.

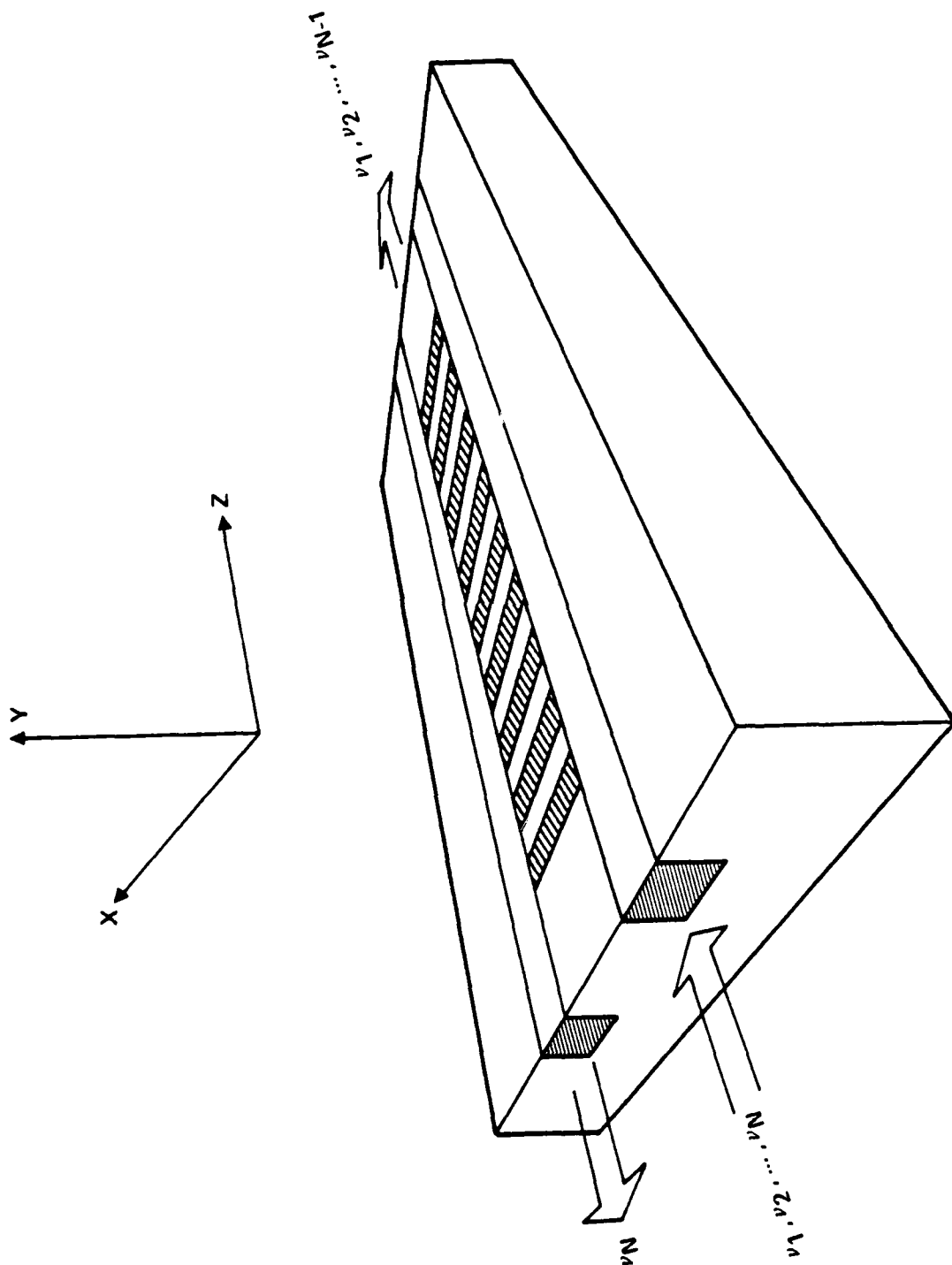


Fig. 3.41 Two waveguides coupled by a periodic refractive index perturbation.



ERC41015.4FR

where $\psi_\ell(x,y)e^{i\beta_\ell z}$ ($\ell = \pm 1, \pm 2, \dots$) are the eigenmode field distributions with propagation constants β_ℓ , and A_ℓ is the amplitude of the ℓ -th eigenmode. In the case of a perfect waveguide structure, the A_ℓ 's are constants and there is no mode coupling. If a dielectric perturbation is imposed on the waveguide, ψ in (3.5.1) is still a valid solution provided the A_ℓ 's are functions of z . A variation in the A_ℓ 's indicates that power is exchanged between the modes. In the following paragraphs, a set of coupled mode equations for the A_ℓ 's will be derived.

We start with the scalar wave equation

$$\left[\nabla^2 + \frac{\omega^2}{c^2} n^2(x,y) + \frac{\omega^2}{c^2} \Delta n^2(x,y,z) \right] \psi = 0 \quad (3.5.2)$$

where $\Delta n^2(x,y,z)$ represents the periodic dielectric perturbation. We will take this $\Delta n^2(x,y,z)$ as

$$\Delta n^2 = \mu(x,y) P(z) \quad (3.5.3)$$

where $P(z)$ is a periodic function of z and $\mu(x,y)$ depends on the geometry of the corrugation.

Substituting (3.5.1) into (3.5.2) and assuming "slow" variation of the amplitudes, we obtain

$$\frac{\beta_m}{|\beta_m|} \frac{dA_m}{dz} = \frac{1}{2} \left(\frac{\omega}{c} \right)^2 \sum_\ell \langle m | \mu | \ell \rangle A_\ell e^{i(\beta_\ell - \beta_m)z} P(z) \quad (3.5.4)$$

where

$$\langle m | \mu | \ell \rangle = \int \psi_m^*(x,y) \mu(x,y) \psi_\ell(x,y) dx dy, \quad (3.5.5)$$

the mode fields are normalized according to the relation

$$|\beta_m| \langle m | \ell \rangle = \delta_{m\ell} \quad (3.5.6)$$

and we recall that $\beta_{-\ell} = -\beta_\ell$.

We will now limit ourselves to a special case in which the whole waveguide structure supports only two confined modes, i.e., $\ell = \pm 1, \pm 2$. We will also only consider the first order Bragg coupling; in other words, we will take

$$P(z) = 2 \cos \left(\frac{2\pi}{\Lambda} z \right) = e^{i \left(\frac{2\pi z}{\Lambda} \right)} + e^{-i \left(\frac{2\pi z}{\Lambda} \right)} \quad (3.5.7)$$

For operation near the Bragg resonant conditions, we only have to keep terms in (3.5.7) with nearly zero phase variation (i.e., $|\beta_m - \beta_\ell| = 2\pi/\Lambda$). We can also discuss the different types of resonant coupling separately, provided these resonances do not overlap. In this case, we can consider coupling between one forward-propagating mode with amplitude A_ℓ and one backward propagating mode with amplitude A_m . Then the coupled mode equations can be written

$$\frac{dA_\ell}{dz} = \kappa_{\ell m} e^{i \Delta_{\ell m} z} A_m \quad (3.5.8)$$

$$\frac{dA_m}{dz} = \kappa_{m\ell} e^{-i \Delta_{\ell m} z} A_\ell \quad (3.5.9)$$

with

$$\Delta_{\ell m} = \frac{2\pi}{\Lambda} - \beta_\ell + \beta_m \quad (3.5.10)$$

$$\kappa_{\ell m} = \frac{i}{2} \left(\frac{\omega}{c} \right)^2 \frac{\beta_\ell}{|\beta_\ell|} \langle m | u | \ell \rangle, \quad m, \ell = 1, 2 \quad (3.5.11)$$

Noting that β_ℓ is positive and β_m negative, it follows that

$$\kappa_{m\ell} = \kappa_{\ell m}^* = -\kappa_{\ell m}$$



ERC41015.4FR

Both direct and exchange Bragg coupling can occur, as discussed below.

Direct Bragg Coupling

Referring to the dispersion curves in Fig. 3.42, we consider the wave propagation near ω_1 and ω_2 where one of the direct Bragg conditions

$$\begin{aligned} 2 \beta_1(\omega_1) &= \frac{2\pi}{\Lambda} \\ 2 \beta_2(\omega_2) &= \frac{2\pi}{\Lambda} \end{aligned} \tag{3.5.12}$$

are satisfied. In these two cases, the waves are constructively reflected and coupled back to the same mode. The coupling constants are

$$\kappa_{11} = -\frac{i}{2} \left(\frac{\omega}{c}\right)^2 \iint \psi_1^2(x,y) u(x,y) dx dy \tag{3.5.13}$$

$$\kappa_{22} = -\frac{i}{2} \left(\frac{\omega}{c}\right)^2 \iint \psi_2^2(x,y) u(x,y) dx dy \tag{3.5.14}$$

We notice that for a range of ω around ω_1 and ω_2 , the propagation constants for the perturbed structure are complex⁵¹. These are the so-called "forbidden gaps". The bandgaps are given approximately by⁵¹

$$\begin{aligned} \delta\omega_1 &\approx 2|\kappa_{11}| c/n_{\text{eff}} \\ \delta\omega_2 &\approx 2|\kappa_{22}| c/n_{\text{eff}} \end{aligned} \tag{3.5.15}$$

where n_{eff} is the effective index of refraction of the mode.

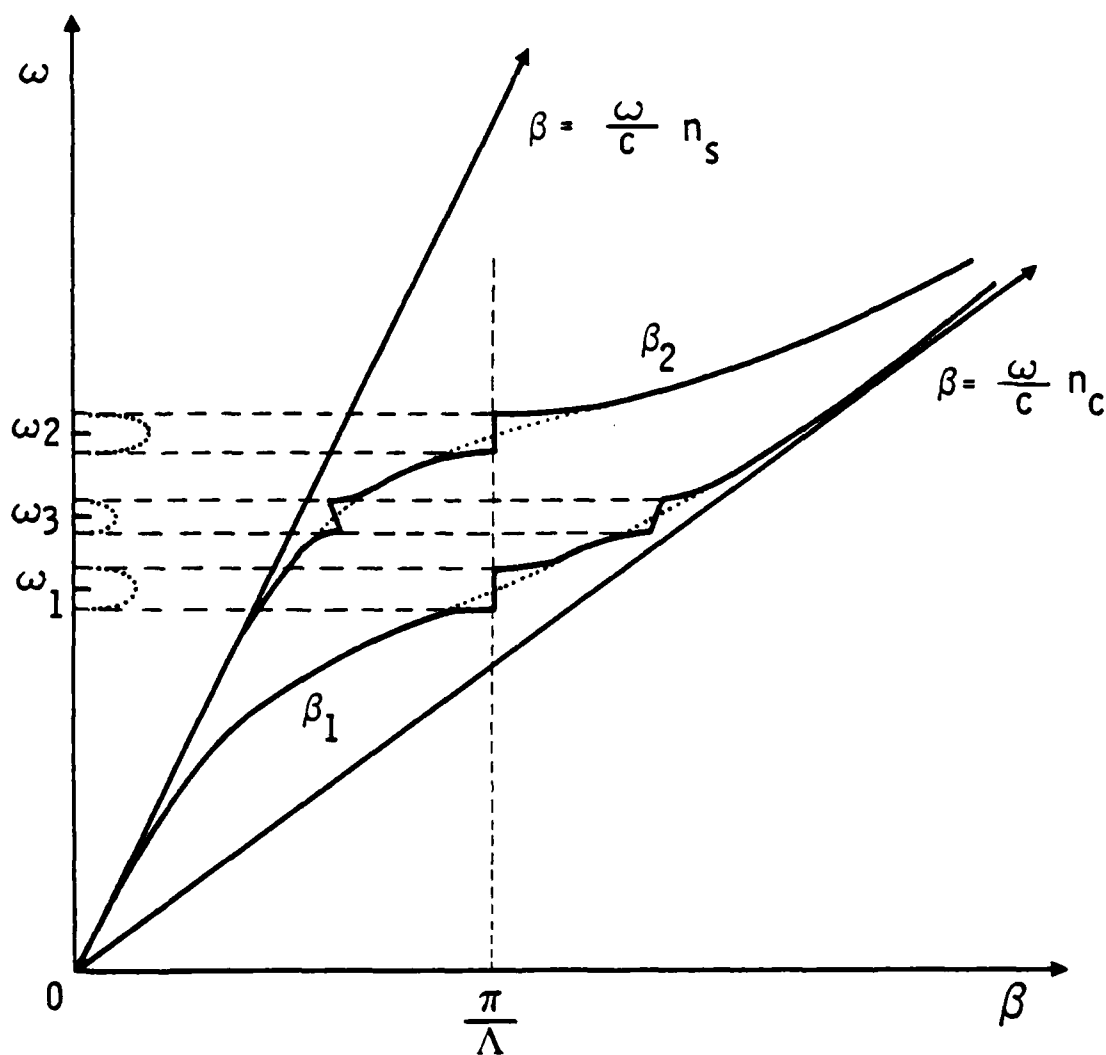


Fig. 3.42 Dispersion curves for coupled waveguides illustrating direct and exchange Bragg coupling.



ERC41015.4FR

Exchange Bragg Coupling

In the frequency regimes near ω_3 , where the exchange Bragg condition is satisfied

$$\beta_1 + \beta_2 = \frac{2\pi}{\Lambda} \quad (3.5.16)$$

This is the situation when the energy of one mode is constructively converted to the energy of the other contra-directional propagating mode. This phenomenon is similar to the exchange Bragg reflection in a periodic birefringent layered medium where the energy of a wave with one polarization state is constructively converted to the energy of a reflected wave with the other polarization state¹¹. The coupling constant of this effect is

$$\kappa_{12} = \frac{1}{2} \left(\frac{\omega}{c} \right)^2 \int \psi_1(x,y) \mu(x,y) \psi_2(x,y) dx dy \quad (3.5.17)$$

The corresponding bandgap is given approximately by

$$\Delta\omega_3 \approx 2|\kappa_{12}| c/n_{\text{eff}} \quad (3.5.18)$$

The solutions of the coupled mode equations for resonant Bragg coupling can be found in any standard textbook.⁵³ In either type of Bragg coupling, the ratio of reflected to incident power R is given by

$$R = \frac{\kappa^2 \sinh^2(SL)}{\kappa^2 \sinh^2(SL) + S^2} \quad (3.5.19)$$

where L is the length of the interaction region,

$$S^2 = |\kappa|^2 - \left(\frac{\Delta}{2} \right)^2, \quad (3.5.20)$$

and the subscripts ($m\ell$) have been omitted for convenience. It is understood in (3.5.19) that if S^2 is negative, then $\sinh^2(SL) \rightarrow \sin^2(|SL|)$. At resonance ($\Delta=0$), (3.5.19) reduces to

$$R = \tanh^2 (|\kappa|L) \quad (3.5.21)$$

It is possible to write Δ in terms of $\nu - \nu_0$, the deviation in frequency from the frequency at resonance ν_0 . If $|n_c - n_s|/n_s \ll 1$, where n_c and n_s are the core and substrate refractive indices of the waveguides, then

$$\Delta = - \frac{4\pi n_s}{c} (\nu - \nu_0) \quad (3.5.22)$$

The coupling efficiency for the contradirectional coupler is plotted in Fig. 3.43 as a function of ΔL for $\kappa L = \pi/2$, π , and $3\pi/2$. Note that increases in κ cause an increase in coupling efficiency at resonance, a broadening of the central peak, and an increase in the amplitude of the side lobes.

The side lobes can be a particularly troublesome problem in communications, as they cause crosstalk between multiplexed data channels. It has been shown for codirectional frequency selective couplers that the side lobes can be greatly reduced by varying the coupling constant gradually along the length of the coupling region.⁴⁵ In the contradirectional coupler, the coupling strength can be varied by changing the length of the corrugations, as illustrated in Fig. 3.44. The effect of varying κ along the length of a contradirectional coupler has been investigated using difference equation techniques to obtain numerical solutions to the coupled mode equations. The coupling constant was assumed to have a Gaussian variation of the form

$$\begin{aligned} \kappa(z) &= \kappa_0 e^{-T(z-L/2)^2/L^2}, \quad 0 \leq z \leq L \\ &= 0 \text{ elsewhere} \end{aligned} \quad (3.5.23)$$

where κ_0 and T are constants. The difference equation solution proceeded in the negative z -direction from $z=L$, where the initial condition $A_z(L) = C$, $A_m(L)=0$ was applied. Here C is an arbitrary constant, and A_z and A_m are amplitudes of the incident (forward-propagating) and reflected (backward propagating) waves. The coupling efficiency is given by



ERC41015.4FR

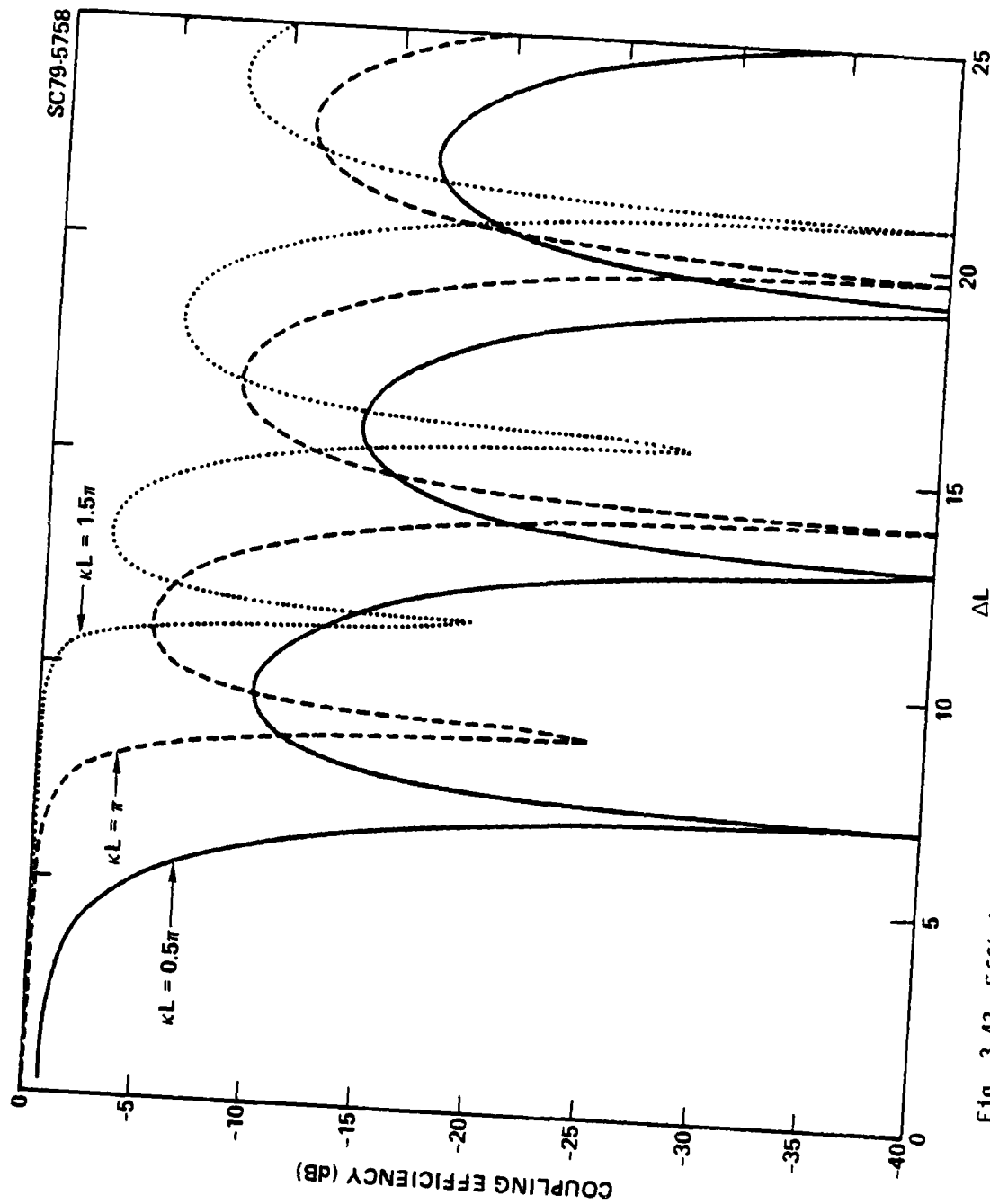


Fig. 3.43 Efficiency of coupling of optical power from a forward-propagating mode into a backward propagating mode, plotted as a function of the phase mismatch parameter ΔL , for three values of the coupling strength parameter κL . The coupling constant κ is assumed to be uniform along the length of the coupling region.

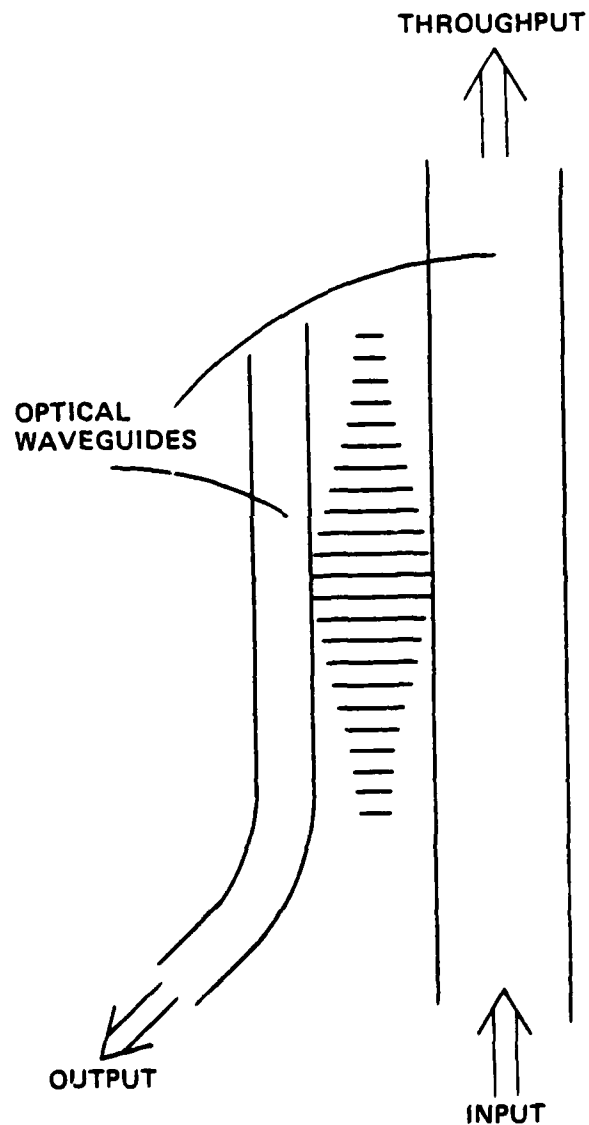


Fig. 3.44 Tapering of the coupling strength by varying the lengths of the surface corrugations.



ERC41015.4FR

$$R = |A_m(0)/A_e(0)|^2 \quad (3.5.24)$$

The dependence of reflected power on phase mismatch is plotted in Fig. 3.45, for $T=0$ (uniform coupling), $T=\pi/2$, and $T=\pi$. Note the substantial reduction in side-lobe power resulting from the use of the tapered coupling scheme.

3.5.2 Coupling Parameters for Parallel Channel Waveguides

In order to gain a practical understanding of the design of contradi-rectional wavelength-selective couplers, some numerical results are obtained for the case of rectangular-core channel waveguides with a periodic surface cor- rugation in between. First, expressions for the field distributions and pro- pagation constants for a single isolated waveguide are derived. Then, these results are used to determine the corresponding parameters for two parallel waveguides. Finally, the coupling parameters κ_{11} , κ_{12} , and κ_{22} are calculated for a surface corrugation between the waveguides.

Rectangular Dielectric Waveguides

We start by reviewing the wave propagation in a rectangular dielectric waveguide. The geometry of this waveguide is sketched in Fig. 3.46. The refractive index profile is given by:

$$n^2(x,y) = \begin{cases} n_0^2 & y > 0 \\ n_c^2 & |x| < a/2 \text{ and } -d < y < 0 \\ n_s^2 & \text{otherwise} \end{cases} \quad (3.5.25)$$

where we choose z -axis as the direction of propagation. In order to support a confined mode, the core refractive index n_c must be greater than the substrate index n_s and the superstrate index n_0 (for air $n_0 = 1$). The wave propagation obeys the following equation⁵⁴

$$\frac{\partial^2}{\partial x^2} + \frac{\partial^2}{\partial y^2} + \frac{\omega^2}{c^2} n^2(x,y) - \beta^2 \frac{E}{H} = 0 \quad (3.5.26)$$

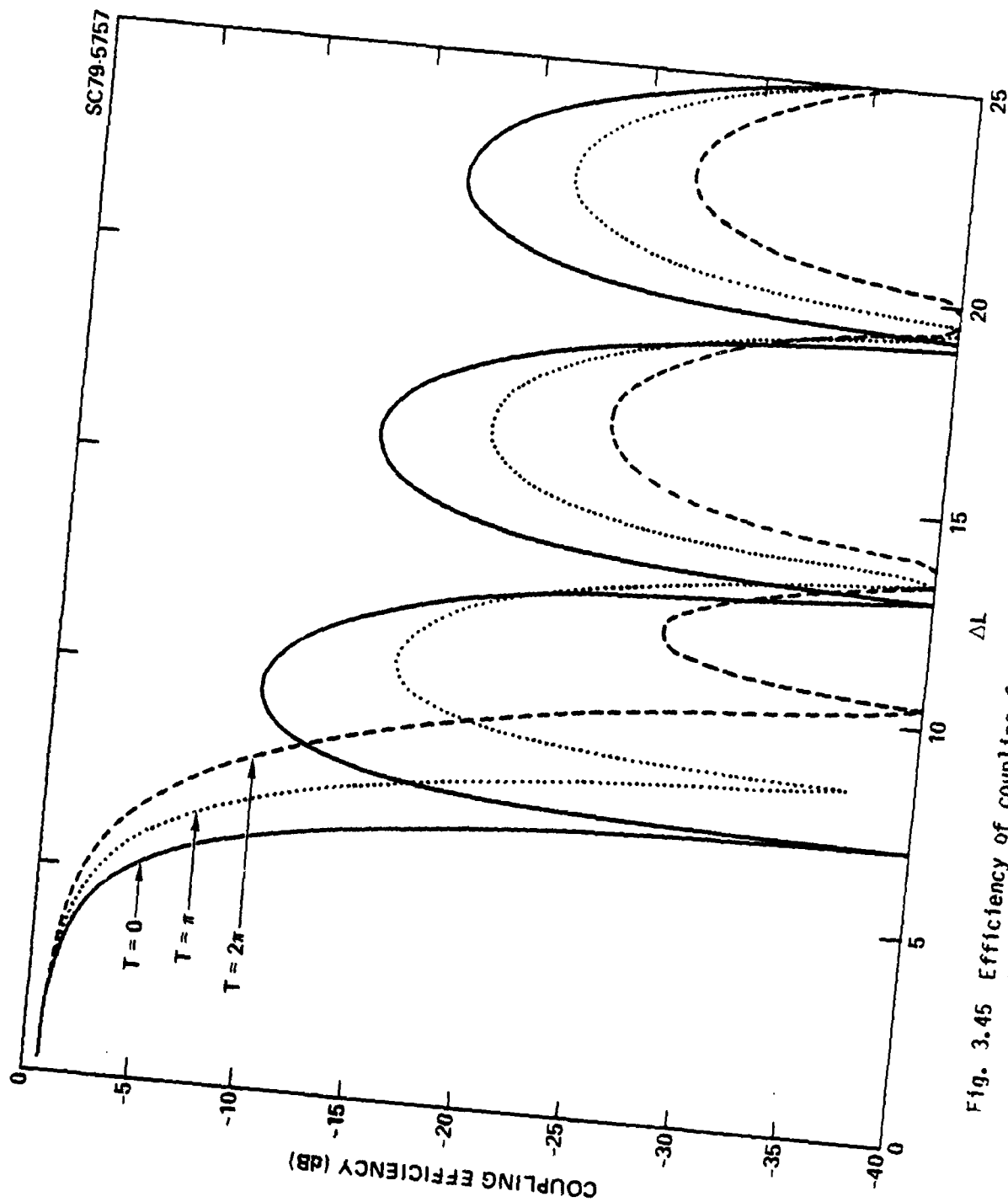


Fig. 3.45 Efficiency of coupling from forward-propagating mode to a backward-propagating mode, plotted as a function of the phase-mismatch parameter ΔL , for three values of the tapering constant T . It is assumed that $\int_C L_{\text{kd}z} = \pi$ for each of the curves.



Rockwell International

ERC41015.4FR

SC79-3550-A

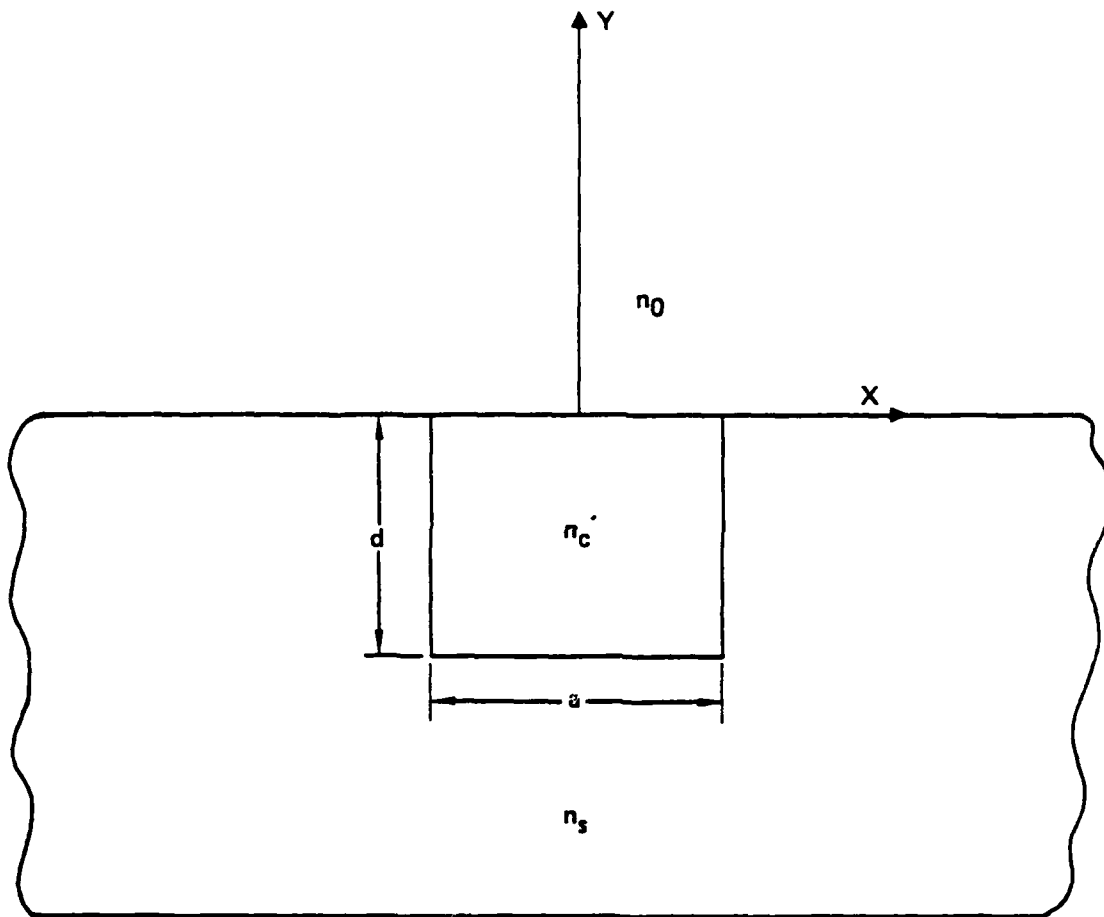


Fig. 3.46 Rectangular-core dielectric waveguide.

where we have assumed a sinusoidal time dependence as well as a sinusoidal variation of the fields in the z-direction, i.e., $e^{i(\beta z - \omega t)}$. Boundary conditions must be matched at the waveguide interfaces where $n^2(x,y)$ is not continuous and Eq. (3.5.26) is not valid.

A closed form solution of Eq. (3.5.26) can be obtained by the method of separation of variables if $n^2(x,y)$ is separable. This problem was studied by Marcatili⁵⁵. He introduced an approximate separation of $n^2(x,y)$ and obtained a closed form solution. In his approach, $n^2(x,y)$ is approximately given by:

$$n^2(x,y) \cong u(x) + v(y) - n_c^2 \cong n_m^2(x,y) \quad (3.5.27)$$

where

$$u(x) = \begin{cases} n_s^2 & |x| > a/2 \\ n_c^2 & |x| < a/2 \end{cases} \quad (3.5.28)$$

and

$$v(y) = \begin{cases} n_s^2 & y < -b \\ n_c^2 & -b < y < 0 \\ n_0^2 & 0 < y \end{cases} \quad (3.5.29)$$

By using the approximation (3.5.27) the wave function $\psi(x,y,z)$ (ψ = any component of E or H) can be written as a product of plane wave solutions in the form

$$\psi(x,y,z) = U(x) V(y) e^{i\beta z} \quad (3.5.30)$$

with $U(x)$ and $V(y)$ satisfying the following equations



ERC41015.4FR

$$\left[\frac{d^2}{dx^2} + \frac{\omega^2}{c^2} u(x) \right] U(x) = \beta_u^2 U(x) \quad (3.5.31)$$

$$\left[\frac{d^2}{dy^2} + \frac{\omega^2}{c^2} v(y) \right] V(y) = \beta_v^2 V(y) \quad (3.5.32)$$

and

$$\beta^2 = \beta_u^2 + \beta_v^2 - \frac{\omega^2}{c^2} n_c^2. \quad (3.5.33)$$

In these expressions, $U(x)$ and $V(y)$ are actually the waveguide modes of the slab waveguides described by Eqs. (3.5.28) and (3.5.29), respectively, and β_u and β_v are the propagation constants of the slab waveguide modes $U(x)$ and $V(y)$, respectively. The dispersion relations and some characteristics can be found in Ref. 55.

To compare the approximate index profile with the actual one, we redraw in Fig. 3.47 the cross section of the waveguide subdivided in many areas. Here, $n^2(x,y)$ and $n_m^2(x,y)$ are identical only in the unshaded areas and they are different by $\delta \equiv n_c^2 - n_s^2$ in the four shaded areas. This separation yields a good approximation to the solution of Eq. (3.5.26) provided the modes are well-confined since most of the power is guided in the core and only a small error will be introduced. As a matter of fact, if one uses the closed form solution obtained from this approximation as a trial function, one can obtain a better approximation for the propagation constants by the variational method⁵⁶. It can be shown that the wave propagation constant obtained from the variational method is given by

$$\beta^2 = \beta_m^2 - (n_c^2 - n_s^2)(2\pi/\lambda)^2 \Gamma \quad (3.5.34)$$

where Γ is a number which represents the fractional part of the power flowing in the shaded regions of Fig. 3.47 and β_m^2 is the wave propagation constant obtained from Marcattilli's approximation. For the fundamental mode, the value of β

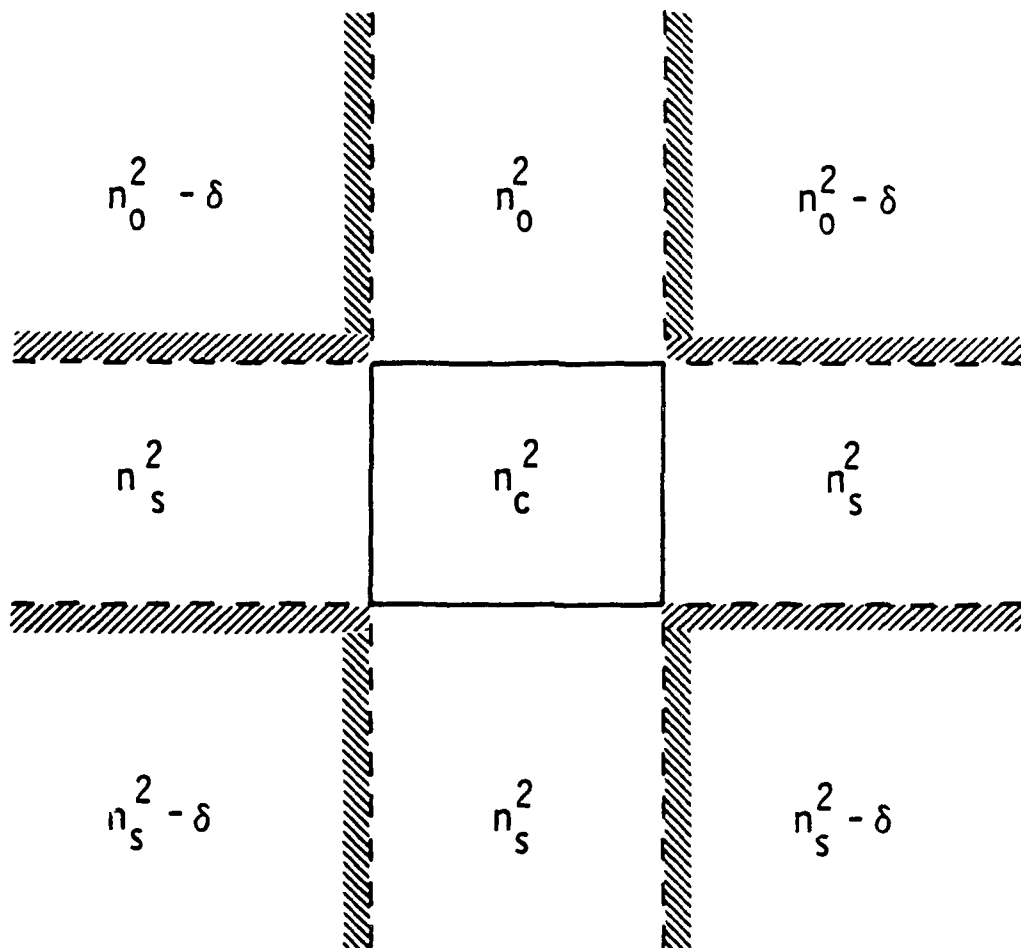


Fig. 3.47 Illustration of regions in which the product-of-plane-wave solutions in Eq. (3.5.30) do not satisfy the scalar wave equation.



ERC41015.4FR

obtained in this way represents a lower bound to the true propagation constant. A typical dispersion curve obtained by the variational method using (3.5.34) is compared with Marcatilli's approximation in Fig. 3.48.

Two Parallel Dielectric Waveguides

We consider the coupling between two rectangular waveguides separated by a finite distance from each other. The geometry of the waveguide structure is sketched in Fig. 3.49. The wave propagation in two parallel waveguides is similar to the electron motion in a two-atom molecule. Let $\phi_a(x,y)e^{i\beta_a z}$ and $\phi_b(x,y)e^{i\beta_b z}$ be the fundamental modes of the individual waveguides when they are far apart. The waveguide modes of the composite structure can be approximated by⁵⁷

$$\psi(x,y)e^{i\beta z} = [C_a \phi_a(x,y) + C_b \phi_b(x,y)]e^{i\beta z} \quad (3.5.35)$$

provided the two waveguides are not too close to each other.

To calculate the propagation constant β , and evaluate the constants C_a and C_b , we decompose the refractive index profile into three parts, and we get

$$n^2(x,y) = s^2(x,y) + \Delta n_a^2(x,y) + \Delta n_b^2(x,y) \quad (3.5.36)$$

where

$$s^2(x,y) = \begin{cases} n_0^2 & \text{air} \\ n_s^2 & \text{substrate} \end{cases} \quad (3.5.37)$$

$$\Delta n_\alpha^2(x,y) = \begin{cases} n_\alpha^2 - n_s^2 & \text{waveguide } \alpha \quad \alpha = a, b \\ 0 & \text{otherwise} \end{cases} \quad (3.5.38)$$

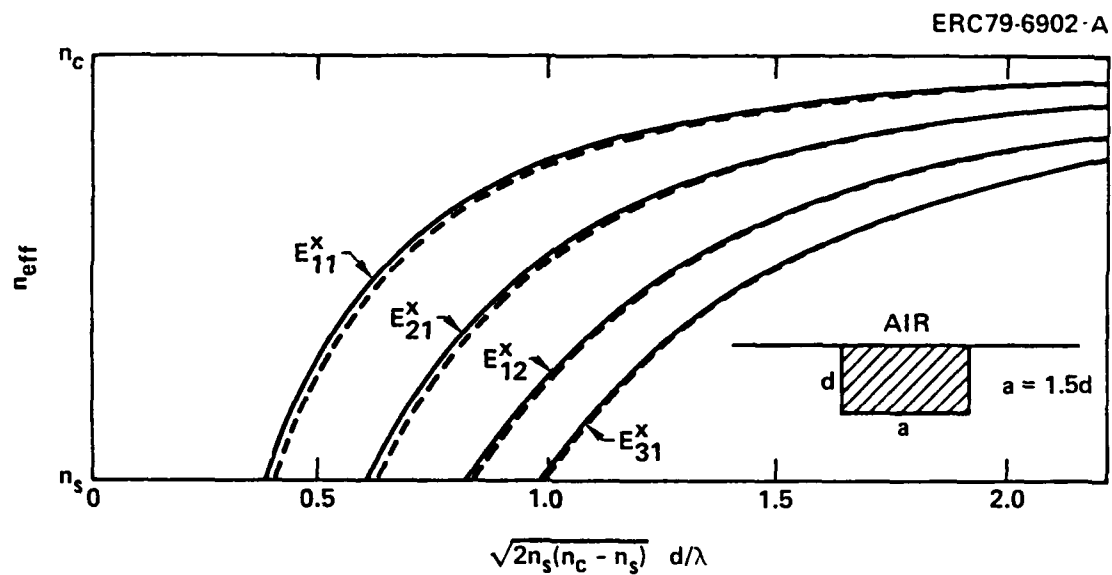


Fig. 3.48 Dispersion curves for rectangular-core waveguides. Marcattilli's approximation (dashed curve); variational method (solid curve).

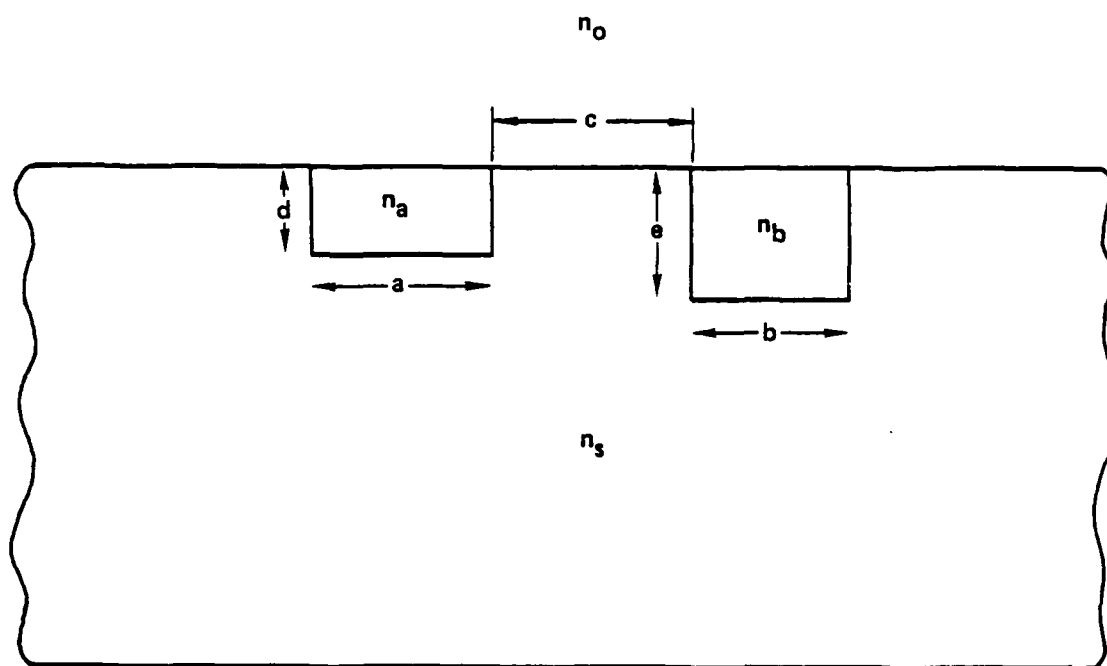


Fig. 3.49 Coupled rectangular-core waveguides.

and n_a and n_b are the refractive indices of the cores respectively. Physically, $s^2(x,y)$ represents the substrate and $\Delta n_a^2(x,y)$ represents the presence of the waveguide core. It is thus obvious that the individual waveguide modes ϕ_α satisfy the following equation

$$\left\{ \frac{\partial^2}{\partial x^2} + \frac{\partial^2}{\partial y^2} + \frac{\omega^2}{c^2} \left[s^2(x,y) + \Delta n_a^2(x,y) \right] \right\} \phi_\alpha = \beta_\alpha^2 \phi_\alpha \quad (3.5.39)$$

$\alpha = a, b$

Substituting (3.5.35) and (3.5.36) into the wave equation (3.5.26) and using (3.5.39), we obtain

$$\begin{aligned} & C_a \left[\beta_a^2 + \frac{\omega^2}{c^2} \Delta n_b^2(x,y) - \beta^2 \right] \phi_a \\ & + C_b \left[\beta_b^2 + \frac{\omega^2}{c^2} \Delta n_a^2(x,y) - \beta^2 \right] \phi_b = 0 \end{aligned} \quad (3.5.40)$$

We multiply (3.5.40) by ϕ_α and integrate over all x and y to obtain

$$\begin{pmatrix} \beta_a^2 - \beta^2 + K_b \\ J_b + I(\beta_a^2 - \beta^2) \end{pmatrix} \begin{pmatrix} J_a + I(\beta_b^2 - \beta^2) \\ \beta_b^2 - \beta^2 + K_a \end{pmatrix} \begin{pmatrix} C_a \\ C_b \end{pmatrix} = 0 \quad (3.5.41)$$

with

$$\begin{aligned} I &= \int \phi_b \phi_a \, dx dy \\ J_a &= (\omega/c)^2 (n_a^2 - n_s^2) \int_a \phi_b \phi_a \, dx dy \\ J_b &= (\omega/c)^2 (n_b^2 - n_s^2) \int_b \phi_b \phi_b \, dx dy \\ K_a &= (\omega/c)^2 (n_a^2 - n_s^2) \int_a \phi_b^2 \, dx dy \\ K_b &= (\omega/c)^2 (n_b^2 - n_s^2) \int_b \phi_a^2 \, dx dy \\ \int \phi_a^2 \, dx dy &= \int \phi_b^2 \, dx dy = 1 \end{aligned} \quad (3.5.42)$$



ERC41015.4FR

The integral signs \int_a and \int_b indicate that the integrations are over the core region of waveguides a and b, respectively, I is the overlap integral of the two individual wave functions which are not orthogonal to each other, K_a and K_b are the dielectric perturbations to one of the waveguides due to the presence of the other waveguide, and J_a and J_b represent the exchange coupling between the two waveguides.

The eigenvalues β_1 and β_2 are the solutions of the secular equation

$$\begin{vmatrix} \beta_a^2 - \beta^2 + K_b & J_a + I(\beta_b^2 - \beta^2) \\ J_b + I(\beta_a^2 - \beta^2) & \beta_b^2 - \beta^2 + K_a \end{vmatrix} = 0 \quad (3.5.43)$$

This is a quadratic equation in β^2 and, in general, will yield two desired propagation constants β_1 , β_2 . The corresponding wave functions (3.5.35) can be obtained from (3.5.41) by solving for C_a and C_b .

The expressions are much simpler in the degenerate case when the two waveguides are identical, i.e., $\beta_a^2 = \beta_b^2 \equiv \beta_0^2$, $K_a = K_b \equiv K$ and $J_a = J_b \equiv J$. In this case, the propagation constants and the corresponding wave functions are given by

$$\beta^2 = \beta_0^2 + \frac{K \pm J}{1 \pm I} \quad (3.5.44)$$

$$\psi = \frac{1}{\sqrt{2(1 \pm I)}} (\phi_a \pm \phi_b) \quad (3.5.45)$$

The "+" sign is for the symmetric one and the "-" sign is for the antisymmetric one. the factor $1/\sqrt{2(1 \pm I)}$ is the normalization coefficient. We also note that these two solutions are already mutually orthogonal.

The perturbation approach we have just discussed can be applied to any waveguide geometry provided the individual wave functions ϕ_a and ϕ_b , as well as the corresponding propagation constants β_a and β_b are known. There is one special case where we can apply the Marcatili approximation directly to get the wave functions of the composite waveguide structure and use (3.5.34) to get a better approximation for the propagation constants. This is the case in which the two rectangular waveguides have the same depth and the same core index n_c , i.e., $d_a = d_b = d$, and $n_a = n_b = n_c$. The partial wave function $U(x)$ and the corresponding propagation constant β_U can be easily obtained from the matrix method developed by Yeh et al.⁴⁸ $U(x)$ is actually the wave function of a two-slab multilayer waveguide which has also been studied by Stotts⁵⁸ and Yajima.⁵⁹ The dispersion relation of β_U for E^Y modes⁶⁰ is given by

$$\left[1 - \frac{1}{2} \left(\frac{h}{p} - \frac{p}{h}\right) \tan ha\right] \left[1 - \frac{1}{2} \left(\frac{h}{p} - \frac{p}{h}\right) \tan hb\right] + e^{-2pc} \left[-\frac{1}{4} \left(\frac{h}{p} + \frac{p}{h}\right)^2\right] \tan ha \tan hb = 0 \quad (3.5.46)$$

where

$$h = [(n_c \omega / c)^2 - \beta_U^2]^{1/2} \quad (3.5.47)$$

$$p = [\beta_U^2 - (n_s \omega / c)^2]^{1/2}$$

and a and b are the widths of the waveguides and c is the separation. The dispersion relation of β_U for E^X modes is similar to that of the E^Y modes, except that h/p in (3.5.46) must be replaced by $(h/n_c^2)/(p/n_s^2)$. In the limit of small core-substrate index difference ($n_c - n_s \ll n_s$), dispersion curves for E^X and E^Y modes are the same. A typical dispersion curve for the E^X modes of the parallel coupled waveguides in the limit of small core-substrate index difference is shown in Fig. 3.50. The field distributions E_x of E_{11}^X and E_{21}^X modes are also depicted in Fig. 3.51.

The critical parameters for the frequency selective couplers are the propagation constants for the two guided modes β_1 and β_2 and the coupling

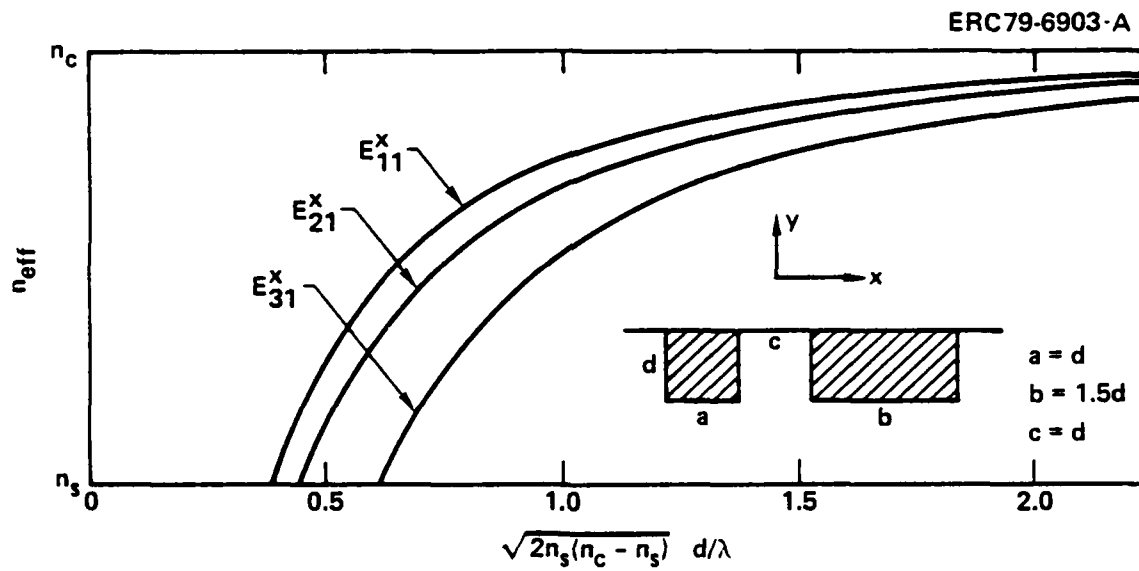


Fig. 3.50 Dispersion curve for coupled rectangular-core waveguides.

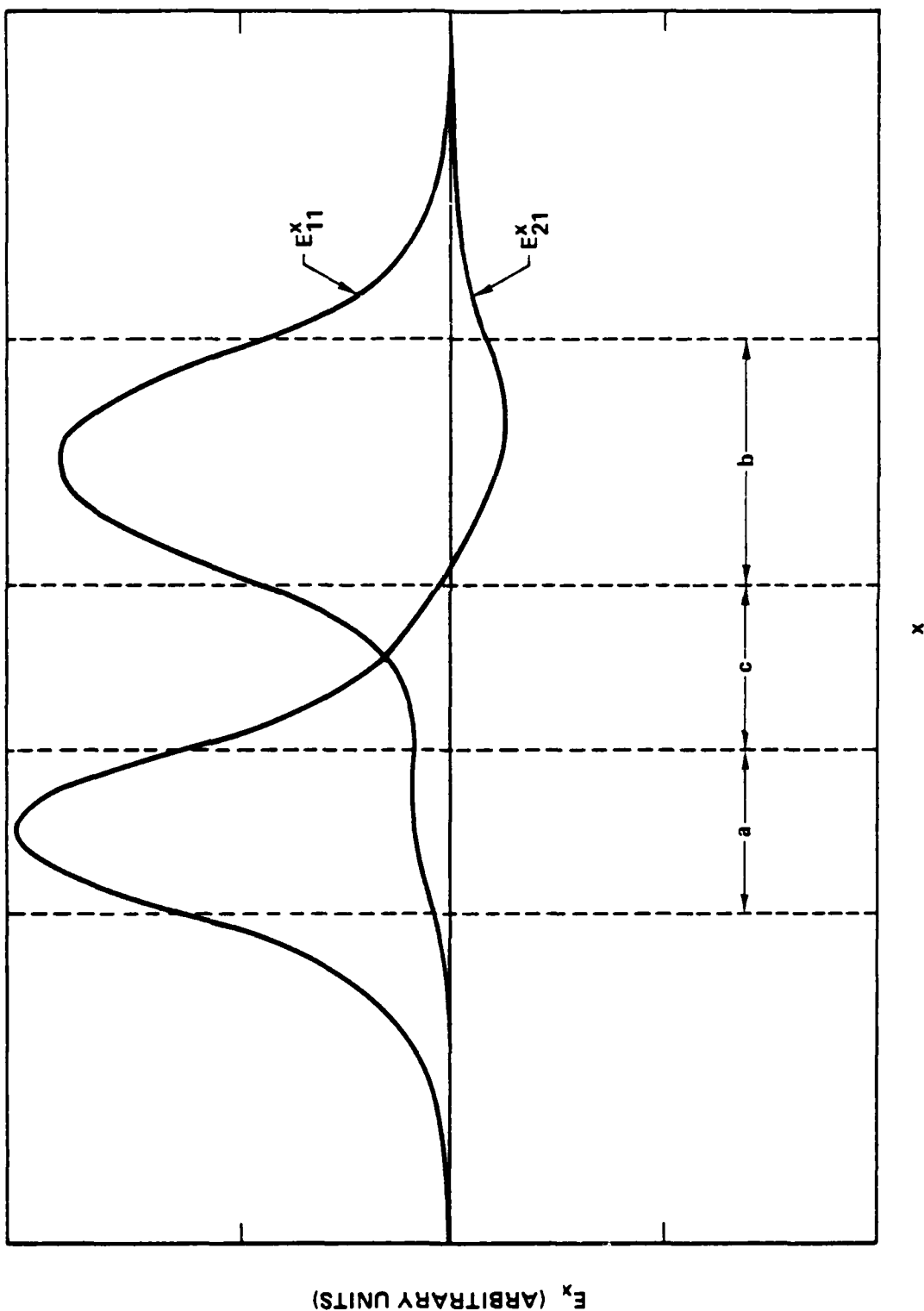


Fig. 3.51 Field distributions for the two guided modes of the coupled waveguides.

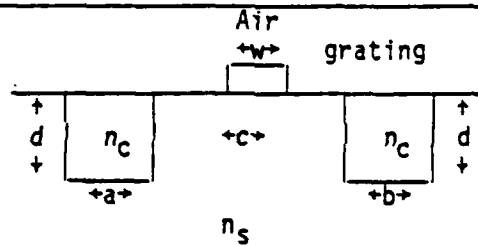


ERC41015.4FR

constants κ_{11} , κ_{12} and κ_{22} . Propagation constants can be obtained from the dispersion curves such as the one in Fig. 3.50, while the coupling constants for a periodic surface corrugation are calculated from (3.5.13), (3.5.14) and (3.5.17), using field distributions such as those in Fig. 3.51. Some numerical results are given in Table 3.6 for specific values of the waveguide parameters.

Table 3.6

Characteristics of a Grating Directional Coupler



$\sqrt{2n_s(n_c - n_s)}d/\lambda$	$\frac{\lambda(\beta_1 - \beta_2)}{2\pi(n_c - n_s)}$	$\frac{w}{c}$	κ_{12}	$\frac{\kappa_{11}}{\kappa_{12}}$	$\frac{\kappa_{22}}{\kappa_{12}}$
0.47	0.15	.5	0.21	0.91	1.7
0.47	0.15	1	0.44	1.5	2.9
0.62	0.12	.5	0.042	0.94	2.4
0.62	0.12	1	0.092	2.5	6.0

In all cases $a = c = d$ and $b = 1.5 d$.

$$\kappa_{12} = \frac{|\kappa_{12}|}{n_s(n_c - n_s)} \frac{\lambda}{2\pi} \left(\frac{d}{t}\right)^2$$

3.5.3 Device Design Example

A frequency-selective coupler for optical communications as described in this paper will utilize a primary waveguide and satellite waveguides coupled to the primary waveguide by periodic refractive index perturbations, as illustrated in Fig. 3.40. The primary waveguide transmits two or more frequency channels with center frequency ν_n , $n=1,2,\dots,N$ and spectral width $\Delta\nu$. Each satellite waveguide is intended to receive the power from one frequency channel, as determined by the spatial period of the index variation. The design of a practical coupler should provide for

- (1) efficient transfer of power at frequencies within each channel into the corresponding satellite waveguide (to minimize coupler insertion loss).
- (2) low transfer efficiency from any channel to satellite waveguides other than the assigned one (to ensure low crosstalk between channels).
- (3) low reflection in the primary waveguide for all frequency channels (to eliminate "ringing" in the system).

As an example, the spectral response of a coupler with a central wavelength of 8000Å has been calculated for a particular set of design parameters. Referring to Table 3.6, the numerical values chosen for these parameters are $n_c = 3.6$, $n_s = 3.5$, $a = c = d = .46 \mu\text{m}$, $b = .68 \mu\text{m}$, $w = .5c = .23 \mu\text{m}$, and from the first row of that table, $\kappa_{12} = .21$, $\kappa_{11}/\kappa_{12} = 0.91$, $\kappa_{22}/\kappa_{12} = 1.7$. Other parameters used in the example are T (the taper parameter) $= 2\pi$, L (the length of the coupling region) $= 440 \mu\text{m}$, $\int_0^L \kappa_{12} dz = .75\pi$, and t (the corrugation depth) $= 215\text{Å}$. The values for the corrugation width w and coupling parameter κ_{12} taper from the values given above at the center to $e^{-\pi/2} = 21\%$ of those values at the ends of the region. The primary waveguide is assumed to be the wider of the two, of width $b = .68 \mu\text{m}$.



ERC41015.4FR

The calculated spectral response for contradirectional power transfer from the primary to the satellite waveguide is plotted in Fig. 3.52. The spectral width of a frequency channel in this example is $\Delta\nu = 5 \times 10^{-4} \nu_0$, where ν_0 is the central frequency. In terms of wavelength, $\Delta\nu$ corresponds to a 4Å spectral width. The maximum loss for frequencies within a channel is 1.4 dB. If the wavelength channels have a 6Å center-to-center spacing, as indicated in the example, the maximum crosstalk is -27 dB with respect to the incident power level. In Fig. 3.53 the curve in Fig. 3.52 giving the power coupled from the primary to the secondary waveguide is replotted on a scale with an expanded abscissa, along with spectra for reflection in the primary and secondary waveguides. For frequencies within the channel of spectral width $\Delta\nu$, the power reflected in the primary waveguide is at least -30 dB below the incident power level, and reflectance in the secondary waveguide is at least -25 dB below the incident power level.

3.5.4 Design and Fabrication Criteria

The design of contradirectional frequency-selective couplers for guided-wave optical communications should take into account factors such as crosstalk induced by side lobes in the coupler response curves and reflections in the primary waveguide due to direct Bragg coupling. The side lobes can be reduced considerably by tapering the coupling strength along the length of the coupler. In order to reduce both crosstalk and direct Bragg reflections, the design should provide for wide frequency separations between the peaks of the direct and exchange Bragg coupling bands. To accomplish this, parameters of the parallel-waveguide structure should be chosen such that the difference in guided-mode propagation constants at the selected frequency is large. Numerical examples show that a properly designed coupler can have narrow spectral response with a short coupling region, while maintaining high transfer efficiency, low crosstalk, and low reflection in the primary waveguide.

The primary difficulty with the practical realization of the contradirectional frequency-selective coupler is that of fabricating the

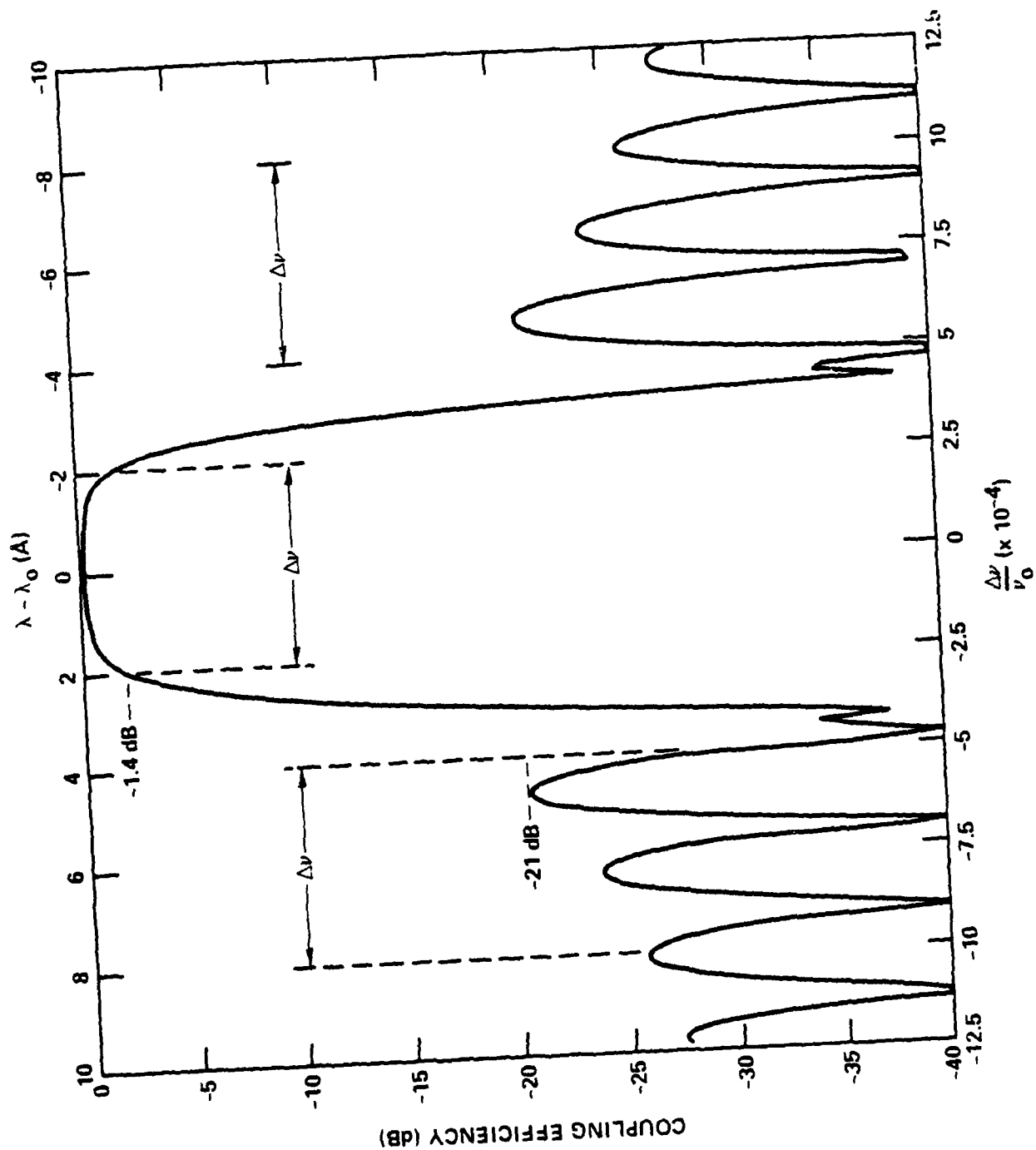


Fig. 3.52 Power transfer spectrum for contradiirectional coupling from primary to satellite waveguides, calculated using parameters given in text.



ERC41015.4FR

ERC79 6900

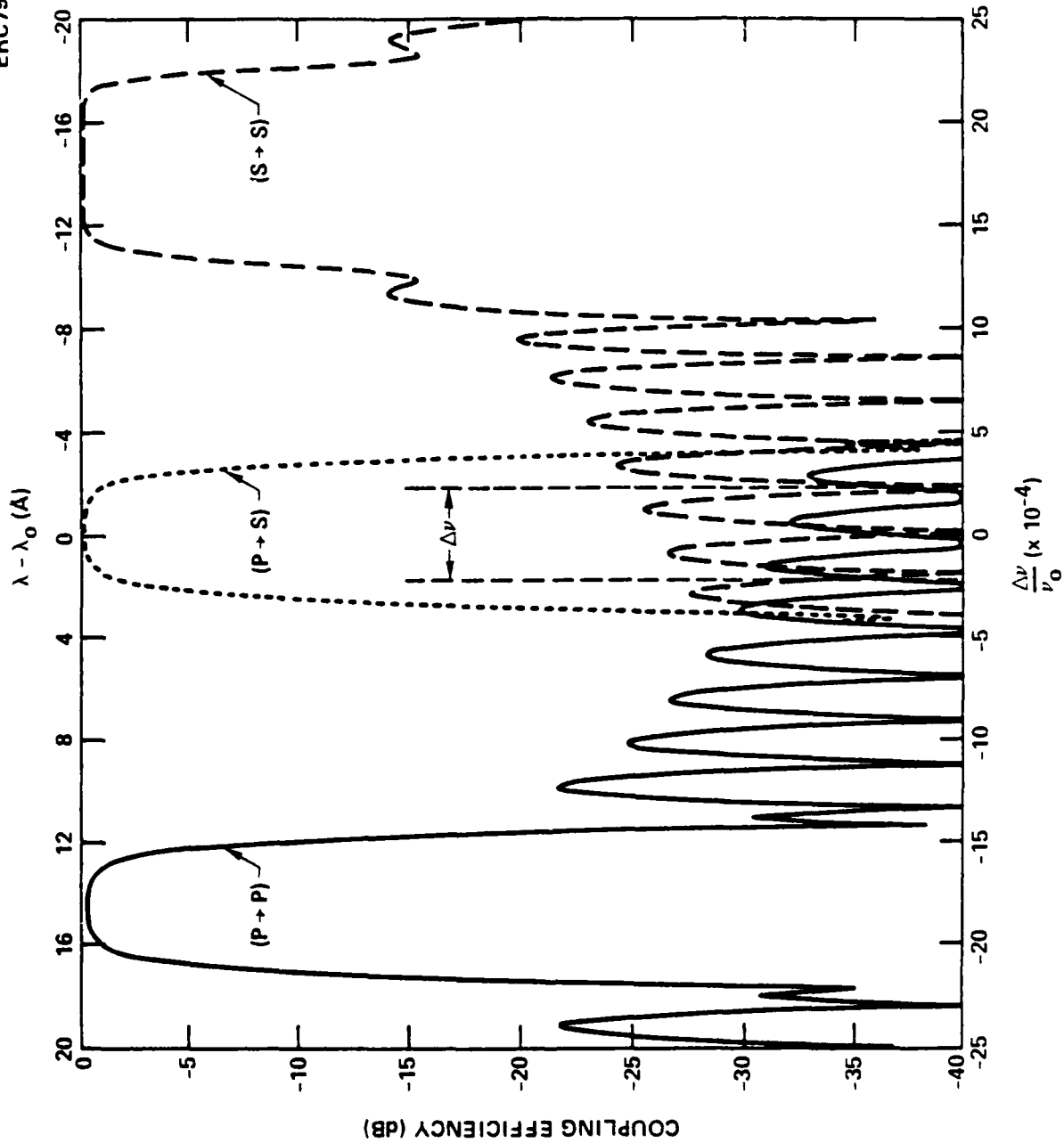


Fig. 3.53 Calculated power transfer spectra for coupling from primary-to-satellite (P→S), primary-to-primary (P→P), and satellite-to-satellite (S→S) waveguides.

ERC41015.4FR

short-period gratings required (e.g., $\Lambda = 1150\text{\AA}$ in GaAs and 1820°\AA in LiNbO_3 for a free-space optical wavelength of 8000°\AA). The resolution required is far beyond the limits of conventional photolithography. There appear to be two alternatives for obtaining the required resolution - electron beam writing, or holographic lithography utilizing the interference of two laser beams. In either case the pattern could be delineated directly on the wafer, or it could be written on a mask which would be used to produce the pattern on the wafer by x-ray lithography. At this time, it is not clear which of these techniques will eventually prove to be the more practical.



3.6 Summary

Each of the key components for the high-data-rate bus has been analyzed in some detail. The results are summarized below:

- (1) **Fibers.** Dispersion in doped silica single mode fibers limits the maximum data rate for a single-frequency channel to about 80 Gbit/s for a 100 m fiber length at a source wavelength of 0.8 μ m. For a local distribution system, as assumed in this study, the fiber bandwidth is more than adequate to handle the maximum data rate of which the transmitters and receivers are capable.
- (2) **Transmitters.** The two options for generation of the optical signal are direct modulation of a semiconductor laser and electro-optic modulation of light from a cw laser. The maximum data rate for a directly modulated laser, assuming photon injection from a second, cw laser, is estimated to be 5 Gbit/s for a 30 mW average power dissipation in the laser. The primary parameters which determine this limit are the spontaneous lifetime of electron-hole pairs in the active region of the laser and the photon lifetime in the laser cavity. Maximum data rates for electrooptic modulators using a buried electrode traveling wave configuration are estimated to be 10 Gbit/s for GaAlAs and 8 Gbit/s for LiNbO₃ for a 30 mW driving power level. The frequency dependence of current penetration depth in the modulating electrodes (skin effect), which leads to attenuation and distortion of the modulating waveform, is a key factor in determining the maximum data rate of the modulator. Phase mismatch between modulating signal and the optical wave is also a key factor in the case of LiNbO₃. For GaAlAs modulators, the relatively high optical attenuation is a matter of serious concern.

- (3) Receivers. An avalanche photodiode is the most appropriate type of photodetector for high-data-rate communication, as it combines high speed of response with internal gain to overcome the thermal noise in the amplifier circuit. Fastest response is obtained for unity gain. As the gain increases, the speed of response decreases and the optical power required to achieve a given bit error rate also decreases to a minimum, then begins to increase. The optimum gain for the receiver generally coincides with the minimum in the optical power curve. For a receiver containing a GaAs APD, the calculations indicate that the optimum gain is near 10, regardless of data rate. The minimum optical power for a 10^{-10} bit error rate is -28 dBm at a data rate of 5 Gbit/s and -25 dBm at 10 Gbit/s. However, it appears that the response of the GaAs FET amplifier following the APD would limit the maximum practical receiver data rate to about 5 Gbit/s.
- (4) Electrooptic switches. The design for the electrooptic switches is similar to that for the traveling wave modulator analyzed in the discussion of the transmitter. It is shown that fast turn on and turn off can be achieved by overdriving the switch (i.e., by providing a modulating voltage which produces a phase change of greater than π radians in the arms of the switching interferometer). Fast turn on and turn off are important in generating suitable "time windows" for removing individual bits from the fiber buffer loops.
- (5) Frequency selective couplers. Optical frequency channels can be combined or separated using contradirectional coupling in parallel waveguide structures. The coupling is induced by a periodic perturbation in refractive index in the region between the waveguides. Side lobes which give rise to interchannel crosstalk can be greatly reduced in amplitude by tapering the strength of the



Rockwell International

ERC41015.4FR

perturbation in the coupling region. Numerical calculations indicate that couplers with low insertion loss and low reflection in the primary waveguide designed for a central wavelength of 8000\AA and a center-to-center separation of 4\AA between frequency channels can be designed to have a length of only 0.5 mm . It is important to minimize the lengths of the coupling region because of the relatively high attenuation of waveguides in GaAlAs.

4.0 TECHNOLOGY TRADEOFFS

The performance potential for each of the critical components for the very-high-speed bus has been analyzed in the preceding section. Key issues in the design of a practical bus using these components are considered below. A number of critical tradeoffs are identified, and in each case a preferred alternative is indicated. The alternatives considered are:

1. Fibers: multifiber vs single fiber with carrier frequency multiplexing.
2. Receivers: Si vs GaAs as the photodetector material.
3. Materials: "hybrid" (i.e., modulators and switches on a LiNbO_3 or LiTaO_3 substrate and lasers, photodetectors, and electronics on a GaAs substrate) vs "integrated" (i.e., all optical and electronic components on a single GaAs substrate).
4. Lasers: Fabry-Perot mirrors vs distributed feedback or distributed Bragg reflection mirrors.
5. Transmitters: directly modulated lasers vs cw lasers with external modulators.
6. Transmitters and receivers: FET amplifiers/drivers vs FET/TELD amplifiers/drivers.

Each of these tradeoffs is explored in more detail below:



ERC41015.4FR

1. Fibers: multifiber vs single-fiber with wavelength multiplexing.

This represents one of the most critical decisions in the design of the high-data-rate bus. Since the receivers are limited to data rates of about 5 Gbit/s, it will be necessary to transmit parallel channels to achieve higher data rates for the bus. The parallel channels can be accommodated by using a separate fiber for each channel, or by using frequency multiplexing to transmit a number of parallel channels on a single fiber. The use of one fiber per information channel would require N times as much fiber and N times as many terminal interfaces for an N-channel system. This implies a considerable increase in the cost of installation and maintenance as well as in the cost of components (fibers and connectors), and reduced reliability in comparison with a single-fiber system. It would also be necessary to equalize the lengths of the parallel fibers to tolerances of less than about 1 cm (= 50 ps delay for a silica fiber) in order to avoid timing errors for the data channels. The use of frequency multiplexing would greatly simplify the fiber optics portion of the system, but would require much more complex terminal devices. The optoelectronic integrated circuits at the terminals of the system require lasers emitting at different, precisely defined wavelengths and frequency-selective couplers for combining and separating the multiplexed channels. The technology development needed to achieve a given total data rate will be much greater than for the multi-fiber approach. However, once the capability to fabricate the required chips for multi-frequency operation (with several hundred optoelectronic and electronic devices per chip) is achieved, the cost per terminal for the bus system should not be prohibitive. Based on this argument and the potential cost and reliability advantages of the single-fiber approach, it is concluded that carrier frequency multiplexing is the preferable alternative.

2. Receivers: Si vs GaAs as the photodetector material.

In comparing Si and GaAs as materials for high-speed receivers, the key factor is the speed of response of the electronic amplifiers and threshold

circuits. Both Si and GaAs photodiodes are capable of response to 10 GHz, but GaAs is far superior to Si for the electronics. The GaAs FETs have a gain-bandwidth potential of the order of 50 GHz, a factor of 5 - 10 greater than Si FETs or bipolar transistors. Furthermore, there is no analog in Si to the TELD in GaAs, which has the potential for making binary decisions and for pulse regeneration at rates equivalent to 10-20 Gbit/s. Although it is possible in principle to use GaAs amplifiers with Si photodetectors, the additional capacitance from the photodiode-amplifier interconnections would degrade receiver performance. Furthermore, the "hybrid" receiver would probably be more expensive and less reliable than its fully integrated counterpart. For these reasons, it is concluded that the integrated receiver in GaAs is the preferred alternative.

3. Materials: "hybrid" with modulators and switches on a LiNbO_3 or LiTaO_3 substrate and lasers, photodetectors, and electronic components on a GaAs substrate vs "integrated" with all optical and electronic elements on a single GaAs substrate.

The advantage of having modulators and switches in a second material is that the ferroelectric materials LiNbO_3 and LiTaO_3 have much larger electrooptic coefficients than GaAs, although this is largely offset by the phase mismatch between optical and microwave propagation in the ferroelectrics. The optical attenuation at near-infrared wavelengths for LiNbO_3 and LiTaO_3 is also considerably less than the attenuation in GaAlAs (<1 dB/cm vs ~ 6 dB/cm), although it is possible that losses might be reduced considerably below 6 dB/cm in GaAlAs with improved waveguide fabrication techniques and purer waveguide material. On the other hand, the "hybrid" approach would require electrical and optical interconnections between the GaAs and LiNbO_3 or LiTaO_3 substrates. Increased optical loss would also result from the presence of additional interfaces, and the requirement for precise alignment of the chips to minimize this coupling loss would probably result in a substantial increase in cost. It is therefore concluded that advantages from the improved properties of LiNbO_3 and LiTaO_3 would



not warrant the additional complexity of the hybrid approach, and the integrated configuration is recommended.

4. Lasers: Fabry-Perot mirrors vs distributed feedback (DFB) or distributed Bragg reflection (DBR).

The lasing wavelength of the conventional Fabry-Perot laser is not controlled very precisely, because the mirror reflectance is practically independent of wavelength. The laser is thus free to operate over a wide range within its gain curve (e.g., over a range of tens of angstroms). Furthermore, the wavelength of the Fabry-Perot laser tends to depend strongly on both driving current and ambient temperature. On the other hand, the lasing wavelength of DBR or DFB lasers is accurately determined by the spatial period of the perturbation which causes the feedback, leading to wavelength stability under both cw and pulsed operation. The primary disadvantage of the DFB and DBR configurations is that the grating which provides the distributed reflectance must have a very small period, making it difficult to fabricate. The DFB and DBR lasers fabricated to date have used third-order gratings, with a periodicity of around 3600Å. However, part of the light propagating in the laser cavity is coupled by the gratings into radiation modes and is lost, leading to high threshold currents and low electrical-to-optical conversion efficiency. On the other hand, a first-order grating would have no such radiation-mode coupling, and the threshold current and efficiency should be comparable to those of the Fabry-Perot laser. The difficulty lies in fabricating the first-order grating, with a period of about 1200Å for emission at a wavelength of 8200Å in $\text{Ga}_x\text{Al}_{1-x}\text{As}$. Not only must very high resolution be achieved in the grating, but the period of the grating must be uniform (to about one part in 10,000) over its length.

In spite of the fabrication difficulty, the severe requirements for wavelength control and stability dictate the choice of the DFB or DBR structure in a wavelength-multiplexed system. These two alternatives (DFB and DBR) would have similar optical properties. The DBR laser would be somewhat longer than the DFB laser because gain and feedback regions are separated in the former

structure. On the other hand, the output wavelength of the DBR laser would be less affected by heating due to variations in the average laser current, because the distributed mirrors (which determine the lasing wavelength) are physically separate from the active region of the laser, where the power is dissipated. Based on this anticipated improvement in wavelength stability, the DBR structure is considered to be the preferable alternative.

5. Transmitters: directly modulated lasers vs cw lasers with external modulators.

For an "optoelectronic integrated circuit" with GaAs as the substrate material, the data rate for the externally modulated laser would be about 10 Gbit/s, vs only 5 Gbit/s for direct modulation. However, receiver response would limit the data rate per channel to about 5 Gbit/s. Furthermore, the length of the GaAs modulator would be in the range of 1 - 2 cm, and this is significant in view of the relatively high loss of the GaAs waveguides. This compares with a laser cavity length of about 1 mm. In addition to the loss factor, the length of the modulators would limit the number of channels which could be combined in a substrate a few cm long using frequency-selective couplers. Finally, assuming that an equal number of "ones" and "zeros" are transmitted, the external modulator will block most of the power emitted by the laser. This results in an additional loss in excess of 3 dB in comparison with the direct-modulated laser, assuming the same average optical power in both cases. Based on these arguments, it is concluded that direct laser modulation is preferred.

6. Transmitters and receivers: FET amplifier/drivers vs FET/TELD amplifiers/drivers.

The TELD is generally recognized as the fastest electronic logic device for room-temperature operation. The FET also can operate at very high bandwidths, but is basically a linear device. To perform the logic functions



ERC41015.4FR

required in digital drivers and repeaters with FETs, more complex circuits must be constructed. This makes the overall response speed inferior to that of the TELD. Therefore, in spite of the relatively high power consumption of the TELD, the amplifiers should use a combination of FETs and TELDs.

To summarize, based on the above arguments the preferred alternatives are:

- Transmission over single fibers with carrier frequency multiplexing
- GaAs as the photodetector material
- Integration of all components (except the fibers) on a single GaAs substrate
- Directly modulated laser transmitters
- Distributed Bragg reflection lasers
- FET/TELD amplifiers and drivers in receivers and transmitters.

The concept of a ring bus for connecting microprocessor terminals is illustrated in Fig. 5.1. It is assumed in the design that the data rate for the main bus is much higher than the input-output rates for the processors which interface with the bus. This means the data buffers must be provided at the terminals. However, conventional electronic shift registers are limited in transfer rate to a few hundred megahertz, and at these rates the capacity is limited to a few tens of bits and electrical power dissipation is high. For interfacing with the optical bus, improvements in both transfer rate and capacity by orders of magnitude are needed. It seems clear that a new type of data buffer is needed for this application.

It is proposed to use fiber optic loops as the data buffers, as illustrated schematically in Fig. 5.2. An input loop is provided for injecting data onto the bus, and an output loop for removing data from the bus. Each loop is provided with a digital repeater so that data can be recirculated indefinitely, and is connected to the main bus via a 2×2 electrooptic switch, of the type illustrated in Fig. 5.3. Data is injected into the input loop from a signal generator by means of a directional coupler, and is removed from the output loop and directed to an optical receiver by means of another electrooptic switch.

In order to inject data into the input loop at a low rate, the signal pulses must be generated at a much lower rate than the clock rate for the bus. For example, if the input loop contains N bits with a total delay of $N\tau$ seconds, the clock rate for the signal generator might be $(N+1)\tau$ seconds. This would correspond to adding one bit to the data stream each time it circulates completely around the loop, as illustrated in Fig. 5.4. If N were 1000, then the bus data rate would be 1001 times the buffer input rate. The input rate could be slowed even further if desired, by making the clock rate for the signal generator equal to $(mN+1)\tau$, where m is an integer. In this case, one bit would be inserted into the loop for each m times the data circulates around the loop.



FIBER OPTIC DATA BUS CONCEPT

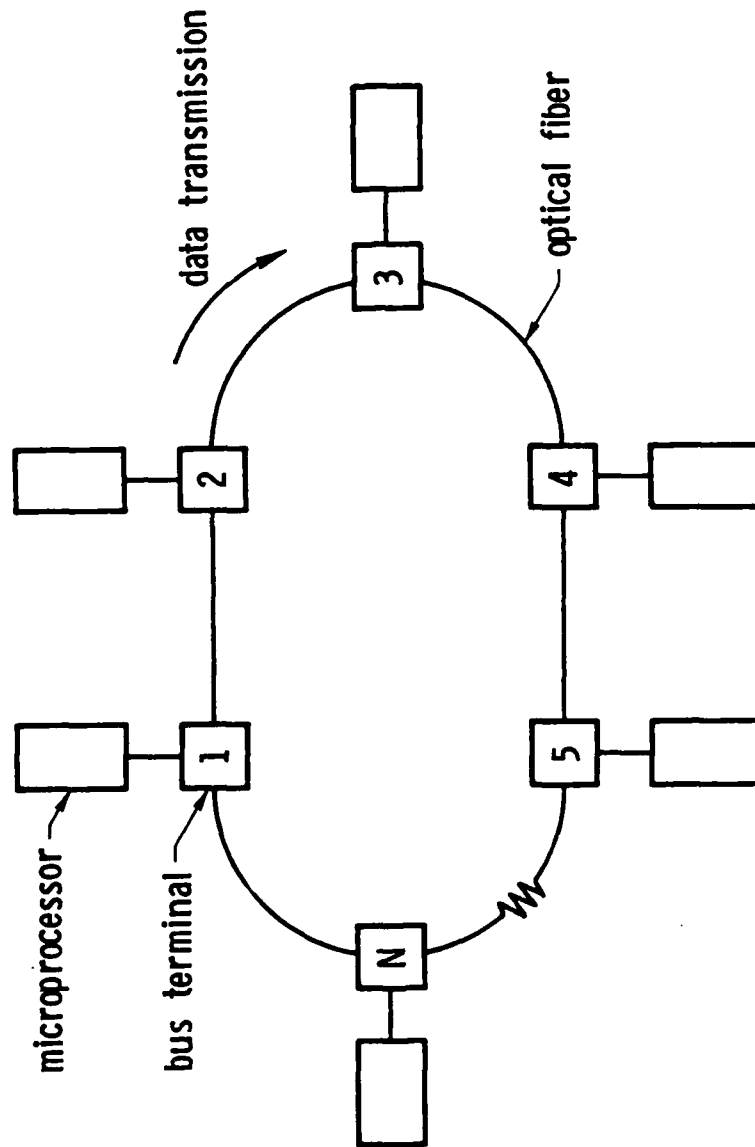


Fig. 5.1 Schematic of fiber optic bus for interconnecting microprocessor terminals.

RING BUS TERMINAL

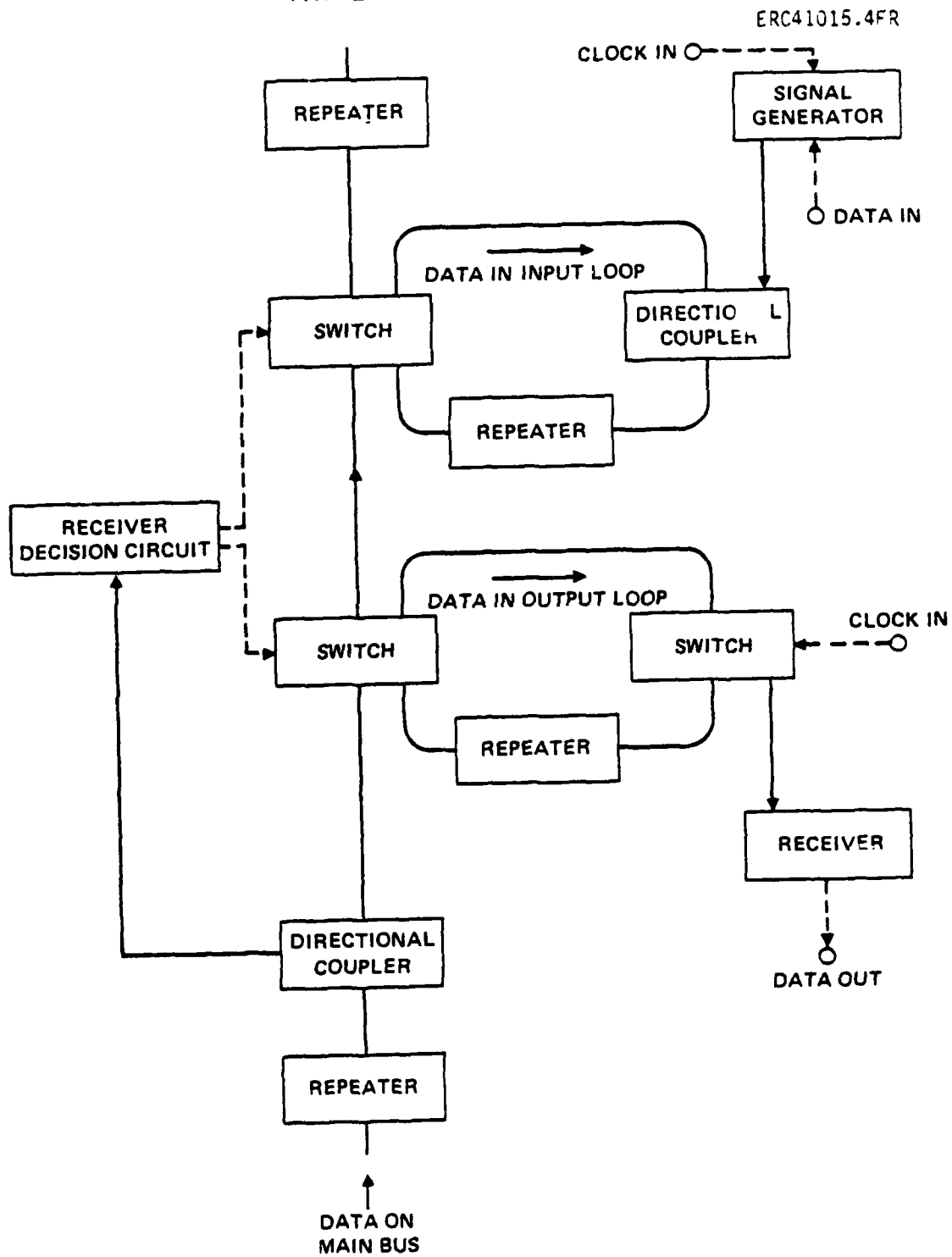


Fig. 5.2 Schematic of a terminal for the ring bus.



ERC41015.4FR

SC79-3746

SWITCH AT BUS TERMINAL

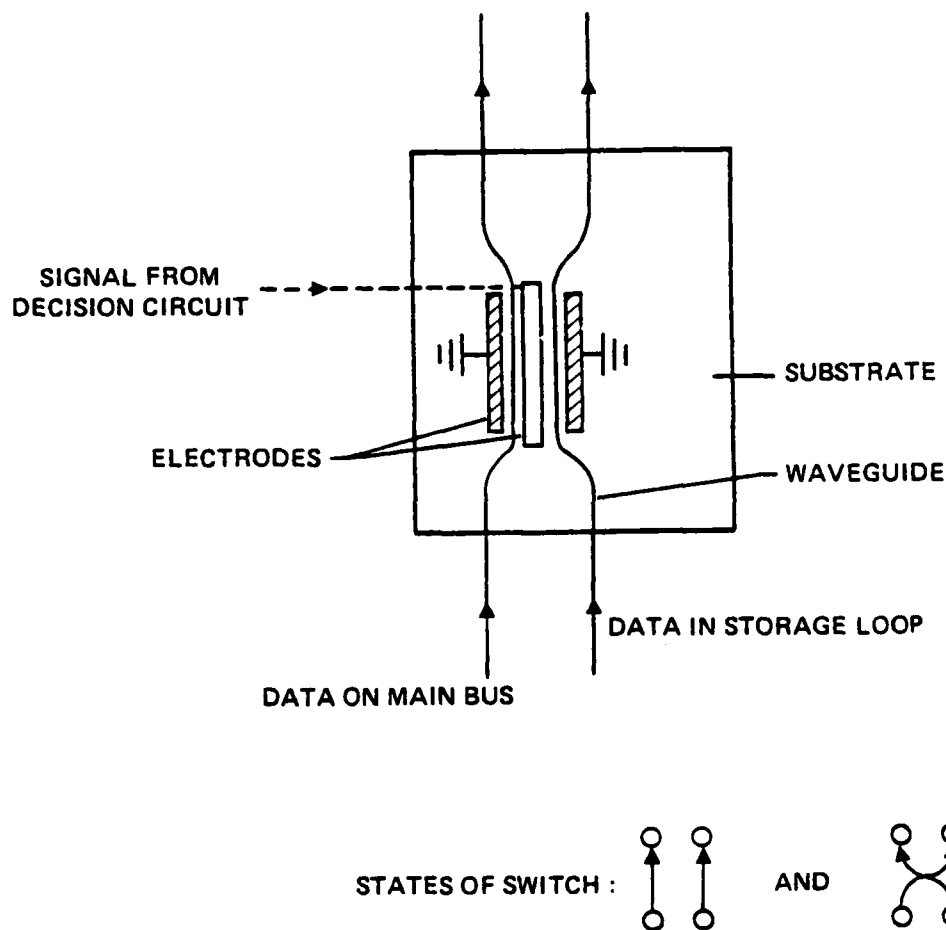
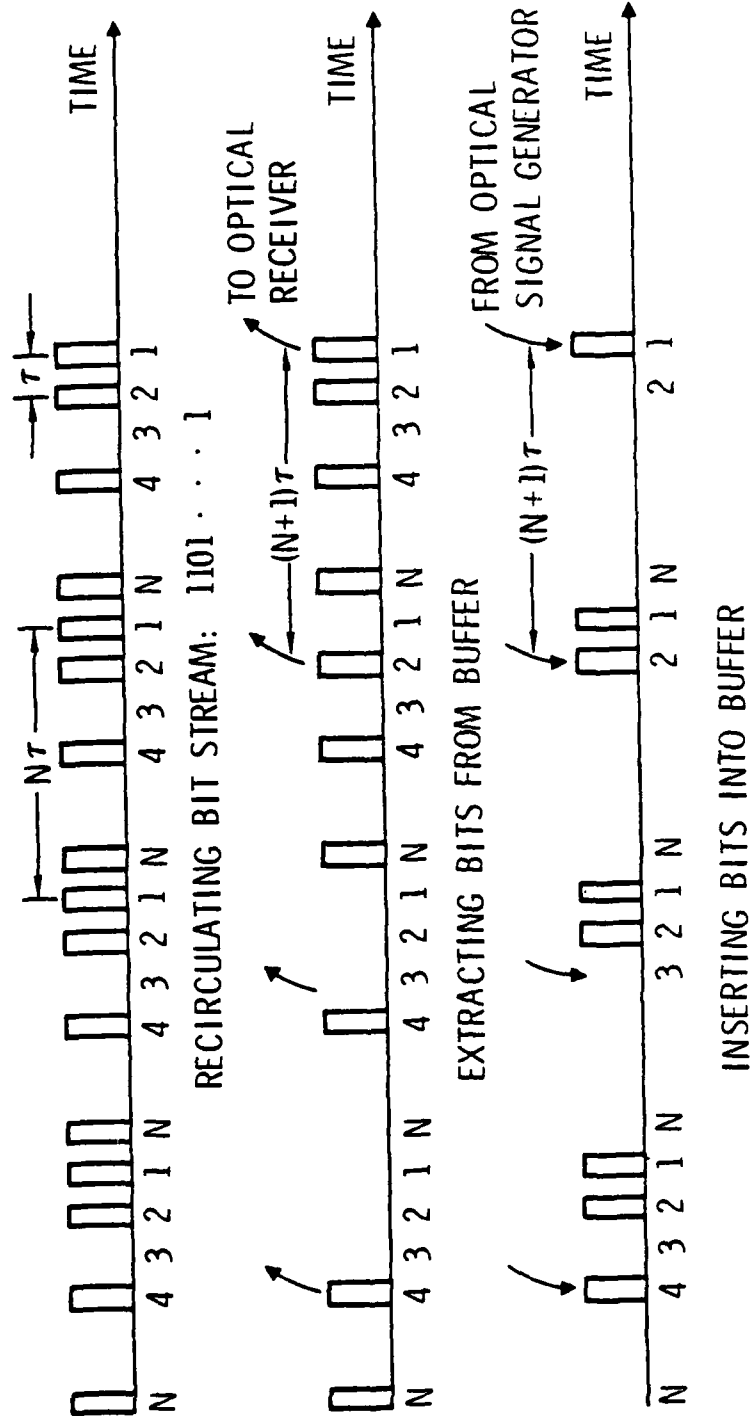


Fig. 5.3 A 2 x 2 electrooptic switch for interfacing between the main bus and a fiber buffer loop.



ERC41015.4FR

Fig. 5.4 Techniques for removing data from the output fiber buffer loop and for inserting data into the input buffer.



ERC41015.4FR

While data is being injected into the input loop, the electrooptic switch is in the "straight-through" state, so that the loop is, in effect, disconnected from the bus. When data is to be injected into the bus, the switch is changed to the "crossover" state, so that the entire contents of the loop are injected onto the bus. The switch is then returned to the "straight through" state.

For removing data from the bus, the switch connecting the output loop to the bus is changed to the "cross-over" state. After the desired data has been transferred from the bus to the loop buffer, the switch is returned to the "straight through" state, and the data continues to circulate in the loop. To remove data from the loop at a low rate, a second switch is activated by a clock pulse. As in the input loop, this clock rate is much lower than the bus data rate. For example, if N bits are stored in the output loop, the clock period could be $(mN + 1)\tau$, with m an integer, to remove one bit for each m times the data circulates around the loop.

As illustrated in Fig. 5.2, a directional coupler is provided on the main bus so that a portion of the optical signal can be directed to an optical receiver and decision circuit. The function of this circuit is to decode address and control instructions associated with the data packets and make a decision as to whether to divert the data to the output loop or whether to inject data from the input loop into the main bus. Since this decision must be made and the switch activated before the data packet arrives at the switch, the time delay between the downstream repeater and the receiver/decision circuit must be several bit intervals less than that from the repeater to the first switch. This delay might be obtained by connecting the repeater to the receiver decision circuit by a fiber that is slightly shorter than the length of main bus fiber from the repeater to the first switch. (See Fig. 5.2.) An additional delay of 1 ns, for example, would require a 20 cm fiber length difference.

If a data packet being read at a particular terminal is also to be read by downstream terminals, the switch between the main bus and the output loop would be only partially activated. In this case some of the light passes on to

the next downstream repeater on the main bus, and part circulates in the output loop. The electrooptic switches can easily be operated in this manner by applying only a fraction of the voltage required for complete switching. When a data packet returns to the originating terminal, it is necessary to remove it from the bus to prevent it from circulating indefinitely. This is accomplished by setting the switch to divert all of the main bus signal into the output loop. With the repeater power turned off, the packet would then be eliminated from the system.

Clock synchronization is an important feature of the bus design. It is envisioned that a master clock for all of the terminals could be provided by a single centrally located mode-locked laser connected to the terminals via a "star" coupler and fiber optic lines independent of the main bus. Mode-locked Nd:YAG lasers with average powers greater than 10 watts, pulse widths less than 50 ps, and repetition rates in the 80-250 MHz range are commercially available. This should be adequate for a bus with a thousand terminals or more. However, adjustment of timing to initialize the bit interval (to within a few ps) would be needed in the data output loop. This could be accomplished electronically, by adjusting the switch activation time relative to the clock pulse until maximum output (corresponding to proper bit interval adjustment) is obtained. A similar adjustment might also be needed in the repeater.

The preceding discussion of bus design architecture refers to a single-carrier-frequency bus system in which a fiber carries only one information channel at any given time. However, the same principles can be applied to the case in which multiple carrier frequencies are used to increase the data capacity of the fiber. Each terminal would then use a number of these frequency channels simultaneously to transmit a data packet, in order to reduce the packet duration and thus the transmission delay for the system as a whole. Implementation of the multi-frequency concept will require lasers operating at different, precisely determined wavelengths and frequency-selective couplers matched to the laser frequencies. An indication of how two of the key bus components, the signal generator and repeater, might be configured for multi-frequency operation



ERC41015.4FR

is given in Figs. 5.5 and 5.6. A hypothetical layout for a monolithic bus terminal chip is given in Fig. 5.7.

An important consideration in the design of such a system is the optical power budget. An example of a power budget calculation in which the loss margin is 5 dB is given in Table 5.1. The most important factor in determining the total loss is the attenuation factor in the optical waveguide, assumed to be 6 dB/cm. Propagation loss in the waveguide accounts for 15 dB of the 28 dB total loss in this example.

Table 5.1

Optical Power Budget Calculation for Fiber Buffer Loop

Average power emitted by laser	= 5 dBm
Average power required at receiver (5 Gbit/s data rate, 10^{-10} error rate)	= -28 dBm
Allowable loss	<u>33 dB</u>
Losses:	
Frequency selective coupler in transmitter (.5 cm at 6 dB/cm + 4 dB excess coupling loss)	7 dB
Switch to main bus (.5 cm at 6 dB/cm)	3 dB
Coupling to fiber and attenuation in fiber loop	5 dB
High-speed switch between fiber and buffer loop (1 cm at 6 dB/cm)	6 dB
Frequency selective coupler in receiver (.5 cm at 6 dB/cm + 4 dB excess loss)	<u>7 dB</u>
Total loss	<u>28 dB</u>
Loss Margin	<u>5 dB</u>

SIGNAL GENERATOR

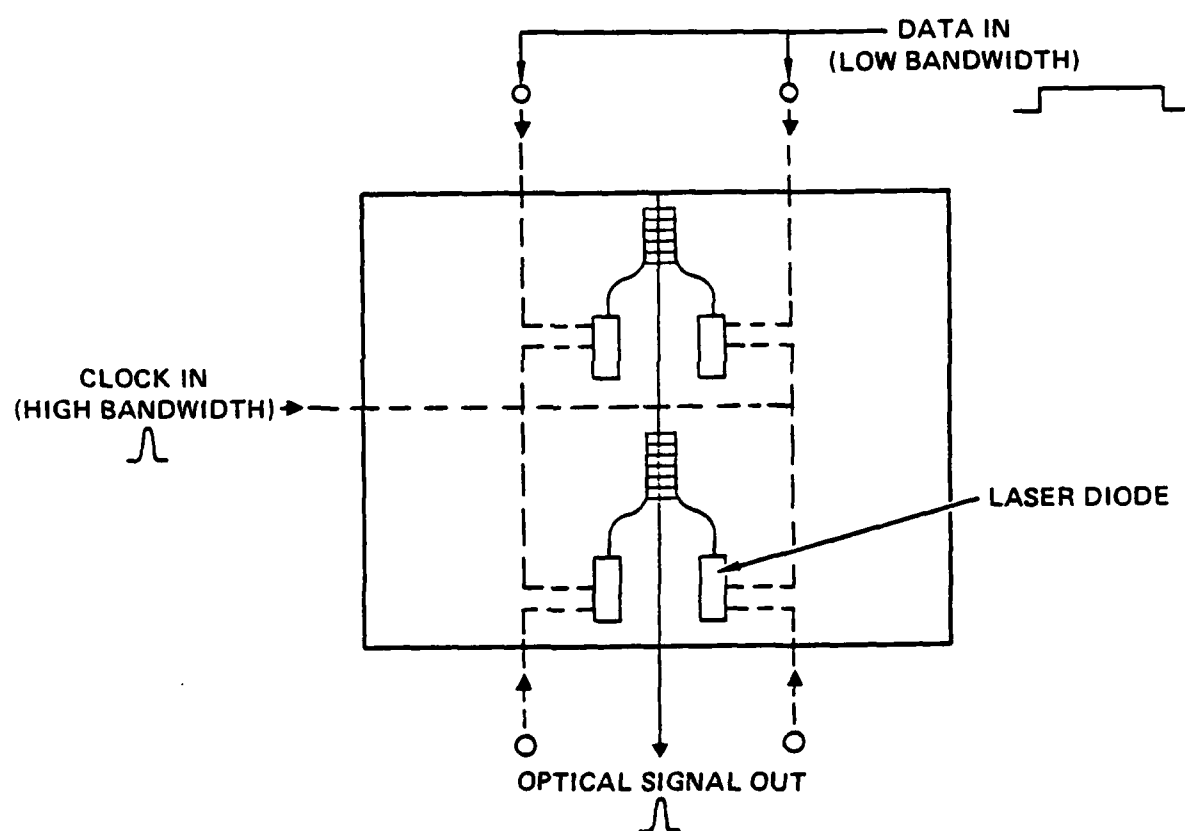


Fig. 5.5 Schematic for a signal generator for parallel frequency channels, using multifrequency lasers and a frequency-selective coupler for combining the channels.



Rockwell International

ERC41015.4FR

SC79-3735

MULTI-WAVELENGTH OPTICAL REPEATER CHIP

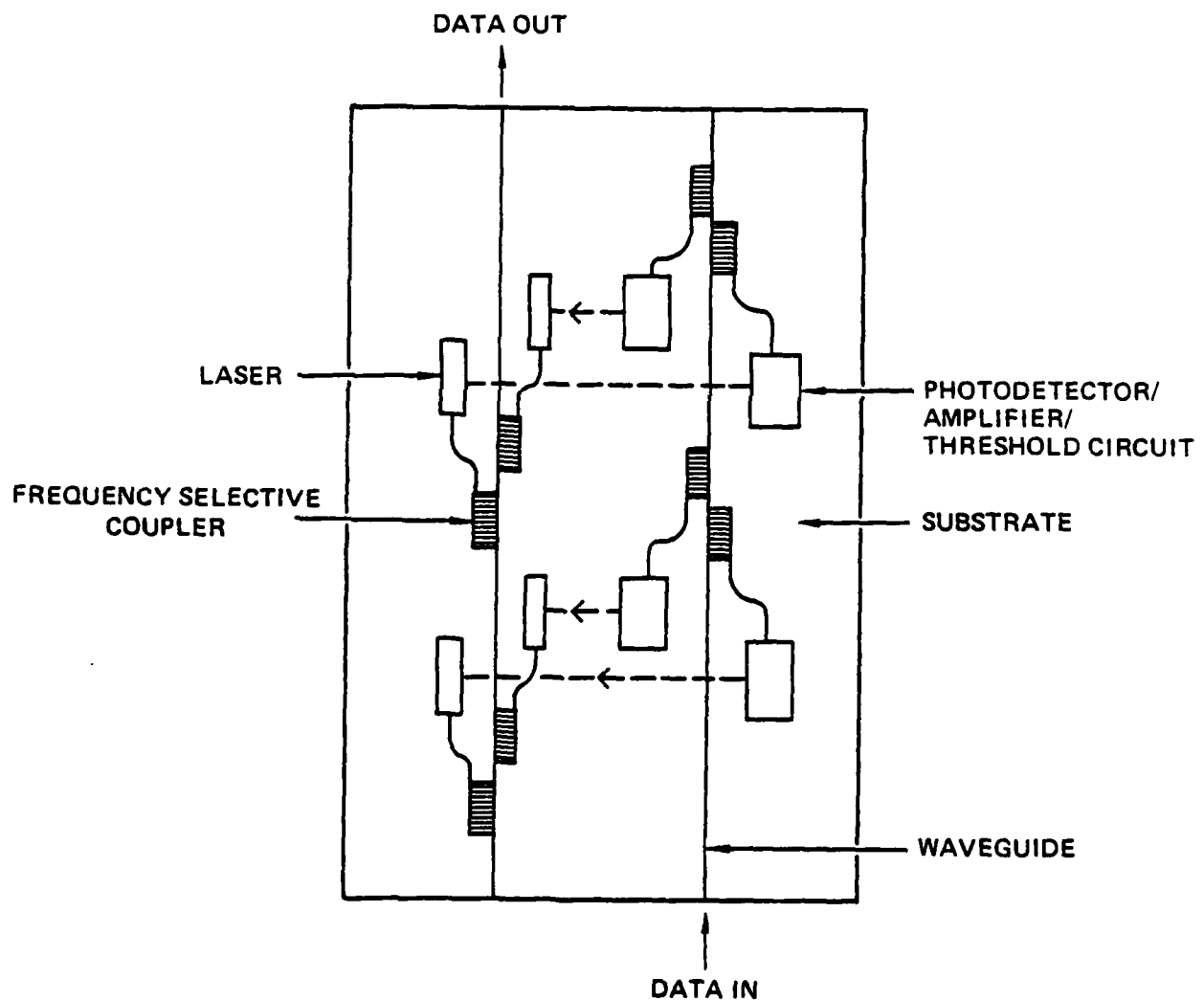


Fig. 5.6 Schematic for a multifrequency optical repeater chip.

MONOLITHIC BUS TERMINAL CHIP

ERC41015.4FR
SC79-4138

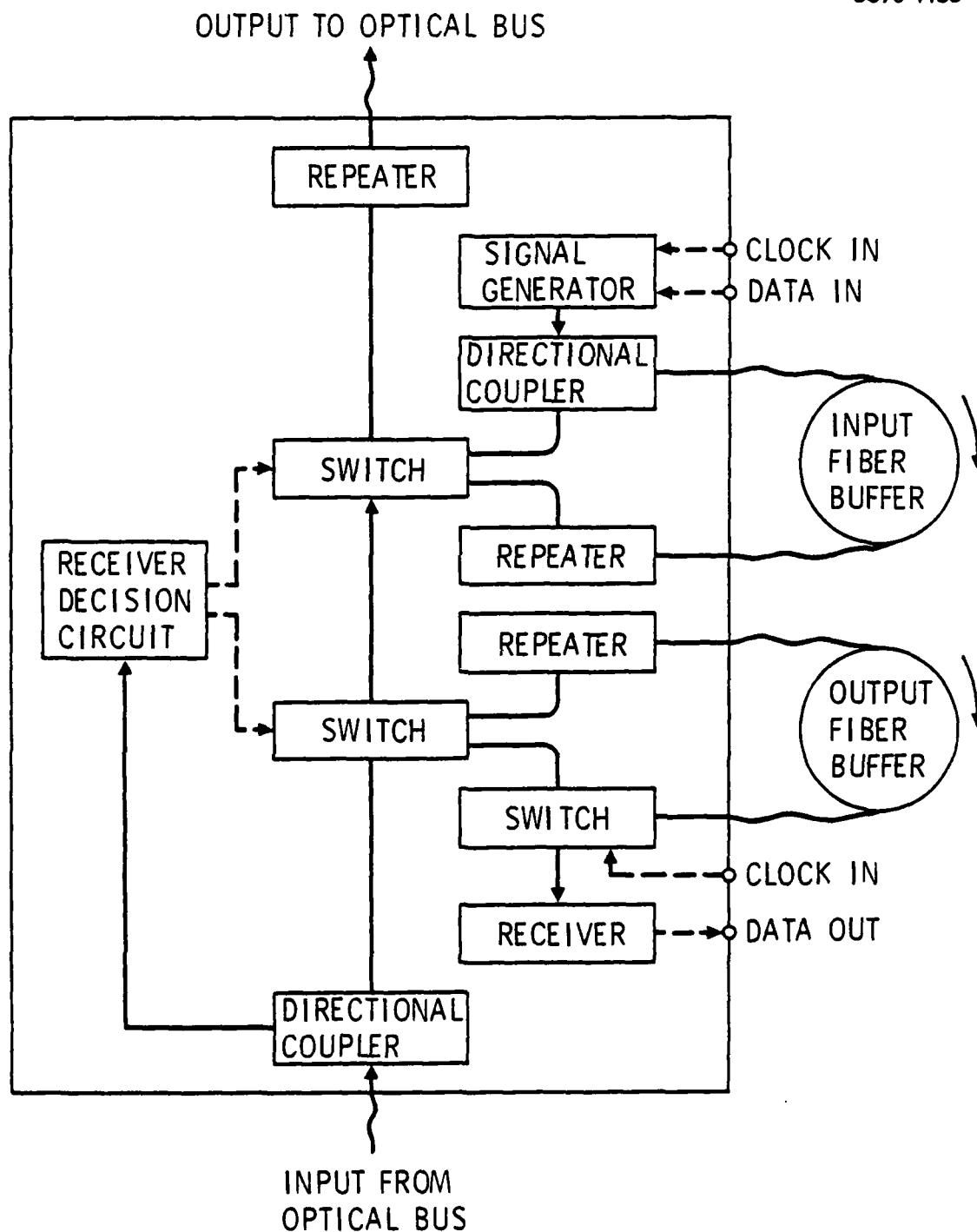


Fig. 5.7 Hypothetical layout for a monolithic bus terminal.



6.0 CONCLUSIONS

A great deal of technology development will be needed to push data rates for fiber optic data bus systems into the hundreds of gigabits-per-second range. The key to the realization of such systems is the ability to produce optoelectronic integrated circuits on a semi-insulating semiconductor substate, such as gallium arsenide. Feasibility of integrating the electronic and optical elements for transmitters and receivers on one substrate has already been demonstrated in the laboratory⁶¹⁻⁶³ although research in "integrated optoelectronics" is still at a very early stage. Circuits for the high-speed bus will contain optical sources, detectors, switches, frequency selective couplers and directional couplers, electronic FET and TED amplifiers, and microwave transmission lines. These circuits will perform the functions of modulation and demodulation of optical carriers, of multiplexing a number of frequency channels on a single-mode fiber transmission line, and of interfacing a high-data-rate bus with low-data-rate processors. The monolithic approach is necessary to maximize transmitter and receiver data rates and the number of wavelength-multiplexed channels, as well as to realize the advantages of low-cost fabrication and high reliability proven by previous experience with electronic integrated circuits. Tradeoffs considered in reaching these conclusions are discussed in detail in Section 4, while the design and operation of the bus are described in Section 5.

A plan leading to the realization of the fully integrated terminal of the optical bus will include the development on a semi-insulating substrate of each of the following functional elements:

- (1) Transmitters
- (2) Receivers
- (3) Repeaters
- (4) Directional Couplers
- (5) High-Speed Switches
- (6) Multifrequency Lasers
- (7) Frequency-selective Couplers

Ultimately, it will be necessary to integrate all of these elements on a single substrate. Each terminal of the computer network will then contain an optoelectronic circuit with electronic interfaces for data input/output and optical interfaces to fiber optic data buffers and to the main bus transmission line.

The technology development effort can be divided into three phases, as indicated below:

Phase I - Development of high-speed integrated transmitter and receiver. This effort will require the fabrication of lasers on the same substrate with electronic FET/TELD drivers, and avalanche photodiodes on the same substrate with FET/TELD amplifiers and decision circuits. Techniques will also be needed for interconnecting the optoelectronic and electronic elements to achieve high-speed operation. Successful completion of this phase will make possible the transmission of data over a fiber optics link at a rate of approximately 5 Gbit/s.

Phase II - Development of interface circuits for a fiber optic buffer loop. This will require the interconnection of receiver and transmitter to form a digital repeater, as well as the fabrication of a high speed electrooptic switch and its electronic driver. It will also be necessary to provide a timing circuit for synchronizing the operation of the switch (for data output) and laser transmitter (for data input) with the propagation delay in the fiber loop. Successful completion of this phase will make it possible to interface a high-data-rate fiber optic bus with low-data-rate data terminals to provide a 5 Gbit/s bus capability.

Phase III - Development of multiwavelength lasers and wavelength-selective couplers integrated on a single substrate. This task will require the fabrication of grating with very short, precisely controlled periods ($\sim 1200\text{\AA}$ period with $< .01\%$ deviation) incorporated into the laser and waveguide structure. Successful completion of this phase will make it possible to expand the data rate for the bus to 100 Gbit/s or greater.



ERC41015.4FR

The three phases of the effort indicated above are arranged in order of increasing difficulty, and the successful completion of one phase is considered to be a prerequisite to completion of the next. An example of how the key tasks might be phased in an eight-year development effort is indicated in Table 6.1. Although that milestone chart implies completion of one phase before the next phase is begun, it would be appropriate to address some of the key issues related to tasks called out in the latter phases (e.g., fabrication of the short periodicity grating needed for Phase III tasks) on a research basis prior to beginning scheduled development on those tasks. The eight-year time period is not considered overly conservative, but merely reflects the perceived degree of difficulty in reaching the goal of a 100 Gbit/s fiber optic data bus.

Table 6.1

Milestones for Fiber Optic Bus Technology Development

	Year from Start							
	1	2	3	4	5	6	7	8
<u>Phase I</u>								
Monolithic transmitter	→							
Monolithic receiver		→						
Fiber optic link demonstration 5 Gbit/s capacity			→					
<u>Phase II</u>								
Monolithic repeater			→	→				
Electro-optic switch			→	→				
Fiber loop buffer			→	→				
Single frequency bus terminal, 5 Gbit/s data rate				→				
<u>Phase III</u>								
Multifrequency lasers				→	→	→		
Frequency selective coupler				→	→	→		
Multifrequency repeater							→	
Multifrequency bus terminal, 100 Gbit/s data rate								→

REFERENCES

1. F.P. Kapron, D.B. Keck, and R.D. Maurer, "Radiation Losses in Glass Optical Waveguides," Appl. Phys. Lett., Vol. 17, pp. 423-425, Nov. 15, 1970.
2. T. Miya, V. Terunuma, T. Hosaka, and T. Miyashita, "Ultimate Loss Single-Mode Fibre and 1.55 μm ," Electron Lett., Vol. 15, pp. 106-108, Feb. 15, 1979.
3. J. Yamada, S. Machida, T. Kimura, and H. Takata, "Dispersion-Free Single-Mode Fibre Transmission Experiments up to 1.6 Gbit/s," Electron Lett., Vol. 15, pp. 278-279, May 10, 1979.
4. M. Chown, A.R. Goodwin, D.F. Lovelace, G.H.B. Thompson, and P.R. Selway, "Direct Modulation of Double-Heterostructure Lasers at Rates up to 1 Gb/s," Electron. Lett., Vol. 9, pp. 34-36, Jan. 25, 1973.
5. J.E. Carroll and J.G. Farrington, "Short-Pulse Modulation of Gallium Arsenide Lasers with Trapatt Diodes," Electron. Lett., Vol. 9, No. 7, pp. 166-167, April 5, 1973.
6. H.W. Thim, L.R. Dawson, L.V. DiLorenzo, J.C. Dymont, C.J. Hwang, and D.L. Rode, "Subnanosecond Pulse Code Modulation of GaAs Lasers by Gunn-Effect Switches," 1973 International Solid State Circuits Conference, Philadelphia, Feb. 1973.
7. C. Baack, G. Elze, G. Walf, G. Gliemroth, D. Krause, and N. Neuroth, "Optical Transmission Experiment at 1.12 Gbit/s using a Graded-Index Fibre with a Length of 1.652 km," Electron Lett. Vol. 13, pp. 452-453, August 4, 1977.



ERC41015.4FR

8. G. Deutsch, G. Lindner, K. Lubke, and H.W. Thim, "High-bit-rate Pulse Regeneration and Modulation of Injection Lasers with a Planar Gunn Device," Electron. Lett., Vol. 15, pp. 285-286, May 10, 1979.
9. J. Yamada, S. Machida, T. Kimura, and H. Takata, "Dispersion-Free Single-Mode Fibre Transmission Experiments up to 1.6 Gbit/s," Electron. Lett., Vol. 15, pp. 278-279, May 10, 1979.
10. J. Noda, N. Uchida, M. Minakata, T. Saku, S. Saito, and Y. Ohmachi, "Electro-optic Intensity Modulation in LiTaO₃ Ridge Waveguide," Appl. Phys. Lett. Vol. 26, pp. 298-300, March 15, 1975.
11. M. Izutsu, T. Itoh, and T. Snetta, "10 GHz Bandwidth Traveling Wave LiNbO₃ Optical Waveguide Modulation," IEEE J. Quantum Electronics, Vol. QE-14, pp. 394-395, June 1978.
12. M. Ross, P. Freedman, J. Abernathy, G. Matassov, J. Wolf, and J.D. Barry, "Space Optical Communications with the Nd:YAG Laser," Proc. IEEE, Vol. 66, pp. 319-344, March 1978.
13. H. Kanbe, T. Kimura, Y. Mizushima, and K. Kajiyama, "Silicon Avalanche Photodiodes with Low Multiplication Noise and High Speed Response," IEEE Trans. Electron Devices, Vol. ED-23, pp. 1337-1343, Dec. 1976.
14. H. Ando, H. Kanbe, T. Kimura, T. Yamaoka, and T. Kaneda, "Characteristics of Germanium Avalanche Photodiodes in Wavelength Region of 1 - 1.6 μ m," IEEE J. Quantum Electronics, Vol QE-14, pp. 804-809, Nov. 1978.
15. H.D. Law, K. Nakano, and L.R. Tomasetta, "III-V Alloy Heterostructure High Speed Avalanche Photodiode," IEEE J. Quantum Electronics, Vol QE-15, pp., July 1979.

16. S.M. Abbott and W.M. Muska, "Low-Noise Optical Detection of a 1.1 Gb/s Optical Data Stream," Electron. Lett., Vol. 15, pp. 250-251, 1979.
17. R.C. Eden, "Heterojunction III-V Alloy Photodetectors for High-Sensitivity 1.06 μ m Optical Receivers," Proc. IEEE, Vol. 63, pp. 32-37, Jan. 1975.
18. L.G. Cohen and C. Lin, "Pulse Delay Measurements in the Zero Material Dispersion Wavelength Region for Optical Fibers," Appl. Opt., Vol. 16, pp. 3136-3139, Dec. 1977.
19. A. Kawana, M. Kawachi, T. Miyashita, M. Saruwatari, K. Astani, J. Yamada, and K. Oe, "Pulse Broadening in Long-Span Single-Mode Fibers around a Material Dispersion-Free Wavelength," Opt. Lett., Vol 2, pp. 106-108, April 1978.
20. I. Natakaeyama and H. Tsuchiya, "Fusion Splices for Optical Fibers by Discharge Heating," Appl. Opt., Vol. 17, pp. 1959-1964, June 15, 1978.
21. N. Shimizu, H. Tsuchiya, and T. Izawa, "Low-loss Single-mode Fiber Connectors," Electron Lett., Vol. 15, pp. 28-29, Jan. 4, 1979.
22. T. Kimura, M. Saruwatari, J. Yamada, S. Uehara, and T. Miyashita, "Optical Fiber (800 Mbit/sec) Transmission Experiment at 1.05 μ m," Appl. Opt., Vol. 17, pp. 2420-2426, Aug. 1, 1978.
23. K. Nawata, S. Machida, and T. Ito, "An 800 Mbit/s Optical Transmission Experiment Using a Single-Mode Fiber," IEEE J. Quant. Electron. Vol. QE-14, pp. 98-103, Feb. 1978.
24. R.H. Stolen, V. Ramaswamy, P. Kaiser, and W. Pleibel, "Linear Polarization in Birefringent Single Mode Fibers," Appl. Phys. Lett., Vol. 33, pp. 699-701, October 15, 1978.



ERC41015.4FR

25. D.N. Payne and W.A. Gambling, "Zero Material Dispersion in Optical Fibers," *Electron Lett.*, Vol. 11, pp. 176-178, April 17, 1975.
26. P.M. Boers and M.T. Vlaardingerbroek, "Dynamic Behavior of Semiconductor Lasers," *Electron. Lett.*, Vol. 1, pp. 206-208, May 15, 1975.
27. G. Arnold and P. Russer, "Modulation Behavior of Semiconductor Lasers," *Appl. Phys.*, Vol. 14, pp. 255-268, Dec. 1977.
28. K. Kajiyama, S. Hata, and S. Sakata, "Effects of Spontaneous Emission on Dynamic Characteristics of Semiconductor Lasers," *Appl. Phys.*, Vol. 12, pp. 209-210, May 1977.
29. Casey and Panish
30. M. Ito and S. Machida, "Fractional Spontaneous Emission Coupled into AlGaAs Laser Mode," *Electron Lett.*, Vol. 14, pp. 693-695, Oct. 12, 1978.
31. H. Hillbrand and P. Russer, "Large Signal P.C.M. Behavior of Injection Laser with Coherent Radiation into One of Their Oscillating Modes," *Electron. Lett.*, Vol. 11, pp. 372-374, Aug. 7, 1975.
32. R.E. Matick, Transmission Lines for Digital Communication Networks, (McGraw Hill, New York, 1969), pp. 153-209.
33. J.C. Shelton, F.K. Reinhart, and R.A. Logan, "Rib Waveguide Switches with MOS Electrooptic Control for Monolithic Integrated Optics in GaAs-Al_xGa_{1-x}As," *Appl. Opt.* Vol. 17, pp. 2548-2555, August 15, 1978.
34. J. Noda, N. Uchida, S. Saito, T. Saku, and M. Minakata, "Electro-optic Amplitude Modulation Using Three-Dimensional LiNbO₃ Waveguide Fabricated by TiO₂ Diffusion," *Appl. Phys. Lett.*, Vol. 27, pp. 19-21, July 1, 1975.

35. C.U. Upadhyayula, R.E. Smith, J.F. Wilhelm, S.T. Jolly, and J.P. Paczkowski, "Transferred Electron Logic Devices for Gigabit-rate Signal Processing," IEEE Trans. Microwave Theory Tech., Vol. MTT-24, pp. 920-926, December, 1976.
36. J.G. Ruch and G.S. Kino, "Transport Properties of GaAs," Phys. Rev., Vol. 174, pp. 921-931, October 15, 1968.
37. K. Heine and A. Schlachetzki, "Pulse Generation in Planar Gunn Devices with Varying nL Product," Electron. Lett.
38. A. Schlachetzki and K. Mause, "Measurements of the Influence of the nd Product on the Gunn Effect," Electron. Lett., Vol. 8, pp. 240-241, May 4, 1972.
39. H.D. Law and C.A. Lee, "Interband Scattering Effects on Secondary Ionization Coefficients in GaAs," Solid State Electronics, Vol. 21, pp. 331-340, 1978.
40. L.R. Tomasetta, H.D. Law, R.C. Eden, I. Deyhmy, and K. Nakano, "High Sensitivity Optical Receivers for 1.0 - 1.4 μ m Fiber Optic Systems," IEEE J. Quant. Electron., Vol. QE-14, pp. 800-804, Nov. 1978.
41. R. Van Tuyt and C. Liechti, "Gallium Arsenide Spawns Speeds," IEEE Spectrum, Vol. 14, No. 3., pp. 41-47, March 1977.
42. H.F. Tayler, "Frequency-Selective Coupling in Parallel Dielectric Waveguides," Opt. Commun. Vol. 8, pp. 421-425, August 1973.
43. R.C. Alferness and R.V. Schmidt, "Tunable Optical Waveguide Directional Coupler Filter," Appl. Phys. Lett., Vol. 33, pp. 161-163, July 15, 1978.
44. M. Kobayashi and A. Tani, "Optical Demultiplexer Using Coupling Between Nonidentical Waveguides," Appl. Opt. Vol. 17, pp. 3253-3258, Oct. 15, 1978.



ERC41015.4FR

45. R.C. Alferness and P.C. Cross, "Filter Characteristics of Codirectionally Coupled Waveguides with Weighted Coupling," IEEE J. Quant. Electron., Vol. QE-14, pp. 843-847, November 1978.
46. C. Elachi and C. Veh, "Frequency Selective Coupler for Integrated Optics Systems," Opt. Commun., Vol. 7, pp. 201-204, March 1973.
47. See, for example, P.K. Tier, "Light Waves in Thin Films and Integrated Optics," Appl. Opt. Vol. 10, pp. 2395-2413.
48. P. Yeh, A. Yariv, and C.S. Hong, "Electromagnetic Propagation in Periodic Stratified Media. I. General Theory," J. Opt. Soc. Amer., Vol. 67, pp. 423-438, April 1977.
49. D.C. Flanders, H. Kogelnik, R.V. Schmidt, and C.V. Shank, "Grating Filters for Thin-Film Optical Waveguides," Appl. Phys. Lett., Vol. 24, pp. 194-196, Feb. 15, 1974.
50. K. Aiki, M. Nakamura, J. Umeda, A. Yariv, A. Katzir, and H.W. Yen, "GaAs-GaAlAs Distributed Feedback Diode Lasers with Separate Optical and Carrier Confinement," Appl. Phys. Lett., Vol. 27, pp. 145-146, August 1, 1975.
51. See, for example, A. Yariv, Quantum Electronics, (Wiley, New York, 1975), pp. 521-522.
52. P. Yeh, "Electromagnetic Propagation in Birefringent Layered Media," J. Opt. Soc. Amer., Vol. 69, pp. 742-756, May 1979.
53. See, for example, Ref. 46, p. 520.
54. See, for example, J.D. Jackson, Classical Electrodynamics, (Wiley, New York, 1962), p. 259.

55. E.A.J. Marcatili "Dielectric Rectangular Waveguide and Directional Coupler for Integrated Optics," Bell Syst. Tech. J., Vol. 48, pp. 2071-2102, Sept. 1969.
56. See, for example, L. Schiff, Quantum Mechanics, 3rd Edition (McGraw Hill, New York, 1968), p. 255.
57. H.F. Taylor, "Optical Switching and Modulation in Parallel Dielectric Waveguides," J. Appl. Phys., Vol. 44, pp. 3257-3265, July 1973.
58. L.B. Stotts, "Eigenvalue Expression for Multilayer Thin-Film Optical Branch and Mode Resonant Structures," Opt. Commun., Vol. 17, pp. 133-140, April 1976.
59. H. Yajima, Proc. Symp. Optical and Acoustical Microelectronics (New York, April 1974).
60. For the definition of E_y modes, see Ref. 55.
61. I. Ury, S. Margalit, M. Yust, and A. Yariv, "Monolithic Integration of an Injection Laser and a Metal Semiconductor Field Effect Transistor," Appl. Phys. Lett., Vol. 34, pp. 430-431, April 1, 1979.
62. C.P. Lee, S. Margalit, I. Ury, and A. Yariv, "Integration of an Injection Laser with a Gunn Oscillator on a Semi-Insulating GaAs Substrate," Appl. Phys. Lett., Vol. 32, pp. 806-807, June 15, 1978.
63. M. Yust, N. Bar-Chaim, S.H. Izadpanah, S. Margalit, I. Ury, D. Witt, and A. Yariv, "A Monolithically Integrated Optical Repeater," Appl. Phys. Lett., Vol. 35, pp. 795-798, November 15, 1979.



Rockwell International

PREPRINT No. _____

Electronics Research Center

DISTRIBUTION FOR TECHNICAL MEMORANDUM

Author(s): _____ Henry F. Taylor _____

Title: _____ Multi-processor Bus Architecture _____

Preprint - submitted to: _____ Defence Advanced Research Projects Agency _____

Date: _____

Electronics Research Center

Vice President
Directors
Library (2) (original + 1)
Patent Section
Group Leader
Author (12)
Group Secretary (2)
Contracts & Pricing (1)

Other

Defence Advanced Research Projects Agency
1400 Wilson Boulevard
Arlington, VA 22209

Att: Dr. Vinton Cerf (25)

Att: Program Management (2)

Defense Documentation Center
Cameron Station
Alexandria, VA (12)